An Interdisciplinary Journal of

Discontinuity, Nonlinearity, and Complexity

L&H

Discontinuity, Nonlinearity, and Complexity

Modelling, Analysis and Control of Nonlinear Discrete and Continuous Mechanical Structures Dedicated for Mechatronic Applications

Jan Awrejcewicz[†], Dariusz Grzelczyk

Department of Automation, Biomechanics and Mechatronics, Lodz University of Technology,
1/15 Stefanowski Street, 90-924 Lodz, Poland

Submission Info	Abstract
	This is the Special Issue dedicated to the 13th International Conference on "Dynamical Systems - Theory and Applications" (DSTA-2015) which was held on December 7-10, 2015 in Łódź Poland. The main aim of the conference was to provide a platform for researchers and engineers to present and discuss the current state and contemporary investigations in different disciplines of science, bioscience, and engineering. This issue presents eight selected manuscripts related to the modeling, analysis and control of nonlinear discrete and continuous mechanical structures met in mechatronic applications.

Preface

The main aim of the conference was to provide a platform for researchers and engineers to present and discuss the current state and contemporary perspective for modeling, simulation, and control of nonlinear/discontinuous dynamical systems, a rapidly developing research branch including different disciplines of science, bioscience, and engineering.

The Scientific Committee of the conference included the following reputable researchers: H. Altenbach – **Germany**, M. Alves – **Brazil**, I.V. Andrianov – **Germany**, J. Awrejcewicz – Chairman, **Poland**, J.M. Balthazar – **Brazil** T. Burczyński – **Poland**, Cz. Cempel – **Poland**, F. Chernousko – **Russia**, F. Dohnal – **Switzerland**, V.-F. Duma – **Romania**, I. Elishakoff – **USA** M. Fečan – **Slovakia**, N. Ferreira – **Portugal**, B. Gallacher – **UK**, O. Gendelman – **Israel**, O. Gottlieb – **Israel**, P. Hagedorn – **Germany** K. (Stevanović) Hedrih – **Serbia** L. Kolar-Anić– **Serbia** I. Kovacić– **Serbia**, J. Kowal – **Poland**, J. Kozanek – **Czech Republic**, P. Krasilnikov – **Russia**, V.A. Krysko – **Russia**, W. Lacarbonara – **Italy**, L.V. Kurpa – **Ukraine**, C.-H. Lamarque – **France**, S. Lenci – **Italy,** G.A. Leonov – **Russia**, A. Luo – **USA**, E. Macau – **Brazil**, J.A. Machado – **Portugal**, N.M.M. Maia – **Portugal**, L.I. Manevitch – **Russia**, A.A. Martynyuk – **Ukraine**, S. Maruyama – **Japan**, G.I. Mikhasev – **Belarus**, Y. Mikhlin – **Ukraine**, G. Olivar – **Colombia**, M. Pascal – **France**, Ch. Pierre – **USA**, V.N. Pilipchuk – **USA**, C.M.A. Pinto – **Portugal**, J. Przybylski– **Poland**, S. Radkowski – **Poland**, B. Radziszewski – **Poland**,

---

[†]Corresponding author.
Email address: jan.awrejcewicz@p.lodz.pl

P. Ribeiro – **Portugal**, R. Sampaio – **Brazil**, A. Seyranian – **Russia**, Ch.H. Skiadas – **Greece**, S. Theodossiades – **UK**, J.J. Thomsen – **Denmark**, J.J. Trujillo – **Spain**, A. Tylikowski – **Poland**, F. Udwadia – **USA**, T. Uhl – **Poland**, A.F. Vakakis – **USA**, F. Verhulst – **The Netherlands**, J. Warmiński – **Poland**, M. Wiercigroch – **UK**, E. Wittbrodt – **Poland**, H. Yabuno – **Japan**, H.M. Yehia – **Egypt**, K. Zimmermann – **Germany**.

Out of all manuscripts recommended by the Scientific Committee of the conference, the following eight manuscripts have been eventually selected for publication in this special issue. A brief description of each paper is as follows.

(1) Jarzęowska and Pilarczyk present a theoretical model-based tracking controller design for a free-floating space robot for a mission scenario of intercepting an object. Due to the growing space exploration and numerous objects and space debris needed to be removed from space, such missions are interesting from a practical point of view. The required service tasks and debris removal need to be performed by specialized robots. The debris interception scenario presented in this paper consists of estimation of target properties and a controller design to track and intercept the debris, and move it to the graveyard orbit.

(2) Antoniadis et al. examine the implementation of a standalone 1 MW Wave Energy Converter (WEC) based on a novel concept of a class of WECs, comprising fully enclosed appropriate internal body configurations, and providing inertial reaction against the motion of an external vessel. The optimal dynamic design of the geometry, mass, and inertia distribution of the internal body ensure the maximal conversion and storage of the wave energy. Moreover, the proposed concept is flexible and parametrically designed, what enables its implementation in any form of floating vessels.

(3) Hedrih and (Stevanović) Hedrih investigate a quasi-static continual ZP (Zona Pelucida) model, this is highly specialized glycosylated and sulfated polymer gel that surrounds mammalian oocyte, which exhibits elastic or viscoelastic properties and a change in diameter in different maturation stages. The authors numerically investigate: how the distance from the center of the oocyte affects different parameters relevant for fertilization process, like stresses and strains state at an arbitrary point that appear in ZP hollow sphere in the fertilization process; how the specific deformation work in ZP and volume dilatation depend on ZP thickness and external pressure.

(4) Barski et. al consider a problem of fatigue cracks detection and evaluation in the case of isotropic rectangular plates with circular holes, subjected to the periodic tension. The fatigue cracks are formed in the vicinity of the hole and this type of damages can be effectively detected by analyzing the propagation of elastic waves. This propagation is simulated with the use of the finite element method, whereas the elastic waves are excited and picked up by piezoelectric sensors. Moreover, the advanced algorithm of crack detection and evaluation is also discussed.

(5) Jaworski and Szlachetka study the first mode of natural transverse vibrations of isotropic, homogeneous, and elastic bars (columns or beams) with clamped bottom and free head. Some interesting analytical/numerical solutions of the integral equation are obtained and discussed. The first frequency of free vibrations is determined using the Rayleigh method. In addition, the obtained values of the frequencies (or periods) are compared with these obtained with the use of finite element modeling and a good compliance of results is observed.

(6) Buchacz and Gałęziowski investigate the problem of vibration control for elements which have defined configurations and connections of piezostack actuator with external electric network and can exhibit negative values. Negative elements, used for the design of mechatronic systems, are identified and described and comply with some given requirements. The considered examples present limits and constrains that may support the physical realization as well as applications of the considered systems.

(7) Polach et. al create a multibody model of a simple weight-fiber-pulley-drive mechanical system. Investigations of the behavior of fiber and experimental laboratory measurements are described, including the influence on the coincidence of simulation results of the fiber spring-damper coefficients dependences on the velocity of the weight motion in the computational model. Finally, the authors present a phenomenological model of the fiber which will be utilizable in fiber modeling in the case of more complicated mechanical or mechatronic systems.

(8) Danylenko and Skurativskyi study a mathematical model for mutually penetrating continua, which consists of the wave equation describing the carrying medium and the equation for oscillators forming the oscillating inclusion. They are interested in the structure of wave solutions obeying the dynamical system of Hamiltonian type, which allows one to determine the peculiarities of the phase space of dynamical system, i.e. the relation describing the homoclinic trajectories, the division of phase plane into the parts with equivalent orbits' behavior, and the conditions of bifurcations. To simulate the wave dynamics, the authors construct the three-level finite-difference numerical scheme and study the evolution of solitary waves, their pair interactions, and their stability.

We do hope that the readers of the **Journal of Discontinuity, Nonlinearity and Complexity** will be attracted by the topics covered in this special issue. We greatly appreciate the willingness and strong support of Editors of DNC Journal to publish the aforementioned papers recommended by the Scientific Committee in this special issue after the standard review procedure. Finally, also we would like to thank all referees for their help in papers selection procedure.

Jan Awrejcewicz and Dariusz Grzelczyk

Guest Editors

Dynamics of Waves in the Cubically Nonlinear Model for Mutually Penetrating Continua

Vjacheslav Danylenko, Sergii Skurativskyi[†]

Subbotin Institute of Geophysics, NAS of Ukraine, Bohdan Khmelnytskyi str. 63-G, Kyiv, Ukraine

Abstract

In this report we study the mathematical model for mutually penetrating continua. This model consists of the wave equation describing the carrying medium and the equation for oscillators forming the oscillating inclusion. Prescribing the constitutive equation of the carrying medium and kinetics of oscillator's dynamics for model in question, the cubic nonlinearity is accounted. We are interested in the structure of wave solutions obeying the dynamical system of Hamiltonian type. This allows us to determine the peculiarities of the phase space of dynamical system, namely, the relation describing the homoclinic trajectories, the division of phase plane into the parts with equivalent orbits' behavior, the conditions of bifurcations. To simulate the wave dynamics, we construct the three level finite-difference numerical scheme and study the evolution of solitary waves, their pair interactions and stability. Propagation of periodic waves is modeled as well.

©2017 L&H Scientific Publishing, LLC. All rights reserved.

1 Introduction

Geophysical media are open strongly nonequilibrium systems which possess the hierarchic block structure described by the sets of spatial and temporal scales [1, 2]. In these media, wave processes undergo the influence of material's microstructure in a wide range of wave lengths and speeds [3, 4]. To study structural effects, we need to revise the classical mathematical models suitable for homogeneous media.

One of the ways to improve the classical models is the incorporation of additional degrees of freedom associated with the discreteness of materials and describing the oscillating dynamics [2, 5, 6] of structural elements. Utilizing this approach, the mathematical model for mutually penetrating linear continua had been developed in [7, 8].

This model consists of the wave equation for carrying medium and equations of motion for oscillating continuum which is regarded as the set of partial oscillators. To generalize the linear counterpart of this model, the nonlinearity has been incorporated in the equation of state for carrying medium [9–11] and in the kinetics for oscillator's equations of motion [12]. We thus are going to treat the following mathematical model

$$\rho \frac{\partial^2 u}{\partial t^2} = \frac{\partial \sigma}{\partial x} - m\rho \frac{\partial^2 w}{\partial t^2}, \qquad \frac{\partial^2 w}{\partial t^2} + \Phi(w - u) = 0, \tag{1}$$

[†]Corresponding author.
  Email address: skurserg@gmail.com

where ρ is medium's density, u and w are the displacements of carrying medium and oscillator from the rest state, $m\rho$ is the density of oscillating continuum. To identify model (1), we apply the cubic constitutive equation for the carrying medium $\sigma = e_1 u_x + e_3 u_x^3$, where e_1 is Young's modulus, e_3 is related to the fourth order elastic moduli describing the deviation from Hooke's law [13]. The relation for applied force $\Phi(x) = \omega^2 x + \delta x^3$ leads to the Duffing like equation of motion [14]. Here ω denotes the natural frequency of oscillator, whereas the parameter δ appears due to accounting for the cubic term in the expansion of restoring force in a power series.

Among the possible applications [15] of the model, it is worth noting that system (1) can provide the models for wave processes in soils, sands, rocks, which possess the dominant frequencies [16, 17], and liquids with bubbles of insoluble gas [18]. The oscillating dynamics of structural elements and physical nonlinearity in combination can lead to cooperative effects and cause the emergence of localized wave regimes similar to solitary waves [13, 19]. We are thus interested in solutions to model (1) which appear due to enriched equations of motion.

Now we are going to consider the properties of traveling wave solutions having the following form

$$u = U(s), \quad w = W(s), \quad s = x - Dt, \tag{2}$$

where the parameter D is a constant velocity of the wave front. System (1) is studied in unbounded domain $x \in (-\infty; +\infty)$ for $t > 0$ without any additional boundary or initial constrains. We also omit any equivalent transformations, like $u \to u + f(x,t)$, $w \to w + f(x,t)$, where $f(x,t) = (v_1 x + v_2)(v_3 t + v_4)$, v_i are arbitrary constants. Without loss of generality, we can consider system (1) as the model written in dimensionless form [20].

In the previous paper [12], we had concentrated our attention upon the properties of peculiar part of solution (2), namely, solitary waves, while in this report we deal with the periodic ones as well.

Inserting (2) into model (1), it is easy to see that the functions U and W satisfy the dynamical system

$$D^2 U' = \rho^{-1}\sigma\left(U'\right) - mD^2 W', \quad W'' + \Omega^2\left(W - U\right) + \delta D^{-2}\left(W - U\right)^3 = 0,$$

where $\Omega = \omega D^{-1}$.

This system can be written in the form

$$W' = \alpha_1 R + \alpha_3 R^3, \qquad U' = R, \qquad (\alpha_1 + 3\alpha_3 R^2)R' + \Omega^2(W - U) + \delta D^{-2}(W - U)^3 = 0, \tag{3}$$

where $\alpha_1 = \dfrac{e_1 - D^2\rho}{m\rho D^2}$, $\alpha_3 = \dfrac{e_3}{m\rho D^2} > 0$. Through the report we fix

$$e_1 = \rho = 1, e_3 = 0.5, m = 0.6, \omega = 0.9$$

in numerical treatments.

1.1 Traveling waves in the model with the linear equation of motion for oscillating inclusions

At first, consider system (3) at $\delta = 0$. Excluding the variable W, system (3) is reduced to the planar system

$$\left(\alpha_1 + 3\alpha_3 R^2\right)^2 R' = Z\left(\alpha_1 + 3\alpha_3 R^2\right)^2, \tag{4}$$
$$\left(\alpha_1 + 3\alpha_3 R^2\right)^2 Z' = -\left[6\alpha_3 R Z^2 + \Omega^2\left((\alpha_1 - 1)R + \alpha_3 R^3\right)\right]\left(\alpha_1 + 3\alpha_3 R^2\right),$$

which admits the Hamiltonian

$$H = \frac{1}{2}Z^2\left(\alpha_1 + 3\alpha_3 R^2\right)^2 + \frac{\Omega^2}{2}[\alpha_3^2 R^6 + \frac{4\alpha_1 - 3}{2}\alpha_3 R^4 + \left(\alpha_1^2 - \alpha_1\right)R^2] = \text{const.}$$

The detail description of phase plane of dynamical system (4) had been done in the paper [21], we thus summarize the main results only.
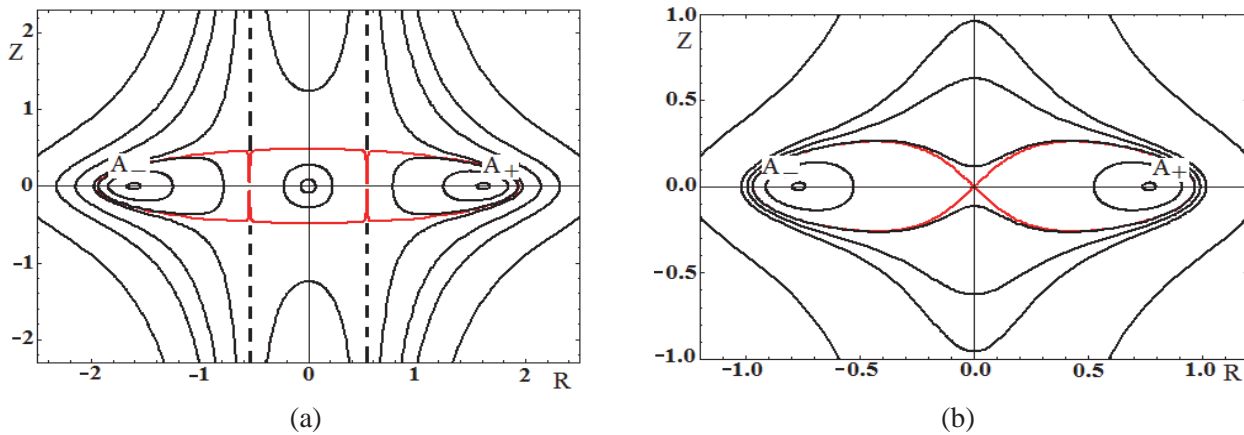
Fig. 1 The phase portraits for system (4) at (a): $\alpha_1 < 0$ ($D = 1.2$) and (b): $0 < \alpha_1 < 1$ ($D = 0.9$).

System (4) has the fixed points

$$O(0;0) \quad \text{and} \quad A_\pm(\pm Q;0),$$

where $Q = \sqrt{(1 - \alpha_1)/\alpha_3}$ if $(1 - \alpha_1)/\alpha_3 > 0$.

It easy to see that at $\alpha_1 < 1$ the phase plane contains three fixed points, whereas at $\alpha > 1$ the only one fixed point (center) remains.

For $\alpha_1 < 0$, when $D = 1.2$ is fixed for definiteness, a typical phase portrait is depicted in the Fig. 1a. In this case all fixed points are centers surrounded by periodic orbits. There are separatrices depicted by red curves and separated the regions with periodic and unbounded trajectories. Two dashed lines are defined by the relation $R = \pm\sqrt{-\alpha_1/3\alpha_3}$ corresponding to discontinuity of system (4). It can be checked that existence of solutions is possible when the following inequality $H > -\frac{(1-\alpha_1)^2\Omega^2}{4\alpha_3} = -0.55$ holds.

When $0 < \alpha < 1$, at $D = 0.9$ for instance, in the phase portrait (Fig. 1b) one can distinguish the homoclinic trajectories that go through the origin. Since for these trajectories the Hamiltonian $H = 0$, the relation for $Z = Z(R)$ and the expression $s - s_0 = \int dR/Z(R)$ for the homoclinic loop can be written in the explicit form

$$s - s_0 = \frac{3}{2\Omega} \arcsin\left(\frac{4\alpha_3 R^2 - 3 + 4\alpha_1}{\sqrt{9 - 8\alpha_1}}\right) - \frac{1}{2\Omega}\sqrt{\frac{\alpha_1}{1 - \alpha_1}}$$

$$\times \ln\left(\frac{1}{R^2} + \frac{3\alpha_3 - 4\alpha_1\alpha_3}{4(\alpha_1 - \alpha_1^2)} + \sqrt{\left\{\frac{1}{R^2} + \frac{3\alpha_3 - 4\alpha_1\alpha_3}{4(\alpha_1 - \alpha_1^2)}\right\}^2 - \frac{\alpha_3^2(9 - 8\alpha_1)}{16(\alpha_1 - \alpha_1^2)^2}}\right)\Bigg|_{R_0^2}^{R^2} \tag{5}$$

Solution (5) corresponds to the solitary wave solution with infinite support.

When α_1 tends to zero, the angles between separatrices of saddle point O are growing. As a result, at $\alpha_1 = 0$ we observe the transformation of solitary wave into the compacton, i.e., solutions with finite support [22, 23]. These orbits are described by the following expressions

$$R = U_s' = \begin{cases} \sqrt{\dfrac{3}{2\alpha_3}} \sin\dfrac{\Omega s}{3}, & \text{if } \dfrac{\Omega s}{3} \in [0; \pi] \\ 0, & \text{if } \dfrac{\Omega s}{3} \notin [0; \pi] \end{cases} \quad \text{and} \quad U = \begin{cases} 0, & \text{if } \dfrac{\Omega s}{3} \in [-\infty; 0], \\ \dfrac{3}{\Omega}\sqrt{\dfrac{3}{2\alpha_3}}\left(1 - \cos\dfrac{\Omega s}{3}\right), & \text{if } \dfrac{\Omega s}{3} \in (0; \pi], \\ \dfrac{6}{\Omega}\sqrt{\dfrac{3}{2\alpha_3}}, & \text{if } \dfrac{\Omega s}{3} \in (\pi; \infty). \end{cases}$$

As above, if $-0.09 = -\frac{(1-\alpha_1)^2\Omega^2}{4\alpha_3} < H < 0$, periodic orbits enclosed in the homoclinic loops exist, if $H > 0$, periodic trajectories lie beyond the homoclinic contour.

(a)   (b)
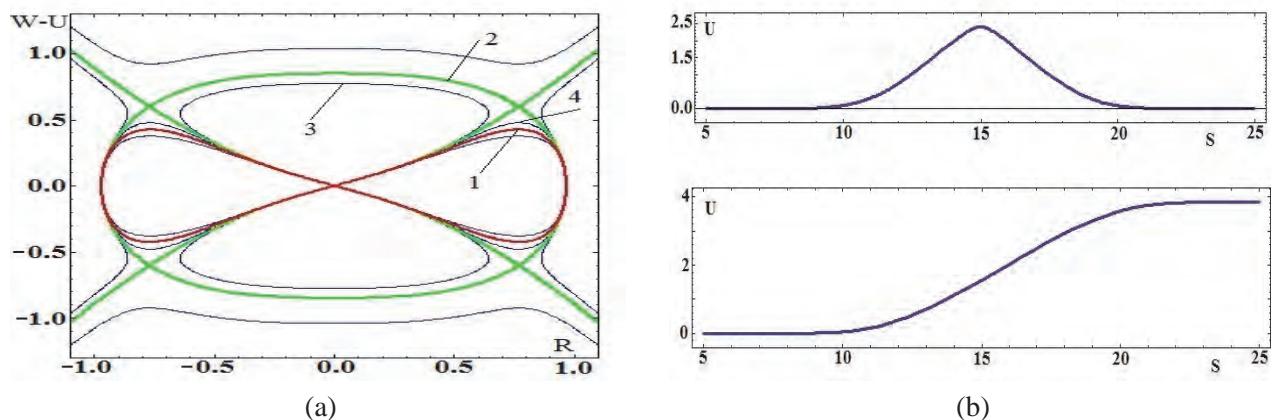
Fig. 2 Left: Position of level curves $I(\delta) = 0$ at different values of δ. Curve 1 is plotted at $\delta = 0$, curve 2 at δ_0, curve 3 at $\delta = -2.7 < \delta_0$, curve 4 at $\delta = -1.5 > \delta_0$. Right: Homoclinic trajectories from the left diagram corresponding to $\delta = -2.7 < \delta_0$ (upper panel) and $\delta = -1.5 > \delta_0$ (lower panel).

1.2   Phase diagrams in the model with cubic nonlinearity in the equation of motion for oscillating inclusions

If $\delta \neq 0$, then system (3) does not reduce to the dynamical system in the plane $(R; R')$. But the first integral for (3) can still be derived in the form

$$I = \frac{\mu_1}{2}(W - U)^4 + \mu_2(W - U)^2 + f(R), \tag{6}$$

where $\mu_1 = \delta D^{-2}$, $\mu_2 = \omega^2 D^{-2}$, $f(R) = \alpha_3^2 R^6 + \frac{4\alpha_1 - 3}{2}\alpha_3 R^4 + (\alpha_1^2 - \alpha_1) R^2$. Since $dI/ds = 0$ on the trajectories of system (3), then $I \equiv$ const.

It is easy to see that expression (6) can be used for splitting system (3). Indeed, solving (6) with respect $W - U$ we obtain

$$W - U = \pm \sqrt{\frac{-\mu_2 \pm \sqrt{\mu_2^2 - 2\mu_1 f(R) + 2\mu_1 I}}{\mu_1}}. \tag{7}$$

This allows us to separate the last equation of (3) from other ones. Unfortunately, the resulting equation cannot be integrated for general case, therefore, let us consider its phase plane structure, which is equivalent to the structure of level curves for function (7).

First of all, consider the position and the form of homoclinic trajectories when the parameter δ is varied. Starting from the loop at $\delta = 0$ which coincides with the orbits of Fig. 1b, we see that increasing δ causes the attenuation of loop's size along vertical axis. Actually, the level curve consists of the closed curve (homoclinic loops) and unbounded trajectories. If δ decreases, loop's size grows, but at δ_0 the additional heterocycle connecting four new saddle points appears. The bifurcational value δ_0 can be derived via analyzing the function (7). Namely, δ_0 corresponds to the moment when different branches of (7) are tangent. This happens when $\mu_2^2 - 2\mu_1 f(R) = 0$. Thus, the condition of contact for two branches leads us to a cubic equation with respect to R^2 with zero discriminant. Then $\delta_0 = -\frac{\alpha_3 \omega^4}{D^2(\alpha_1 - 1)^2}$ or $\delta_0 = \frac{27\alpha_3 \omega^4}{D^2 \alpha_1^2 (9 - 8\alpha_1)}$. The last value of δ_0 is not interesting because four branches of (7) degenerate into two ones forming homoclinic loops.

Considering the first value δ_0, we put $D = 0.9$ and derive $\delta_0 = -2.24$. For $\delta > \delta_0$ we have homoclinic loops placed along horizontal axis accompanied by appearing the unbounded curves in the upper and lower parts of diagram. When $\delta < \delta_0$, the homoclinic loops are placed in the vertical quarters of the phase plane, whereas the unbounded orbits appear at the left and at the right sides of diagram (Fig. 2a). Note that the profiles of the
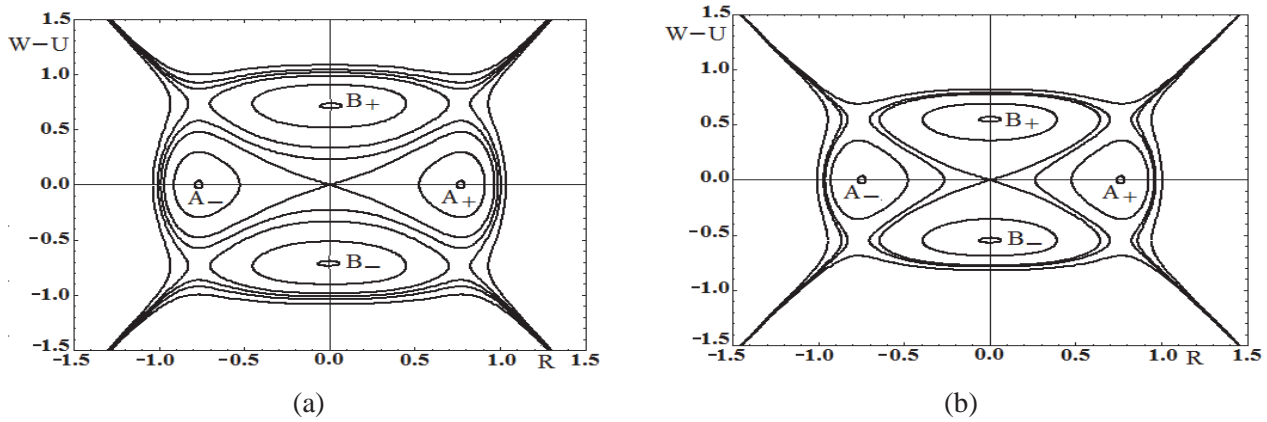
Fig. 3 Phase portraits at $\delta = -1.5$(a) and $\delta = -2.7$(b).

resulting solitary waves are different (Fig. 2b), namely, at $\delta < \delta_0$ the U profile looks like a bell-shape curve, but at $\delta > \delta_0$ it is a kink-like regime.

The homoclinic orbits divide the phase plane into parts filled by closed curves corresponding to the periodic regimes. If we choose $\delta = -1.5 > \delta_0$, we get the typical phase portrait of system (3) plotted in the Fig. 3a. In the portrait two pairs of nontrivial fixed points $A_\pm(\pm Q; 0)$ and $B_\pm(0; \pm \omega/\sqrt{-\delta})$ can be distinguished. Inserting the coordinates of these points into relation (6), we obtain the values of $I_1 = -\frac{(\alpha_1-1)^2}{2\alpha_3}$ and $I_2 = \frac{\omega^4}{2D^2|\delta|}$ which allows us to state the conditions of periodic regimes existence. For fixed $\delta = -1.5$, $I_1 = -0.18$ and $I_2 = 0.27$. We thus get that periodic regimes exist if $I_1 < I < I_2$ only.

Now let us choose $\delta = -2.7 < \delta_0$. In this case the homoclinic loop going through the origin is placed along vertical axis and the phase portrait looks like Fig. 3b. As above, we have $I_1 = -0.18$, but $I_2 = 0.15$.

1.3 The numerical scheme for model (1)

To model the wave dynamics, we construct the three level finite-difference numerical scheme for model (1) and study its stability.

Let us construct the numerical scheme for model (1) in the region $\Sigma = [0 \leq x \leq L] \times [0 \leq t \leq T]$ with grid lines $x = ih$ and $t = j\tau$, where h, τ are constant, $i = 1, ..., N$. Consider three level numerical scheme. Denote $u = u(t_{j+1})$, $v = u(t_j)$, $q = u(t_{j-1})$, and $K = w(t_{j+1})$, $G = w(t_j)$, $F = w(t_{j-1})$. We use the following difference approximation of derivatives

$$\frac{\partial^2 u}{\partial t^2} \approx \frac{u_i - 2v_i + q_i}{\tau^2}, \quad \frac{\partial^2 u}{\partial x^2} \approx r\frac{u_{i-1} - 2u_i + u_{i+1}}{h^2} + (1-r)\frac{v_{i-1} - 2v_i + v_{i+1}}{h^2},$$

$$\frac{\partial u}{\partial x} \approx \frac{v_{i+1} - v_{i-1}}{2h}, \quad \frac{\partial^2 w}{\partial t^2} \approx \frac{K_i - 2G_i + F_i}{\tau^2}, \quad w - u \approx \frac{3G_i - F_i}{2} - \frac{3v_i - q_i}{2} \equiv \psi_i.$$

Thus, if $r \neq 0$, then we obtain the three level implicit scheme:

$$A_i u_{i-1} + C_i u_i + B_i u_{i+1} = Y_i, \quad K_i = 2G_i - F_i - \tau^2 \omega^2 \psi_i - \tau^2 \delta \psi_i^3, \tag{8}$$

where $A_i = B_i = \frac{r}{h^2}\varphi$, $C_i = -2\frac{r}{h^2}\varphi - \frac{1}{\tau^2}$, $\varphi = \rho^{-1}(e_1 + 3e_3(\frac{v_{i+1}-v_{i-1}}{2h})^2)$,
$Y_i = -(\varphi\frac{v_{i-1}-2v_i+v_{i+1}}{h^2}(1-r) + m\omega^2\psi_i + m\delta\psi_i^3 + \frac{2v_i-q_i}{\tau^2})$.

System of algebraic equations (8) can be solved by the sweep method. The necessary conditions of the sweep method stability ($|A_i| + |B_i| \leq |C_i|$) are fulfilled. To get the restrictions for spatial and temporal steps, the Fourier stability method, being applied to linearized scheme (8), is used. Let us fix the values of the parameters
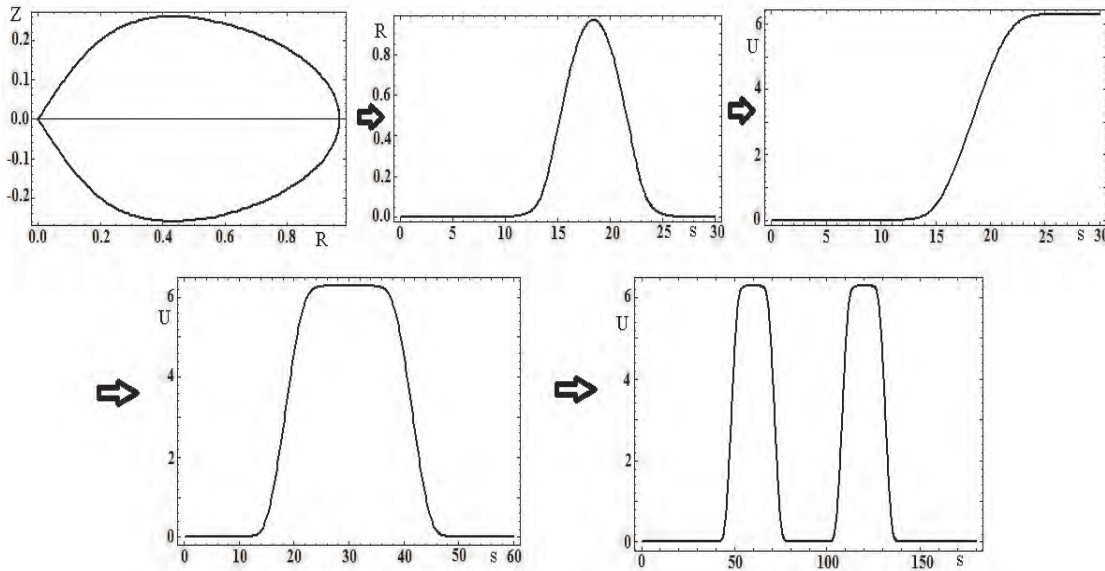
Fig. 4 The construction of initial data for numerical scheme.
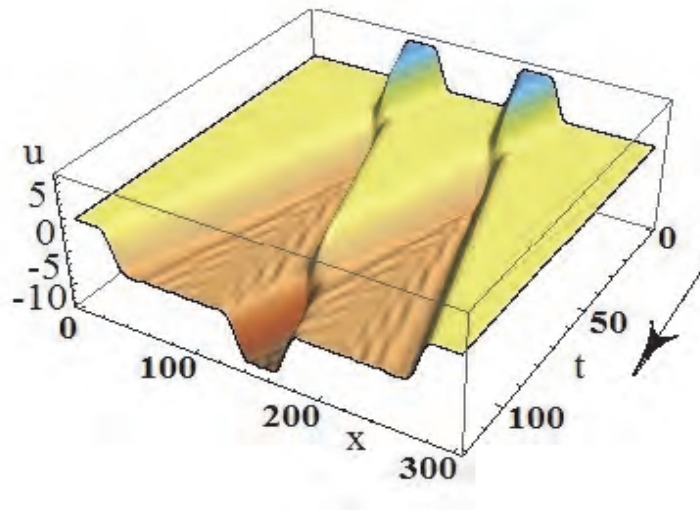
Fig. 5 The propagation of solitary waves at $\delta = 0$ starting from the initial profile depicted in Fig. 4.

$e_1 = 1$, $e_3 = 0.5$, $\rho = 1$, $\omega = 0.9$, $m = 0.6$, $D = 0.9$, and the parameters of the numerical scheme $L = 30$, $N = 200$, $r = 0.3$, $h = L/N$, $\tau = 0.05$.

Solitary waves. Let us construct the initial data v_i, q_i, G_i, F_i for numerical simulation on the base of solitary waves. To do this, we integrate dynamical system (4) with initial data $R(0) = 10^{-8}$, $Z(0) = 0$, $s \in [0;L]$ and choose the right homoclinic loop in the phase portrait (Fig. 1b). Then the profiles of $W(s)$, $U(s)$, and $R(s)$ can be derived. Joining the proper arrays, we can build the profile in the form of arch:

$$v = U(ih) \cup U(L - ih), q = u(x + \tau D) = [U(ih) + \tau DR(ih)] \cup [U(L - ih) + \tau DR(L - ih)].$$

The arrays G and F are formed in similar manner. Combining two arches and continuing the steady solutions at the ends of graph, we get more complicated profile. The sequence of steps for profile construction is depicted
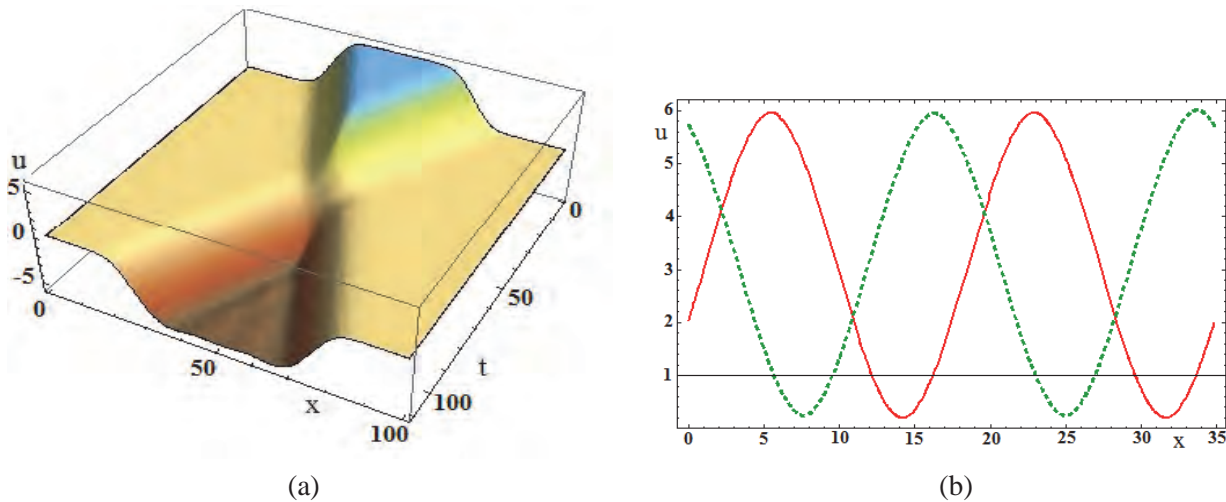
Fig. 6 Collision of solitary waves (a) and evolution of periodic wave (b) at $\delta = -0.2$.

in the Fig. 4 in detail. We apply the fixed boundary conditions, i.e. $u(x = 0, t) = v_1$, $u(x = Kh, t) = v_K$, where K is the length of an array.

Starting from the two-arch initial data, we see (Fig. 5) that solitary waves move to each other, vanish during approaching, and appear with negative amplitude and shift of phases. After collision in the zones between waves some ripples are revealed. Secondary collisions of waves are watched also. Note that the simulation of compacton solutions displays similar properties.

Propagation of solitary waves at $\delta \neq 0$ depends on the sign of δ. Numerical simulations show that the collision of waves at $\delta > 0$ is similar to the collision at $\delta = 0$. Behavior of waves after interaction does not change essentially when $\delta < 0$ and close to zero (Fig. 6a). But if δ is not small, after collision the amplitude of solution is increasing in the place of soliton's intersection and after a while the solution is destroyed [12].

This suggests that we encounter the unstable interaction of solitary waves or the numerical scheme we used possesses spurious solutions. But if we take half spatial step and increase the scheme parameter r up to 0.8, the scenario of solitary waves collision is not changed qualitatively. Therefore, the assertion on the unstable nature of collision is more preferable.

Periodic waves. To simulate the evolution of periodic waves, we take the initial profile corresponding to a periodic orbit (red curve in Fig. 6b) surrounding the homoclinic loop at the phase portrait of Fig. 3a at $\delta = -0.2$ and $D = 0.9$. Due to the periodicity of the problem, the boundary conditions for numerical scheme (8) should be modified. At the ends of interval $0 < x < L$, where $L = 34.86$ is multiple of wave period, we impose the periodic conditions: $u(0, t) = u(L, t)$, $u_x(0, t) = u_x(L, t)$, and $w(0, t) = w(L, t)$, $w_x(0, t) = w_x(L, t)$. Thus, system (8) must be supplemented by the relations $u_1 = u_N$, $u_1 - u_2 = u_{N-1} - u_N$, $K_1 = K_N$, and $K_1 - K_2 = K_{N-1} - K_N$. Remark also that, in turn, the scheme (8) becomes the stiffer as δ decreases and, therefore, one should to increase the scheme parameter r up to 0.8. The resulting profile derived after time interval 1200τ has passed is depicted in Fig. 6b with dark green curve. It is obvious that this wave is shifted a distance $1200\tau D$ to the right in a self-similar manner.

2 Conclusions

In this report, we have presented the studies of cubically nonlinear generalization of model for media with oscillating inclusions. It turned that this model possesses a large variety of traveling wave solutions type of which depends crucially on the parameters of nonlinearity and wave velocities. In particular, if the velocity

of wave D tends to the velocity of sound in medium $\sqrt{e_1/\rho}$, i.e. $\alpha_1 \to 0$, the solitary wave with unbounded support converted into compactly supported wave pulse. Model (1) is the basis for studying the processes of self-organization in heterogeneous nonequilibrium media [24].

Dealing with model (1) we encounter the well-known problem of application of phenomenological model to specific medium. General recommendations for the identification of the considered model had been developed in [15]. Meanwhile, the parameter e_3 is related to the fourth order elastic moduli from the nine-constants Murnaghan model [25]. In general, there is little available information on high order elastic moduli. They can be derived within the solid state physics approach [26] or be estimated experimentally [4, 27]. Moreover, the high order elastic moduli are not necessarily small [25], especially for geophysical media. The parameters ω and δ in model (1) can be associated with the characteristics of grains or clusters in a medium [6].

From the other hand, the shape of these waves, especially solitary ones, depend on the parameters, e.g. ω, δ, characterizing the intrinsic material structure. This seems to be useful for diagnostics of media by means of nondestructive techniques [4], for modeling the behavior of complex media in vibrational fields, for instance when we deal with the intensification of extracting oil and natural gas [16].

To study the properties of solitary waves and their interactions, we have proposed the effective numerical scheme based on the finite difference approximation of the continuous model. In particular, we have analyzed the conditions when the stable propagation of solitons and their collisions are observed. It turned out that the nonlinearity of the oscillating dynamics describing by Φ affects not only the form of solitary waves but their stability properties in collisions. Finally, there are solitary waves moving without preserving of their self-similar shapes. While the numerical results concerning the stable properties of single solitary wave can be confirmed by analytical treatments [28], the studies of wave collisions require mostly the application of improved numerical schemes.

Acknowledgements

References

[1] Rodionov, V.N. (1996), *An Essay of Geomechanics*, Nauchnyi Mir, Moscow.
[2] Sadovskyi, M.A. (1986), Self-similarity of geodynamical processes, *Herald of the RAS*, **8**, 3-12.
[3] Nazarov, V.E. and Radostin, A.V. (2015), *Nonlinear Acoustic Waves in Micro-inhomogeneous Solids*, John Wiley: United Kingdom.
[4] Guyer, R.A. and Johnson, P.A. (2009), *Nonlinear Mesoscopic Elasticity: The Complex Behaviour of Granular Media including Rocks and Soil*, John Wiley: Weinheim.
[5] Danylenko, V.A., Danevych, T.B., Makarenko, O.S., Skurativskyi, S.I., and Vladimirov, V.A. (2011), *Self-organization in nonlocal non-equilibrium media*, Subbotin in-t of geophysics NAS of Ukraine: Kyiv.
[6] Nikolaevskij, V.N. (1989), Dynamics of viscoelastic media with internal oscillators, Lecture Notes in Engineering 210, **39**, Springer: Berlin.
[7] Slepjan, L.I. (1967), Wave of deformation in a rod with flexible mounted masses, *Mechanics of Solids*, **5**, 34-40.
[8] Palmov, V.A. (1969), On a model of medium of complex structure, *Journal of Applied Mathematics and Mechanics*, **4**, 768-773.
[9] Danylenko, V.A. and Skurativskyi, S.I (2008), Resonance regimes of the spreading of nonlinear wave fields in media with oscillating inclusions, *Reports of NAS of Ukraine*, **11**, 108-112.
[10] Danylenko, V.A. and Skurativskyi, S.I. (2012), Travelling wave solutions of nonlocal models for media with oscillating inclusions, *Nonlinear Dynamics and Systems Theory*, **4**(12), 365-374.
[11] Skurativskyi, S.I. (2014), Chaotic wave solutions in a nonlocal model for media with vibrating inclusions, *Journal of Mathematical Sciences*, **198**(1), 54-61.

[12] Danylenko, V.A. and Skurativskyi, S.I. (2015), On the dynamics of solitary wave solutions supported by the model of mutually penetrating continua, *Dynamical systems. Mechatronics and life sciences*, **2**, 453-460. (arXiv:1512.05226v1 [nlin.PS] 15 Dec 2015)

[13] Samsonov, A.M. (2001), *Strain solitons in solids and how to construct them*, Chapman and Hall CRC: New York.

[14] Nayfeh, A.H. and Mook, D.T. (1995), *Nonlinear oscillations*, John Wiley: New York.

[15] Palmov, V. A. (1998), *Vibrations of Elasto -Plastic Bodies*, Springer-Verlag: Berlin.

[16] Nikolaevskiy, V.N. (1989), Mechanism and dominant frequencies of vibrational enhancement of yield of oil pools, *USSR Acad. Sci., Earth Science Sections*, **307**, 570-575.

[17] Beresnev, I.A. and Nikolaevskiy, V.N. (1993), A model for nonlinear seismic waves in a medium with instability, *Physica*, **66D**, 1-6.

[18] Nigmatulin, R.I. (1991), *Dynamics of Multiphase Media*, (Volume 2), Hemisphere Publishing Corporation: New York.

[19] Gamburtseva, N.G., Nikolaev, A.V., Khavroshkin, O.B. and Tsyplakov, V.V. (1986), Solitonic properties of teleseismic waves, *Transactions of Acad. of Sc. of USSR*, **291**(4), 814-816.

[20] Danylenko, V.A., Skurativskyi, S.I. and Skurativska, I.A. (2014), Asymptotic wave solutions for the model of a medium with Van Der Pol oscillators, *Ukrainian Journal of Physics*, **59**(9), 932-938.

[21] Skuratovskii, S.I. and Skuratovskaya, I.A. (2010), Localized autowave solutions of the nonlinear model of complex medium, *Electronic Journal "Technical Acoustics"*, **6**, http: ejta.org.

[22] Hyman, J. and Rosenau, Ph. (1993), Compactons: solitons with finite wavelength, *Phys. Rev. Lett.*, **70**, 564.

[23] Vladimirov, V.A. and Skurativskyi, S.I. (2015), Solitary waves in one-dimensional pre-stressed lattice and its continual analog, *Dynamical systems. Mechatronics and life sciences*, **2**, 531-542. (arXiv:1512.06125v1 [nlin.PS] 18 Dec 2015)

[24] Danylenko, V.A. and Skurativskyi, S.I. (2016), Peculiarities of wave dynamics in media with oscillating inclusions, *International Journal of Non-Linear Mechanics*, **84**, 31-38.

[25] Porubov, A.V. and Maugin, G.A. (2009), Cubic non-linearity and longitudinal surface solitary waves, *International Journal of Non-Linear Mechanics*, **44**, 552-559.

[26] Potapov, A.I. (2005), Strain waves in a medium with internal structure, Eds. Gaponov-Grekhov A.V., Nekorkin V.I., *Nonlinear Waves'2004*, Institute of Applied Physics RAS: Nizhny Novgorod.

[27] Payan, C., Garnier, V., and Moysan, J. (2009), Determination of third order elastic constants in a complex solid applying coda wave interferometry, *Applied Phys. Lett.*, **94**, 011904.

[28] Vladimirov, V., Maczka, C., Sergyeyev, A., and Skurativskyi, S.I (2014), Stability and dynamical features of solitary wave solutions for a hydrodynamic type system taking into account nonlocal effects, *Commun. in Nonlinear Science and Num. Simul.*, **19**(6), 1770-1782.

Design of a Tracking Controller for Object Interception in Space

Elżbieta Jarzębowska[†], Bartłomiej Pilarczyk

Institute of Aeronautics and Applied Mechanics, Warsaw University of Technology, Nowowiejska 24,
00-665 Warsaw, Poland

Abstract

The paper presents a model-based tracking controller design for a free-floating space robot for a mission scenario of intercepting an object. Such missions are of interest due to a growing number of objects needed to be removed from space. The free-floating mode requires spacecraft thrusters to be off and linear and angular momentum are conserved then. Momentum conservation generates holonomic and nonholonomic constraint equations, respectively. The free-floating mode implicates underactuation, so the robot becomes multi-constrained. Many control algorithms are designed for underactuated robots but they are specific mission and robot dependent. Motivations for the presented research come from the growing space exploration, which results in more space debris and requires sophisticated removal services. Service tasks and debris removal need to be performed by specialized robots. The debris interception scenario presented in the paper consists of estimation of target properties, a controller design to track and intercept the debris, and move it to the graveyard orbit. Simulation results of the theoretical control development for the robot intercepting a non-tumbling object are provided.

©2017 L&H Scientific Publishing, LLC. All rights reserved.

1 Introduction

The paper presents some results on designing model-based tracking controllers for a free-floating space robot dedicated to perform maintenance tasks. The focus of this research is on capturing objects, e.g. debris in space. We design a mission scenario for intercepting small debris in space and move it safely to a graveyard orbit or vehicle disposable containers. Such missions are of a significant interest due to a growing number of debris and other space objects needed to be removed from space, as well as due to asteroids which, when captured, may be promising sources of raw materials.

A free-floating operation mode requires spacecraft thrusters to be turned off and the robot linear and angular momenta are conserved. The condition of linear momentum conservation generates the holonomic constraint on the robot. However, due to the angular momentum conservation the space robot is a nonholonomic control system. The free-floating mode implicates that the robot is underactuated. In control setting, underactuation is

---

[†]Corresponding author.
  Email address: elajarz@meil.pw.edu.pl

treated as a second order nonholonomic constraint, so the free-floating space robot is a multi-constraint control system [1, 2].

Motivations for undertaking this research are of potential significance of its results in the future, in the face of constantly growing interest in conquest and exploration of space. The growing space exploration results in generation of more space debris and requires sophisticated removal services [3]. The latter ones are often delivered by astronauts, like in Extra Vehicular Activities (EVA). Debris moving in space may cause danger for operating satellites and need to be removed successively. Small debris, which are of interest of this paper, can be captured by space robots using robot hands, leashes or nets, and the bigger ones require removal including docking of a space robot to them, flying in a formation maneuver and then, bringing the debris, e.g. to Earth.

Both, services in space and debris removal, need to be performed by specialized space robots. Also, this research, through a development of new control strategies for space robots may provide a new insight into nonlinear control methods for missions in space.

Control properties of space robots, as mentioned earlier, and missions planned for them make the control design an interesting and quite challenging problem. Although there already exist algorithms which allow controlling underactuated robots and manipulators [4–6], there are still many open problems and room for new research in this area, since controllers are usually dedicated to specified missions and space robots performing them. Thus, some more general mission oriented approaches are welcome.

The paper presents a development of space robot control oriented dynamics. Based upon the dynamics a model based controller is developed to serve a debris interception mission. The mission scenario consists of three main steps: (a) estimation of a moving target motion using long and short range distance cameras, sizing and approximating its inertia; (b) design of a controller to track and intercept the moving target; (c) safely move the moving target the graveyard orbit.

This research provides a theoretical control development for approaching, capturing and acquisition of an object. The assumptions are that the space robot is supposed to track and capture an object of a relatively small size with respect to that of the robot, and which does not tumble. The theoretic development is illustrated by the mission simulation studies.

The research contribution is two–folded. Firstly, intercepting a slowly moving, non-tumbling object, may provide us some insight into a selection of simple and effective control algorithms for this mission. Secondly, a space robot dynamics after an object interception may be monitored. The presented research provides and extension of what is presented in [1]. Specifically, the research results may provide a better insight into the space robot stable motion due to an object size, weight and kind of its motion. Additionally, the results may contribute to a control theoretic basis for future applications in space or for ground manipulators when an extra load is intercepted or one of their actuators fail.

2 Formation types

Spacecraft formations can be categorized according to some of the following properties: precision, size or ambient dynamic character [7]. Categorized by size, the formations can be considered as small ($N \leq 5$) or large ($N \geq 20$), where N is the number of spacecraft in the formation. Based on the precision, formations can be divided into those representing high precision or low precision. High precision means operating on the level of centimeters and low precision formations precision is greater than meters [7, 8]. The last mentioned category is based on the environment in which formations operate. This may be a Deep Space or Planetary Orbital Environment.

A different type of distinction may be done based on the structure of the spacecraft formation. According to Scharf et al. [7] five different architectures can be distinguished. These are: Leader/Follower; Multiple-Input Multiple-Output, Virtual Structure, Behavioral and Cyclic.

Thanks to the hierarchical arrangement of controllers, the Leader/Follower structure reduces the formation control to individual tracking problems [9]. This basically means that the state of the follower-spacecraft depends

on the leader. There are two approaches used most often to achieve this: (a) the follower spacecraft tracks the state between the leader and the follower; (b) reference trajectory for the follower is based on the state of the leader.

Multiple–input multiple-output (MIMO) controllers are designed with respect to a dynamical model of the whole formation. Thus, a number of methods can be applied to control this type of formation.

Another type of a formation is called Virtual Structure. Within this type of a system, a spacecraft formation behaves as a collection of rigid bodies embedded in a bigger virtual structure. In this type of architecture positions of spacecraft and motions of virtual structures are used in order to define reference trajectories. Controllers of every spacecraft are used to follow the generated paths.

One more possibility of controlling a spacecraft formation is Cyclic. Although it may seem that it is the same as the Leader/Follower strategy, it slightly differs. In this case, interconnections between controllers are not hierarchical. Cyclic architecture is actually very complex, since the dependency cycles add higher levels of feedback to the controllers of individual spacecraft. One of possible control algorithms for Cyclic architecture may be based on the flocking algorithm. This behavior may be observed in nature among groups of animals. Briefly, this behavior may be characterized as follows: each animal is attracted to a distant neighbor; is repulsed by near-by neighbors and follows the velocity of neighboring animals [7].

Last of the algorithms mentioned above is called Behavioral. This one is characterized by certain behaviors which are presented by a spacecraft. A formation as a whole may represent several behaviors: maintaining a formation, avoiding obstacles, moving towards an object or avoiding collisions. Unfortunately, there may be certain behaviors which lead to collisions of the spacecraft in the formation.

3 Control mission protocol

A mission of capturing a moving target – a debris, precisely its very end part, consists of approaching the target, following it, capturing and getting away. The main assumptions and objectives taken into consideration during the control mission protocol design are as follows:

- The space robot dynamic model is control oriented and developed with respect to the mass center of the system.

- The space robot is supposed to track and capture a moving target of a relatively small size, about a diameter of 10 cm, with respect to that of the robot, and which does not tumble.

- The debris weight is small comparing to that of the robot. Intercepting the moving target adds additional mass to the system what may significantly change its dynamics and move it out of its orbit. We assume that the debris weight does not affect the robot motion.

- The debris is assumed to move with a speed of not more than 7km/s.

The debris inertia can be determined:

- The debris motion is monitored and estimated with the help of cameras. It is assumed that image processing algorithms allow obtaining information from the still picture, as well as from a live video feed. Thus, the size of the debris can be determined.

- The debris mass can be approximated based upon its dimensions, volume, and assuming its density.

- A distance change between the robot and the target, using stereo vision or a depth camera, can be determined. Based on this, relative motion of the target can be approximated.

- Motion of the debris can be estimated using cameras so the robot can follow it, track it and grasp by its end effector.
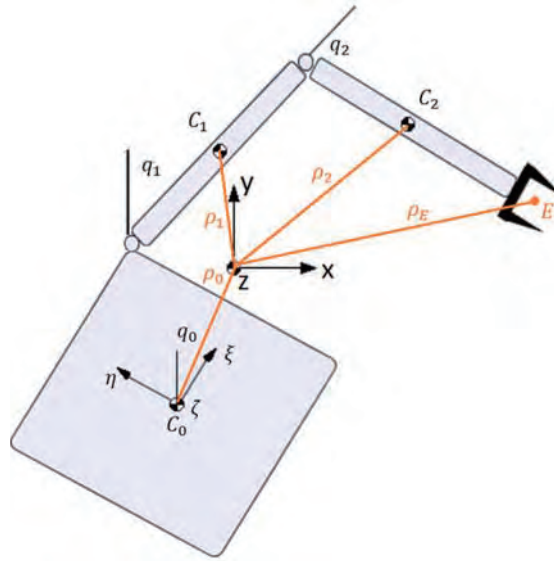
Fig. 1 Representation of the space robot model

Table 1 Physical parameters of the space robot

Body No.	a_i [m]	l_i [m]	m_i[m]	I_i [kgm^2]
0	1	0.5	40	6.667
1	1	0.5	4	0.333
2	1	0.5	3	0.250

The research scope as presented does not cover launching of the robot and putting it in the orbit. It is assumed that the robot can reach the debris and it may approach to it at the reachable distance.

The assumptions stated above allow us to distinguish the phases interesting for the research, i.e. approaching, intercepting and moving safely away with the debris to the mission destination. Also, they enable performing the dynamics and control analysis using data delivered by on-board devices.

4 A space robot dynamic model

The space robot adapted in this paper is a space manipulator consisting of a base and two arms; see Fig. 1.

Although the robot is assumed to be three dimensional, limitations of its motion to the (x,y) plane are applied. The joints can then rotate around the z axis. The space robot is equipped with a 2D arm since it is easier to design, manufacture and control it. It is enough to have such arm for specialized tasks. Geometric and inertia robot parameters are provided in the Table 1.

The space robot motion is described by the joint coordinate vector $q = [q_0, q_1, q_2]^T$. The symbols C_0, C_1, C_2 denote centers of mass of each body in the system. Vectors ρ_0, ρ_1, ρ_2 define positions of the centers of masses, where $\rho_i = [\xi, \eta, \zeta]^T$. Also, ρ_E is a position vector for the end effector of the robot arm.

Conservation of the angular momentum for space vehicles results in a nonholonomic constraint equation. The formula of the angular momentum for a single body in 3 dimensions is denoted as follows:

$$K_i = \rho_i \times m_i \dot{\rho}_i + I_{ii} \omega_i \tag{1}$$

where ρ_i is a vector specifying a distance between the center of mass of the *i-th* body and the center of mass of the whole system, m_i is the mass of the *i-th* body, I_{ii} is the matrix of moments of inertia of the *i-th* body

with respect to central principal axes and ω_i is the vector of angular velocity of the *i-th* body. The conservation condition requires the sum of angular momenta of all the bodies in the system to be constant. If the engines are turned off, the spacecraft drifts and we may assume this sum to be zero. Taking into account the applied notation, the angular momentum vector depends upon the angular positions q and the angular velocities $\dot{q}$. Thus, the formula for angular momentum conservation can be written as follows:

$$\mathbf{K} = \mathbf{K_0} + \mathbf{K_1} + \mathbf{K_2} = \mathbf{\Phi}(q_0, q_1, q_2, \dot{q}_0, \dot{q}_1, \dot{q}_2) \tag{2}$$

Although, the model of the robot is three-dimensional, the motion of the robot is limited in this study, i.e. rotation only around the z axis is available. Therefore, equation (1) can be written in a simplified form:

$$K_i = \rho_i \times m_i \dot{\rho}_i + I_{i\zeta\zeta}\omega_{iZ} \tag{3}$$

where $I_{i\zeta\zeta}$ is the inertia tensor of the *i*-th body and ω_{iZ} is the angular velocity component of the *i*-th body around the axis perpendicular to the plane in which the motion takes place. The angular velocity of each body can be written as the sum of time derivatives of the rotational angles:

$$\begin{aligned} \omega_0 &= \dot{q}_0, \\ \omega_1 &= \dot{q}_0 + \dot{q}_1, \ \omega_2 = \dot{q}_0 + \dot{q}_1 + \dot{q}_2 \end{aligned} \tag{4}$$

Total kinetic energy of the system can be then computed as follows:

$$T = 0.5[m_0(\dot{x}_0^2 + \dot{y}_0^2) + I_{0CoM}\omega_0^2 + m_1(\dot{x}_1^2 + \dot{y}_1^2) + I_{1CoM}\omega_1^2 + m_2(\dot{x}_2^2 + \dot{y}_2^2) + I_{2CoM}\omega_2^2] \tag{5}$$

where $\dot{x}_i, \dot{y}_i$ are linear velocity components of the centers of masses of the robot components. I_{iCoM} is the moment of inertia around the z axis, with respect to the center of mass of the system. Its magnitude is as follows:

$$I_{iCoM} = I_i + m_i d_i^2 = I_i + m_i(x_i^2 + y_i^2) \tag{6}$$

Motion of the system can be described by the Lagrange equations which yield:

$$\mathbf{M}(\mathbf{q})\ddot{\mathbf{q}} + \mathbf{C}(\mathbf{q}, \dot{\mathbf{q}})\dot{\mathbf{q}} = \tau + \mathbf{J_0^T}\lambda \tag{7}$$

Furthermore, the unknown Lagrange multipliers are decoupled from the control momenta which results in the reduced form of the equations. This procedure is applied to general nonholonomic systems in order to obtain dynamical control models for them. The equations decoupling results in

$$\mathbf{M_{12}}(\mathbf{q})\ddot{\mathbf{q}}_2 + \mathbf{C_{12}}(\mathbf{q}, \dot{\mathbf{q}}_2)\dot{\mathbf{q}}_2 = \tau + \mathbf{J_1^T}\lambda \tag{8}$$

$$\begin{aligned} \mathbf{M_{22}}(\mathbf{q})\ddot{\mathbf{q}}_2 + \mathbf{C_{22}}(\mathbf{q}, \dot{\mathbf{q}}_2)\dot{\mathbf{q}}_2 &= \tau; \\ \dot{\mathbf{q}}_1 &= \mathbf{D}(\mathbf{q})\dot{\mathbf{q}}_2 \end{aligned} \tag{9}$$

where $q_1 = [q_0]$ and $q_2 = [q_1, q_2]^T$. Equations (8) and (9) form the system dynamical control model, where τ are control forces that come from controllers. This control model is applied for computation of the control torques and applied to simulation of the target tracking. All computations are conducted in MatLab environment. In this research only the angles q_1 and q_2 are controlled. Orientation of the base, q_0, is not controlled, i.e. the spacecraft is underactuated. Thus, $\tau_0 = 0$ and the only acting torques are τ_1 and τ_2. The angular momentum conservation plays the role of the constraint equation so Eq (9) looks like the dynamic control model of a nonholonomic system. In the control setting, underactuated systems are treated as nonholonomic control systems.
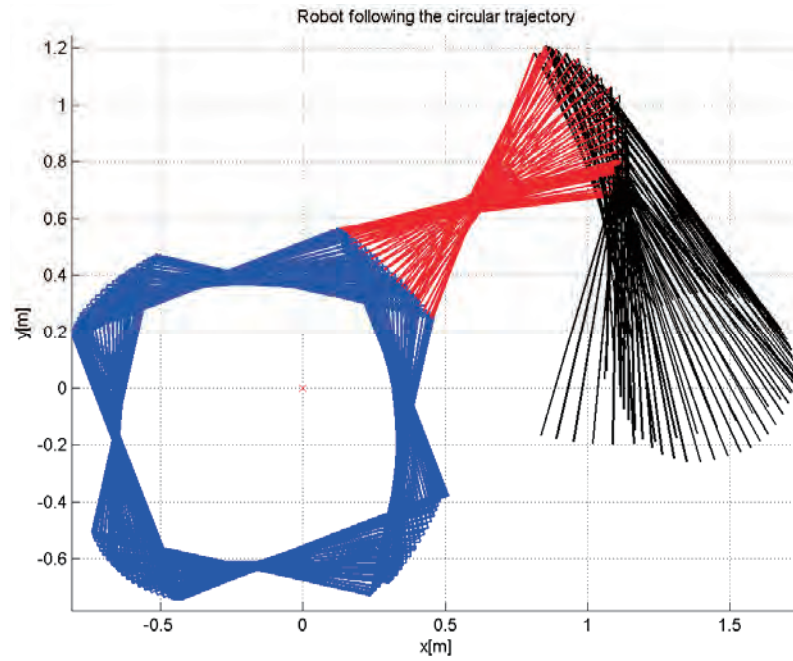
Fig. 2 Robot motion tracking a circular trajectory.
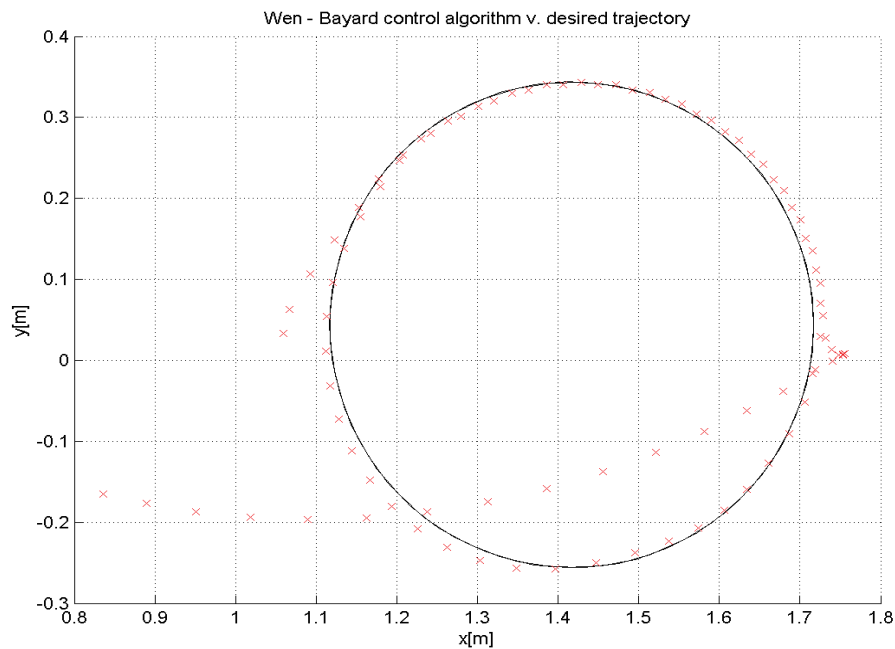
Fig. 3 End effector tracking a circular trajectory.

5 Results of a space robot simulation

The Wen-Bayard control algorithm is the computed torque type controller. It requires the complete knowledge of the system dynamics. However, its significant advantage over some other algorithms, e.g. computed torque, is that the mass matrix does not have to be non-singular. The Wen-Bayard control algorithm was introduced first for holonomic systems [10]. It has been adapted to nonholonomic systems in [11]. This adapted control scheme applies to systems as presented by Eqs (9). It is used in this study and it is a novel application of this algorithm,
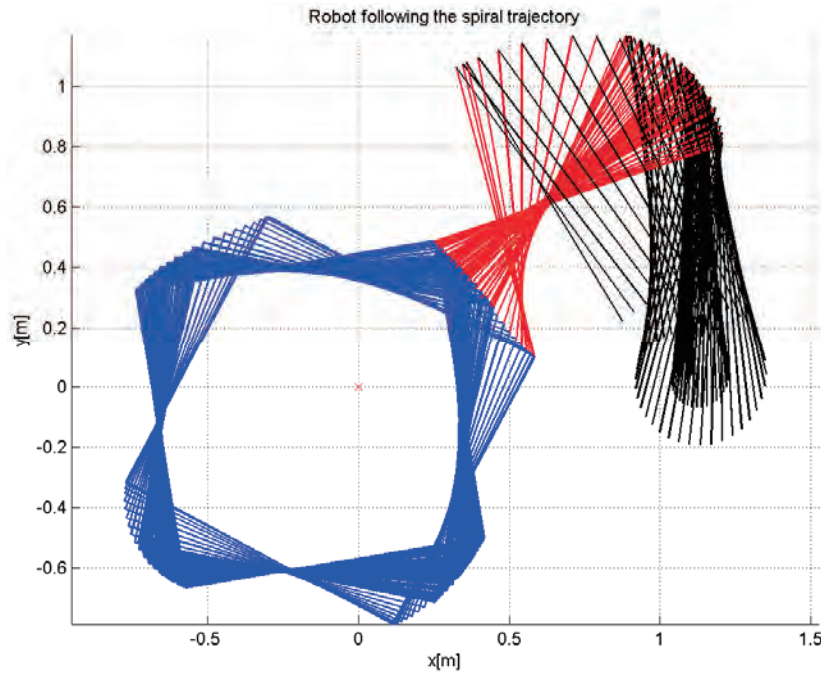
Fig. 4 Robot motion tracking a spiral trajectory.

i.e. application to a space mission of an underactuated system. The reason for its application is the study of its use possibility to this class of problems.

Throughout this research two numerical experiments have been performed. In the first one, the end effector of the robot followed an object along a circular trajectory, which is a desired trajectory. In the second experiment, the end effector followed the object moving on a spiral trajectory. Also, it is assumed, as stated in section 3, that the robot can find and approach the target in space, and can start tracking it along its trajectory which was recovered by on the robot board cameras. Tracking is followed by speeding up and capturing the target. Next actions of the robot, which are out of this paper scope, are to move the target to its desired destination, e.g. a graveyard orbit.

Below, the research results are presented. They were obtained via implementation of the Wen-Bayard algorithm. The error function, $e = e(t)$, is defined as

$$e(t) = q(t) - q_d(t) \tag{10}$$

Equation (11) defines the formula for the Wen-Bayard computed torque like controller.

$$\tau = \mathbf{M_{22}}(\mathbf{q})\ddot{\mathbf{q}}_{\mathbf{2d}} + \mathbf{C_{22}}(\mathbf{q_d}, \dot{\mathbf{q}}_{\mathbf{2d}})\dot{\mathbf{q}}_{\mathbf{2d}} - \mathbf{K_d}\dot{\mathbf{e}} - \mathbf{K_p}\mathbf{e} \tag{11}$$

The values of the control gains in diagonal gain matrices $\mathbf{K}_d$ and $\mathbf{K}_p$ were chosen to be: K_d=9 and K_p=9. They are the smallest gains provided fast convergence to the reference moving target trajectory. For nonlinear control dynamics (9) the linear techniques of the gain selections fail so the selection method is rather a trial and error method. Also, notice that the base rotation is controlled indirectly as the second of Equations (9) indicates. It means that its controlled values are provided through the angular momentum conservation equation.

Figure 2 presents the motion of the space robot while tracking the object moving along the circular trajectory. Initial conditions for the circular motion of the end effector are as follows:

$$q_0 = -0.523 \text{ rad}, q_1 = 0 \text{ rad}, q_2 = 1.309 \text{ rad}, \dot{q}_0 = 0 rad/s, \dot{q}_1 = 0 \text{ rad/s}, \dot{q}_2 = 0 \text{ rad/s}$$

In Fig. 3 tracking of the circular trajectory is presented in details. Black line is the desired trajectory to be followed and the crosses show motion of the end effector.
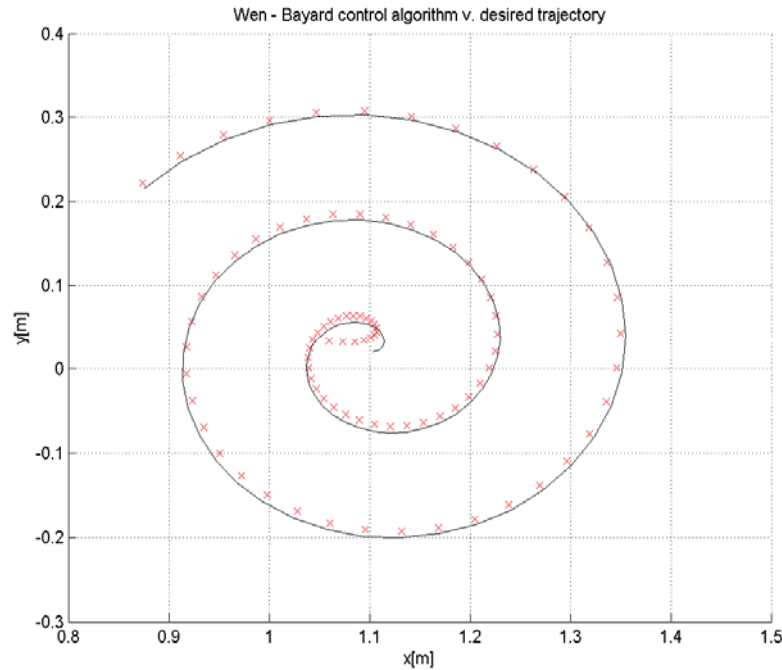
Fig. 5 End effector tracking a spiral trajectory.

Figure 4 shows the motion of the space robot while tracking the object moving along the spiral trajectory. Initial conditions for the spiral motion of the end effector are as follows:

$$q_0 = -0.349 \text{ rad}, q_1 = -0.087 rad, q_2 = 1.832 \text{ rad}, \dot{q}_0 = 0 \text{ rad/s}, \dot{q}_1 = 0 \text{ rad/s}, \dot{q}_2 = 0 \text{ rad/s}$$

In Fig. 5 tracking of the spiral trajectory is presented in details. Black line is the desired trajectory to be followed and the crosses show the way of the end effector.

It can be seen that the Wen–Bayard algorithm produces worse tracking performance comparing to the popular in applications computed torque controller, in which a PD with correction is applied in the inner loop, but its significant advantage over the computed torque is that the inertia matrix does not have to be non-singular. It is of the essential value when capturing debris, since they change inertia properties of a robot-debris system. This is the main reason for applying the Wen–Bayard algorithm for our preliminary capturing mission analysis.

6 Conclusions

Model-based control design for a space robot following, tracking and capturing a moving object was presented in the paper. This was the preliminary study for, what was in fact, formation flying when a robot and an object were of comparable masses. The presented research showed the simulation results of controlling the space vehicle capturing the small debris. The control algorithm used was the Wen-Bayard algorithm applied for the first time to such a mission. The preliminary results were promising and the control algorithm which we used could be applied for tracking different trajectories. Therefore the results obtained in this research were the good starting point for further mission tasks like flying in a robot-debris formation and moving the debris to the graveyard orbit or flying in two-robot carrying a debris and a debris formation. Also, it was the good starting point for development other control strategies, e.g. adaptive, for more complex mission tasks.

References

[1] Jarzębowska, E. and Pilarczyk, B. (2015), A tracking controller design for a space target interception, Proc. DSTA 2015 Conference, Łódź Poland, Dec. 7–10, 263-272.

[2] Vafa, Z. and Dubowsky, S. (1990), The kinematics and dynamics of space manipulators: The virtual manipulator approach, *The International Journal of Robotics Research*, **9**(3), DOI 10.1177/027836499000900401.

[3] Lehnert, Ch. (2011), Space debris removal for sustainable space environment, *ESPI Perspectives*, 52.

[4] Sagara, S. and Taira, Y. (2008), Digital control of space robot manipulators with velocity type joint controller using transpose of generalized Jacobian matrix, *Artificial Life Robotics*, **13**(355-358), DOI 10.1007/s10015-008-0584-7.

[5] Nakamura, Y. and Mukherjee, R. (1991), Nonlinear control for the non-holonomic motion of space robot systems, Advanced Robot Control, *Lecture Notes in Control and Information Sciences*, **162**, 83-105.

[6] Papadopoulos, E.G. (1993), Teleoperation of free–floating space manipulator systems, Proc. SPIE 1833, *Telemanipulator Technology*, **122**, doi:10.1117/12.142103.

[7] Scharf, D.P., Hadaegh, F.Y., and Ploen, S.R. (2004), A survey of spacecraft formation flying guidance and control (Part II): Control, Jet Propulsion Laboratory, California Institute of Technology, Pasadena, CA 9 1 109-8099.

[8] Lennox, S.E. (2004), Coupled Attitude and Orbital Control System Using Spacecraft Simulators, Thesis submitted to the Faculty of the Virginia Polytechnic Institute and State University.

[9] Yang, I., Lee, D., and Han, D.S. Designing a Robust Nonlinear Dynamic Inversion Controller for Spacecraft Formation Flying, Hindawi Publishing Corporation, *Mathematical Problems in Engineering*, **2014**, Article ID 471352, http://dx.doi.org/10.1155/2014/471352

[10] Bayard, D.S. and Wen, J.T. (1988), New class of control laws for robotic manipulators, *Int. J. Control*, **47**(5), 1387-1406.

[11] Jarzębowska, E. (2012), Model-based tracking control of nonlinear systems, *Taylor & Francis Group, Series: Modern Mechanics and Mathematics*, Boca Raton.

[12] Jarzębowska, E. and Pietrak, K. (2011), Control oriented dynamic modeling framework for constrained multibody systems: A Case Study of a Free-Floating Space Manipulator, Proc. *11th DSTA International Conference*, 139-144, Łódź Poland.

Implementation Assessment of a Wave Energy Converter, Based on Fully Enclosed Multi-axis Inertial Reaction Mechanisms

Ioannis A. Antoniadis[1†], Vasilis Georgoutsos[1], Andreas Paradeisiotis[1], Stratis A. Kanarachos[2], Konstantinos Gryllias[3]

[1] Mechanical Design and Control Systems Section, Mechanical Engineering Department, National Technical University of Athens, Heroon Polytechniou 9, 15780 Zografou, Greece

[2] Department of Mechanical, Automotive and Manufacturing Engineering, Faculty of Engineering and Computing, Coventry University, 3, Gulson Road, Coventry, CV1 2JH, UK

[3] Faculty of Engineering, Department of Mechanical Engineering, Division PMA, KU Leuven, Celestijnenlaan 300, BOX 2420, 3001 Leuven, Belgium

Abstract

This paper examines the implementation of a standalone 1 MW Wave Energy Converter (WEC), based on a novel concept of a class of WECs, consisting in fully enclosed appropriate internal body configurations, which provide inertial reaction against the motion of an external vessel. Acting under the excitation of the waves, the external vessel is subjected to a simultaneous surge and pitch motion in all directions, ensuring maximum wave energy capture. The internal body is suspended from the external vessel body in such an appropriate geometrical configuration, that a symmetric four bar mechanism is essentially formed. The first advantage of this suspension geometry is that a linear trajectory results for the center of the mass of the suspended body with respect to the external vessel, enabling the introduction of a quite simple form of a Power Take-Off (PTO) design. The simplicity and symmetry of the suspension geometry and of the PTO, ensure a quite simple and robust technological implementation. Mass and inertia distribution of the internal body are optimized, ensuring maximal conversion and storage of wave energy. As a result, the internal body assembly is essentially, dynamically equivalent to a vertical physical pendulum. However, the resulting equivalent pendulum length and inertia can far exceed those that can be achieved by a simple horizontal or vertical pendulum, suspended or inverted, leading to a significant reduction of the suspended mass.

1 Introduction

Oceans constitute more than 75% of our planet and the waves being produced in them consist one of the biggest untapped renewable energy resources of our world. Various estimates and methodologies with varying figures

---

[†]Corresponding author.
Email address: antogian@central.ntua.gr

exist [1–3], converging however to estimates for a wave power exceeding 2 TW, which is of the same order as global electricity production. Much higher perspectives exist in the hybrid wind-wave energy exploitation. Using only North Sea sites with water over 50 m deep as an example, the energy produced in this area could meet today's EU electricity consumption four times over [4, 5]. An additional potential exists in suitable areas of the Atlantic and Mediterranean seas.

This fact has inspired numerous inventors, as early as 1799, when French engineer Pierre Girard and his son filed the first patent to harness power from waves. The main systematic research effort for efficient wave energy converters was only stimulated by the emerging oil crisis of the 1970s. As a result, more than a thousand of patents and tenths (if not hundreds) of experimental prototypes are being tested in the sea. Some comprehensive recent reviews can be found [6–8].

Today, the main obstacles for efficient wave energy conversion are mainly related to the requirement for survivability in extreme weather conditions, and to the energy efficient and reliable design of the PTO mechanism. This last requirement involves not so much the design of the PTO device itself, but much more its seamless and energy efficient interface and integration with the wave absorption vessel and the electrical grid.

Towards the last direction, numerous concepts of wave energy converter systems have been conceived, consisting from two-body configurations, in which only one body is in contact with the water and the other body is located above the water or is totally enclosed inside the wetted one. This design enables such mechanisms to fulfill in the best possible way a fundamental prerequisite for wave energy converters: the requirement for reliability, robustness and survivability under extreme weather conditions.

The earliest example in this direction are perhaps the Frog and PS Frog designs at the University of Lancaster in England [9, 10]. Frog actually refers to a heaving absorber, while PS Frog refers to a combined surging and pitching absorber, all actually resulting to a PTO mechanism in the form of a linear sliding mass, enclosed inside a floating vessel. Parallel, an approach for the theoretical modeling and control of such devices has been performed in [11, 12], essentially for the heaving ones. An interesting variant of this design, acting essentially in the form of a vertical pendulum has been proposed: the SEAREV [13] concept. The basic disadvantages of these two designs consist in their limited capability for wave capture in a single axis and in the big masses they require for efficient energy capture, thus demanding complex and unreliable support structures.

Other designs in the forms of an inverted pendulum have been proposed [14], which however result to unstable structures, possibly extended quite high above the sea level. Parallel, horizontal pendulum designs [15, 16] have been proposed, which however introduce problems of stability of the external vessel, only partially compensated by asymmetric ballast designs. Quite recently, the GAIA multi-axis wave energy converter has been also proposed [17]. However, it still requires a complicated support structure and PTO mechanisms.

An interesting variant of such concepts is the class of designs, which make use of a gyroscope as an internal reacting inertial configuration [18–22]. However, no systematic analysis exists on the requirements for significant energy capture by such designs, in terms of rotating masses and corresponding speeds. Furthermore, their complexity consists a further serious disadvantage for their reliability and robustness in the harsh sea environments.

The novel concept for the design of a general class of fully enclosed internal body configurations introduced in [23], providing inertial reaction against the motion of an external vessel, is able to drastically overcome the disadvantages of the above designs. Acting under the excitation of the waves, the external vessel can perform in general a 6 DOFs arbitrary translation and rotation of in space.

The internal bodies are suspended from the external body in such appropriate geometrical configurations, that the entire assembly of the internal and external bodies, together with their suspension systems, form essentially a multilink mechanism. The kinematic design of these mechanisms can be performed in such a way, that the internal bodies can follow a well prescribed relative motion with respect to the external body. Moreover, each individual body has an optimal mass and inertia distribution.

This overall design enables the maximum conversion and storage of wave energy from all the degrees of freedom of the external body, into the form of kinetic and potential energy, stored into the total assembly of

the internal bodies. Moreover, since specific points of the internal body assembly can be arranged to follow prescribed trajectories with respect to the external vessel, simple and established forms of Power Take Off systems can be appropriately inserted (linear or rotary, hydraulic or electrical), in order to further convert the internally stored mechanical energy to electrical energy.

An example of this arrangement, its kinematic relations and dynamic equations of motion, are briefly presented in section 2 of this paper. The external vessel is subjected to simultaneous surge and pitch motion in all directions. The inertial reacting body is enclosed internally, suspended appropriately from the external body in such a way that a symmetric four-bar mechanism is formed.

The first advantage of this suspension geometry is that the center of the mass of the suspended body moves in a linear trajectory with respect to the external vessel. This implies the internal body appears to move essentially in linear way, like a simple mass in the conventional form of the PSFrog arrangements. This enables the introduction of a quite simple Power Take Off (PTO) system, as for e.g. hydraulic rams. Moreover, the simplicity and the symmetry of the suspension geometry and of the PTO, ensure a quite simple and robust technological implementation, contrary to all other known above variants of inertial reacting internal bodies.

The second advantage of this design is that the internal body behaves dynamically as a vertically suspended pendulum. However, the suspension geometry, in combination to the optimal mass and the inertia distribution of the internal body, ensure the maximal conversion and storage of the wave energy in the form of kinetic and potential energy. This is reflected to the resulting equivalent pendulum length and inertia of this design, which can far exceed those that can be achieved by an actual technical implementation either of a simple horizontal or of a vertical pendulum (suspended, or inverted). The direct consequence is significant reduction of the suspended mass.

The linearized equations of motion are presented in section 3. Also, the proposed appropriate feedback law and the power that can be converted, is estimated. Finally an indicative design is presented in section 4, as a standalone 1 MW WEC. In section 5, the standout features of this novel design along with the conclusions from the dynamical analysis and the indicative implementation are summarized.

2 Equations of motion

2.1 Description of the assembly and basic definitions

The assembly considered, is depicted in Fig. 1, consisting from a floating external vessel V, into which an internal four-bar mechanism $ABDE$ is hoisted. The waves induce to the vessel, a simultaneous surge motion of magnitude u and a pitching motion of an angle θ, with respect to the inertial coordinate system OXY. The origin O is located at the intersection of the level of the sea with the vertical axis of symmetry of the vessel. The center of mass of the vessel G is located at a distance b from the point O below the level of the sea.

The member DE of the internal four-bar mechanism provides a basis onto which a solid body S is placed. The solid body provides a reaction mass to the motion of the external vessel, rotating with an angle φ about the Z axis of the inertial reference frame OXY. The initial (rest) position R of the center of mass of this solid body is located on the axis of symmetry of the vessel V, at distance a, from the origin O. The coordinate reference system RX_bY_b is rigidly attached to the vessel V, following its motion.

- O: origin of the coordinate system OXY - intersection of the level of the sea with the vertical axis of symmetry of the vessel,

- C: center of mass of the body S,

- R: origin of the body axis system RX_bY_b - initial (rest) position of C,

- G: center of mass of the vessel V,
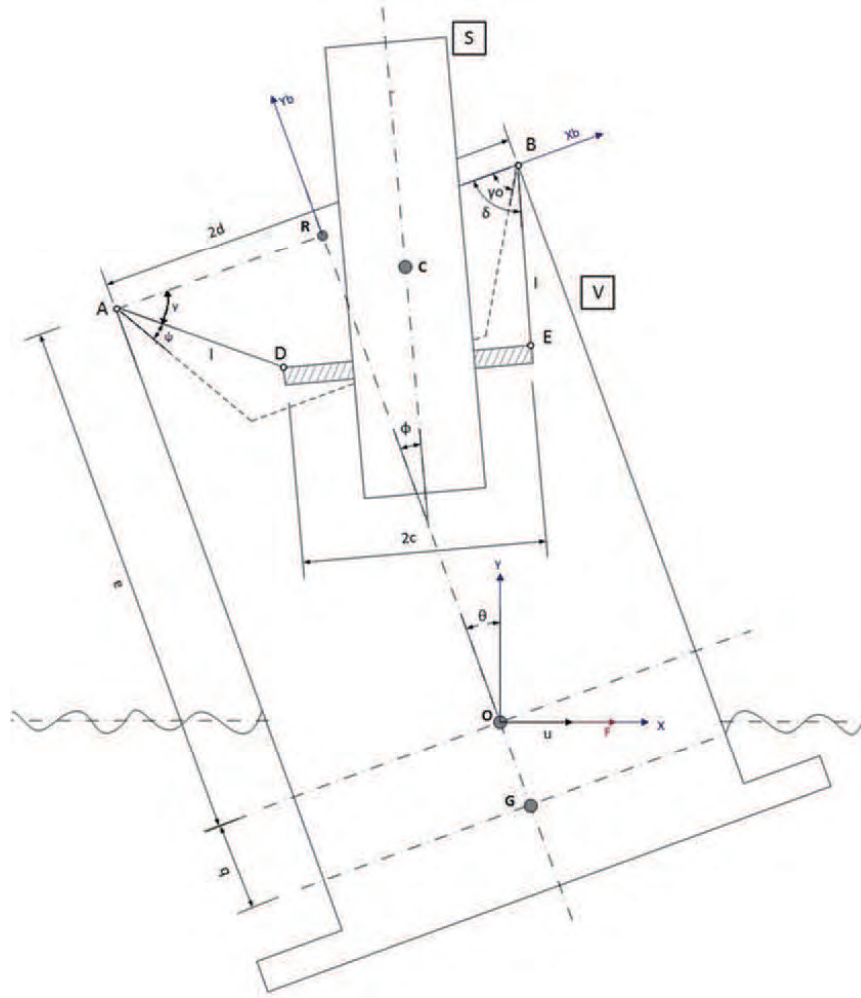
Fig. 1 Schematic presentation of the assembly considered. An internally reacting body S is suspended by an appropriate mechanism by an external floating vessel V.

- a: distance between R and O,

- b: distance between G and O,

- φ: rotating angle of the body S about the Z axis,

- θ: pitching motion induced by the waves,

- u: surge motion induced by the waves.

2.2 Kinematic analysis

2.2.1 Geometric parameters

The basic geometrical configuration of the mechanism is defined by the selection of the three independent lengths d, c, h. The rest of the geometric parameters can be retrieved as follows:

$$l = \sqrt{(d-c)^2 + h^2} \ \ [m] \tag{1}$$

$$\tan(\gamma_0) = \frac{h}{(d-c)} \tag{2}$$
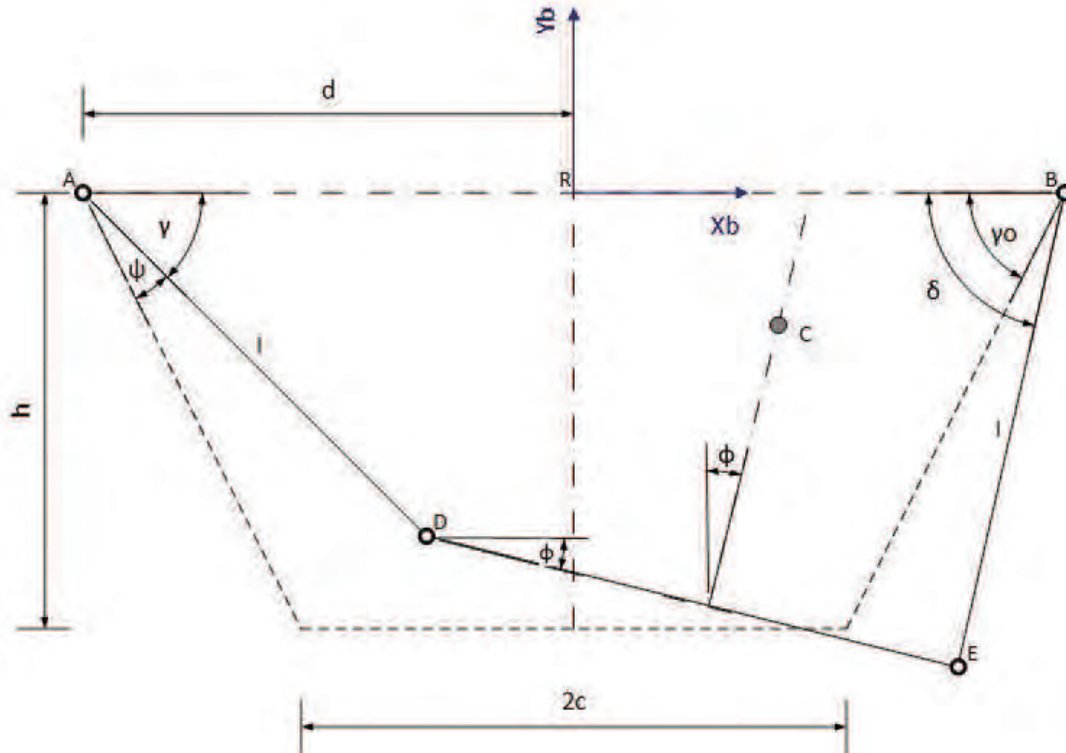
Fig. 2 Geometric parameters and kinematic variables of the mechanism.

2.2.2 Reference position of the mechanism

The reference (rest) position of the mechanism, indicated by dashed lines, is defined by the following relations:

$$\varphi = \psi = 0 \ [rad], \qquad \gamma = \delta = \gamma_0 \ [rad] \tag{3}$$

The origin R of the coordinate system RX_bY_b is selected in the middle of the stationary link (ground) AB of the mechanism, with the position of the axes indicated as in the figure.

The kinematics of the mechanism can be fully retrieved as a function of a single degree of freedom, the angle φ. he rest of the angles can be retrieved by the following compatibility relations of the closed kinematic chain:

$$l \cos \gamma + 2c \cos \varphi + l \cos \delta = 2d \ [m] \tag{4a}$$

$$l \sin \gamma + 2c \sin \varphi - l \sin \delta = 0 \ [m] \tag{4b}$$

After reforming and squaring each of the above equations and finally adding them, using the abbreviations

$$x_\varphi = d - c \cos \varphi \ [m] \tag{5a}$$

$$y_\varphi = c \sin \varphi \ [m] \tag{5b}$$

$$r_\varphi = x_\varphi^2 + y_\varphi^2 \ [m^2] \tag{5c}$$

leads to

$$-x_\varphi l \cos \gamma + y_\varphi l \sin \gamma + r_\varphi = 0 \tag{6}$$

This equation can be further recast to a second order polynomial equation

$$a_{2\varphi} z_\gamma^2 + 2a_{1\varphi} z_\gamma + a_{0\varphi} = 0 \tag{7a}$$

where

$$Z_\gamma = \tan\left(\frac{\gamma}{2}\right) \tag{7b}$$

$$a_{2\varphi} = r_\varphi + x_\varphi l \ [m^2] \tag{7c}$$

$$a_{1\varphi} = y_\varphi l \ [m^2] \tag{7d}$$

$$a_{0\varphi} = r_\varphi - x_\varphi l \ [m^2] \tag{7e}$$

$$\Delta = \sqrt{a_{1\varphi}^2 - a_{2\varphi}a_{0\varphi}} \ [m^2] \tag{7f}$$

Finally, γ, ψ and δ, can be expressed as functions of angle φ as follows:

$$\gamma = 2\tan^{-1}\left(\frac{-\alpha_{1\varphi} + \Delta}{\alpha_{2\varphi}}\right) \ [rad] \tag{8}$$

$$\psi = \gamma_0 - \gamma \ [rad] \tag{9}$$

$$\delta = \sin^{-1}\left(\sin\gamma + \frac{2c}{l}\sin\varphi\right) \ [rad] \tag{10}$$

2.2.3   Angular velocities

The time derivatives of the compatibility relations of the closed kinematic chain, lead to the following equations:

$$\dot{\gamma} = -\frac{2c}{l\sigma}\dot{\varphi} = -\mu\dot{\varphi} \ \left[\frac{rad}{s}\right] \tag{11}$$

$$\dot{\psi} = -\dot{\gamma} = \mu\dot{\varphi} \ \left[\frac{rad}{s}\right] \tag{12}$$

where the non-dimensional abbreviations:

$$\mu = \frac{2c}{l\sigma} \tag{13}$$

$$\sigma = \frac{\sin(\gamma + \delta)}{\sin(\varphi + \delta)} \tag{14}$$

2.2.4   Motion of the center of mass

The original position of the center of mass C of a body attached to the mechanism is assumed to coincide with the origin R of the coordinate system Rx_by_b at the rest position of the mechanism. Therefore, its coordinates x_b, y_b with respect to this system at an arbitrary position of the mechanism can be derived as follows:

$$x_b = -d + l\cos\gamma + c\cos\varphi + h\sin\varphi \ [m] \tag{15}$$

$$y_b = l\sin\gamma + c\sin\varphi - h\cos\varphi \ [m] \tag{16}$$

$$h = l\sin\gamma_0 \ [m] \tag{17}$$

It is easy to derive that y_b is equal to zero when $l = 2d = 4c$, as it is the special case of the Roberts linkage. Therefore, the point C moves in a straight line over the segment AB. The velocities of C can be derived as follows:

$$\dot{x}_b = r_x\dot{\varphi} \ \left[\frac{m}{s}\right] \tag{18}$$

$$\dot{y}_b = r_y\dot{\varphi} \ \left[\frac{m}{s}\right] \tag{19}$$

where

$$r_x = l\mu\sin\gamma - c\sin\varphi + h\cos\varphi \ [m] \tag{20}$$

$$r_y = -l\mu\cos\gamma + c\cos\varphi + h\sin\varphi \ [m] \tag{21}$$

The displacement and velocity of the point G with respect to the inertial coordinate system are as follows:

$$x_G = u + b\sin\theta \ [m] \tag{22a}$$

$$y_G = -b\cos\theta \ [m] \tag{22b}$$

$$\dot{x}_G = \dot{u} + \dot{\theta}(b\cos\theta) \ [\frac{m}{s}] \tag{23a}$$

$$\dot{y}_G = \dot{\theta}(b\sin\theta) \ [\frac{m}{s}] \tag{23b}$$

The translation of the reaction mass according to the system OXY is as follows:

$$\begin{aligned} x_m &= x_R + x_b\cos\theta - y_b\sin\theta \\ &= u + x_b\cos\theta - (a + y_b)\sin\theta \ [m] \end{aligned} \tag{24a}$$

$$\begin{aligned} y_M &= y_R + x_b\sin\theta + y_b\cos\theta \\ &= x_b\sin\theta + (a + y_b)\cos\theta \ [m] \end{aligned} \tag{24b}$$

where

$$x_R = u - a\sin\theta \ [m] \tag{25a}$$

$$y_R = a\cos\theta \ [m] \tag{25b}$$

The corresponding expressions for x_b, y_b are given in Eq. (15) and (16), where the kinematic analysis of the motion of the center of mass C of the body S with respect to the frame RX_bY_b is performed.

The expression of the corresponding velocities $\dot{x}_M$ and $\dot{y}_M$ result as follows:

$$\dot{x}_M = \dot{u} - l_{xM}\dot{\theta} + r_{xM}\dot{\varphi} \ [\frac{m}{s}] \tag{26}$$

$$\dot{y}_M = l_{yM}\dot{\theta} + r_{yM}\dot{\varphi} \ [\frac{m}{s}] \tag{27}$$

where

$$l_{xM} = (a + y_b)\cos\theta + x_b\sin\theta \ [m] \tag{28a}$$

$$l_{yM} = x_b\cos\theta - (a + y_b)\sin\theta \ [m] \tag{28b}$$

$$r_{xM} = r_x\cos\theta - r_y\sin\theta \ [m] \tag{29a}$$

$$r_{yM} = r_x\sin\theta + r_y\cos\theta \ [m] \tag{29b}$$

and the expressions for $\dot{x}_b$, $\dot{y}_b$ bare given in Eq (18) and (19).

2.3 Differential equations of motion

The kinetic energy captured from the bodies can be written as:

$$T = \frac{1}{2}m_V(\dot{x}_G^2 + \dot{y}_G^2) + \frac{1}{2}I_V\dot{\theta}^2 + \frac{1}{2}m_s(\dot{x}_M^2 + \dot{y}_M^2) + \frac{1}{2}I_s(\dot{\theta} - \dot{\varphi})^2 \ [\frac{kg\ m^2}{s^2} = J] \tag{30}$$

where:

- m_V: the mass of the vessel V including the added mass of the water,

- m_s: the mass of the body S,

- I_V: the axial mass moment of inertia of the vessel about axis through point O, perpendicular to OXY plane,

- I_s: the axial mass moment of inertia of the reaction mass about axis through point C, perpendicular to plane OXY.

The potential energy is as follows:

$$U = m_s g y_M + \frac{1}{2} K_V \theta^2 + m_V g y_G \ [\frac{kg \ m^2}{s^2} = J] \tag{31}$$

where K_V is the hydrostatic stiffness [13], in pitch (and/or roll) for the vessel about O, that can be calculated in the form of:

$$K_V = \rho \cdot g \int_{A_w} (x - x_{buoy})^2 dS \ [\frac{kg \ m^2}{s^2}] \tag{32}$$

where A_W is the water plane area and x_{buoy} the position of the center of buoyancy.

The system presents three degrees of freedom:

$$r_1 = u \ [m] \tag{33a}$$

$$r_2 = \theta \ [rad] \tag{33b}$$

$$r_3 = \varphi \ [rad] \tag{33c}$$

$$\mathbf{r}^T = [u \quad \theta \quad \varphi] \tag{34}$$

The equations of motion of the system can be derived by the application of the following Lagrange principle:

$$\frac{d}{dt}(\frac{\partial L}{\partial \dot{r_i}}) - (\frac{\partial L}{\partial r_i}) = F_i, \qquad i = 1, 3 \tag{35}$$

where

$$L = T - U \tag{36}$$

and F_i denotes the external and the damping forces of the system. The equations of motion result as:

$$\frac{d}{dt} P_u + R_u \dot{u} = F_w \ [N = \frac{kg \ m}{s^2}] \tag{37}$$

$$\frac{d}{dt} P_\theta + K_v \theta + T_{v\theta} + T_{g\theta} = 0 \ [Nm] \tag{38}$$

$$\frac{d}{dt} P_\varphi + T_{g\varphi} = T_p \ [Nm] \tag{39}$$

where the generalized momentum values P_u, P_θ, P_φ are defined as follows:

$$P_u = \frac{\partial L}{\partial \dot{u}} = M_{uu} \dot{u} + M_{u\theta} \dot{\theta} + M_{u\varphi} \dot{\varphi} \ [kg \frac{m}{s}] \tag{40a}$$

$$P_\theta = \frac{\partial L}{\partial \dot{\theta}} = M_{u\theta} \dot{u} + M_{\theta\theta} \dot{\theta} + M_{\theta\varphi} \dot{\varphi} \ [kg \frac{m^2}{s}] \tag{40b}$$

$$P_\varphi = \frac{\partial L}{\partial \dot{\varphi}} = M_{u\varphi} \dot{u} + M_{\theta\varphi} \dot{\theta} + M_{\varphi\varphi} \dot{\varphi} \ [kg \frac{m^2}{s}] \tag{40c}$$

with:

$$M_{uu} = m_v + m_s \ [kg] \tag{41a}$$

$$M_{u\theta} = m_v b \cos\theta - m_s l_{xM} \ [kg \cdot m] \tag{41b}$$

$$M_{u\varphi} = m_s r_{xM} \ [kg \cdot m] \tag{41c}$$

$$M_{\theta\theta} = I_v + I_s + m_v b^2 + m_s(l_{xM}^2 + l_{yM}^2) \ [kg \cdot m^2] \tag{41d}$$

$$M_{\theta\varphi} = -[I_s + m_s(r_{xM} l_{xM} - r_{yM} l_{yM})] \ [kg \cdot m^2] \tag{41e}$$

$$M_{\varphi\varphi} = I_s + m_s(r_{xM}^2 + r_{yM}^2) \ [kg \cdot m^2] \tag{41f}$$

The moments due to the gravity are:

$$T_{v\theta} = m_v g b \sin\theta \ [Nm] \tag{42a}$$

$$T_{g\theta} = m_s g l_{ym} \ [Nm] \tag{42b}$$

$$T_{g\varphi} = m_s g r_{ym} \ [Nm] \tag{42c}$$

The rest of the terms are:

- R_u: an added damping coefficient for the surge motion induced by the waves,

- F_w: the force due to the incident and diffracted waves,

- T_p: the reaction moment of the PTO mechanism.

2.4 State space representation

A compact state space representation for the system of equations is possible under the following compact form:

$$\dot{\mathbf{z}}_1 = \mathbf{M}^{-1}\mathbf{z}_2 \tag{43a}$$

$$\dot{\mathbf{z}}_2 = \mathbf{f}_R \tag{43b}$$

where:

$$\mathbf{z}_1^{\mathbf{T}} = \mathbf{r}^{\mathbf{T}} = [u \quad \theta \quad \varphi] \tag{44a}$$

$$\mathbf{z}_2^{\mathbf{T}} = [P_u \quad P_\theta \quad P_\varphi] \tag{44b}$$

$$\mathbf{f}_R = \begin{bmatrix} F_w - R_u \dot{u} \\ -K_{v\theta} - T_{v\theta} - T_{g\theta} \\ -T_{g\varphi} + T_p \end{bmatrix} \tag{45}$$

$$\mathbf{M} = \begin{bmatrix} M_{uu} & M_{u\theta} & M_{u\varphi} \\ M_{u\theta} & M_{\theta\theta} & M_{\theta\varphi} \\ M_{u\varphi} & M_{\theta\varphi} & M_{\varphi\varphi} \end{bmatrix} \tag{46}$$

2.5 Equation of motion of the internal inertial reacting body

Under the assumption that the surge and pitch motion of the external vessel are known in the time domain, the equations of motion can be further simplified, retaining only the set of equations which refer to the mechanism itself:

$$\frac{d}{dt}(M_{\varphi\varphi}\dot{\varphi}) = -\frac{d}{dt}(M_{u\varphi}\dot{u} + M_{\theta\varphi}\dot{\theta}) - T_{g\varphi} + T_p \ [Nm] \tag{47}$$

In an equivalent state space representation:

$$\mathbf{z} = \begin{bmatrix} \varphi \\ P_\varphi \end{bmatrix} \tag{48}$$

$$\begin{bmatrix} \dot{\varphi} \\ \dot{P}_\varphi \end{bmatrix} = \begin{bmatrix} (P_\varphi - M_{u\varphi}\dot{u} - M_{\varphi\varphi}\dot{\varphi})/M_{\varphi\varphi} \\ -T_{g\varphi} + T_p \end{bmatrix} \tag{49}$$

3 Maximum Power Conversion Capability

3.1   Linearization of the equations of motion

Under the assumption of small perturbations around the rest position of the mechanism, the following approximate relations hold for the angles $\alpha \in \{\varphi, \psi, \theta\}$ of the assembly:

$$\cos \alpha \approx 1 \tag{50a}$$

$$\sin \alpha \approx \alpha \tag{50b}$$

which results to:

$$\cos \gamma = \cos(\gamma_0 - \psi) \approx \cos \gamma_0 + \psi \sin \gamma_0 \tag{51a}$$

$$\sin \gamma = \sin(\gamma_0 - \psi) \approx \sin \gamma_0 - \psi \cos \gamma_0 \tag{51b}$$

   The equations of motion (15) and (16) of the of the center of mass C of the oscillating body with respect to the origin R of the coordinate system RX_bY_b can thus be simplified as follows:

$$x_b \approx l_p \varphi \ \ [m] \tag{52a}$$

$$y_b \approx 0 \ \ [m] \tag{52b}$$

$$l_p = (\mu + 1)h \ \ [m] \tag{53}$$

$$\mu \approx \mu_0 = \frac{2c}{l\sigma_0} = \frac{c}{l \cos \gamma_0} = \frac{1}{d/c - 1} \tag{54}$$

$$\sigma \approx \sigma_0 = \frac{\sin 2\gamma_0}{\sin \gamma_0} = 2 \cos \gamma_0 \tag{55}$$

   Equations (52a) and (52b) imply that the physical motion of the center of the mass of the body is linear, exactly in the same way as the traditional designs of linear sliding mass WECs, as for e.g. in the form of PS Frog.

   Similar simplified relations hold for the factors r_x, r_y, l_{xM}, l_{yM}, r_{xM} and r_{yM}:

$$r_x \approx l_p \ \ [m] \tag{56a}$$

$$r_y \approx 0 \ \ [m] \tag{56b}$$

$$l_{xM} \approx a \ \ [m] \tag{57a}$$

$$l_{yM} \approx l_p \varphi \ \ [m] \tag{57b}$$

$$r_{xM} \approx l_p \ \ [m] \tag{58a}$$

$$r_{yM} \approx l_p \theta \ \ [m] \tag{58b}$$

as well as for the components of the matrix $\mathbf{M}$:

$$\mathbf{M} = \begin{bmatrix} m_v & m_v b & m_s l_p \\ m_v b & I_v + I_s + m_v b^2 & -I_\theta \\ m_s l_p & -I_\theta & I_\varphi \end{bmatrix} \tag{59}$$

where:

$$I_\theta = I_s + m_s l_p a \ \ [kg \cdot m^2] \tag{60}$$

$$I_\varphi = I_s + m_s l_p \ \ [kg \cdot m^2] \tag{61}$$

and the moments due to the gravity:

$$T_{v\theta} \approx 0 \ \ [Nm] \tag{62a}$$

$$T_{g\theta} \approx m_s g l_p \varphi \ \ [Nm] \tag{62b}$$

$$T_{g\varphi} \approx m_s g l_p \theta \ \ [Nm] \tag{62c}$$

3.2   Proposed form for the Power Take Off Moment and Feedback Law

In view of the non-linear equation of motion (47), the mechanism is inherent to an unstable behavior. For this reason, a feedback law is incorporated in the power take off moment, being of the following form:

$$T_p = -K_p \varphi - R_p \dot{\varphi} + T_N \ [Nm] \tag{63}$$

where K_p and R_p are constant linear feedback gains to be properly selected and T_N denotes an appropriate compensator for the non-linearity of the system in the form:

$$T_N = \frac{d}{dt}(P_\varphi - m_s l_p \dot{u} + I_\theta \dot{\theta} - I_\varphi \dot{\varphi}) + (T_{g\varphi} - m_s g l_p \theta) \ [Nm] \tag{64}$$

which results to the following equation for motion of the internal body:

$$I_\varphi \ddot{\varphi} + R_p \dot{\varphi} + K_p \varphi = -m_s l_p \ddot{u} + I_\theta \ddot{\theta} - m_s g l_p \theta + T_N \ [Nm] \tag{65}$$

Obviously T_N is equal to zero for a linearized system. It should be noted, that the linearized system in equation (65) is statically and dynamically stable, under the proper selection of the parameters R_p, K_p. Therefore, although the initial non-linear dynamic system may present static or dynamic instabilities. The final linearized system is always stable, as a result of the feedback law in equations (63) and (64).

3.3   Analysis of the expected dynamic behavior

Equation (65) implies that the motion of the internal body is fully equivalent dynamically to that of a damped physical pendulum, with a mass m_s and inertia I_s about its *CM*, which is suspended at a distance l_p from its center of mass.

However, it should be stretched, that in view of equation (53), the equivalent length l_p of this pendulum can be many orders of magnitude higher than that expected by any other vertical pendulum, realized in the traditional natural technological way, as for e.g. in the form of SEAREV.

This pendulum can simultaneously convert three different forms of wave energy:

- The kinetic energy resulting from the surge motion.

- The kinetic energy resulting from the pitching motion.

- The potential energy resulting from the pitching motion.

In view of equation (63), the selection of the feedback gains can be performed in a way to ensure stability of the system, optimal tuning of the natural periods of the system to the periods of the external source, as well as maximum power conversion capability.

3.4   Calculation of maximum power conversion capacity

The analysis of the power conversion capability can be performed independently for the surge and pitch motion of the converter. However, the design of the external vessel and the coupled form of equations [14] imply that dependence exists in fact between them. Detailed analysis of such dependence is performed in [15]. Following the outline of such an analysis, the vessel will be assumed to be subjected to a pitching motion of amplitude Θ_C and frequency ω.

$$\theta(t) = \Theta_C \cos \omega t \ [rad] \tag{66}$$

while the surge motion will depend on the pitch motion as follows:

$$u(t) = -b\theta(t) = -b\Theta_C \cos \omega t \ [m] \tag{67}$$

As a result, the equation of motion (65) now becomes:

$$I_\varphi \ddot{\varphi} + R_p \dot{\varphi} + K_p \varphi = -M_e \Theta_C \cos \omega t \tag{68}$$

$$T_p = -K_p \varphi - R_p \dot{\varphi} \quad [Nm] \tag{69}$$

$$M_e = \omega^2 I_p + m_s g l_p \quad [kg \cdot (\frac{m}{s})^2] \tag{70}$$

$$I_P = I_S + m_s l_p (a+b) \quad [kg \cdot m^2] \tag{71}$$

The steady state response of the system is a harmonic function with a frequency equal to ω and with a phase difference of $\pi/2$ with the excitation force, in order to maximize power capture from the excitation force:

$$\varphi(t) = -\Phi_S \sin \omega t \quad [rad] \tag{72}$$

The minus sign is used to denote that for the positive θ angle, a negative φ angle should result, in order to ensure the stability of the vessel.

Substitution of equations (61) and (70) into equation (68) leads to the following results:

$$R_p = \frac{M_e \Theta_C}{\omega \Phi_S} \quad [\frac{kg \cdot m^2}{s}] \tag{73}$$

$$K_p = \omega^2 I_\varphi \quad [kg \cdot (\frac{m}{s})^2] \tag{74}$$

The mean power absorbed by the PTO mechanism is defined as follows:

$$P_{out} = \frac{1}{T_w} \int_0^{T_w} T_p \dot{\varphi} dt \quad [W] \tag{75}$$

where the wave period is

$$T_w = \frac{2\pi}{\omega} \quad [s] \tag{76}$$

Substitution of equations (69), (76) into (75) leads to the following expression

$$P_{out} = -\frac{1}{2} \omega M_e \Theta_c \Phi_s = -P_{in} \quad [W] \tag{77}$$

or alternatively to:

$$P_{out} = -\frac{1}{2} \omega \Theta_c m_s X_M a_e \quad [W] \tag{78}$$

where:

$$X_M = l_p \Phi_s \quad [m] \tag{79a}$$

$$a_e = g + \omega^2 (a+b+l_I) \quad [\frac{m}{s^2}] \tag{79b}$$

$$l_I = \frac{I_S}{m_s l_p} \quad [m] \tag{79c}$$

and

- ω: frequency of the waves,

- Θ_c: amplitude of the pitch motion,

- m_s: reaction mass,

- X_M: amplitude of the linear motion of the center of mass of the oscillating body,

- Φ_s: maximum inclination of the mechanism,

- l_P: equivalent pendulum length,

- I_S: inertia of the oscillating body about its *CM*.
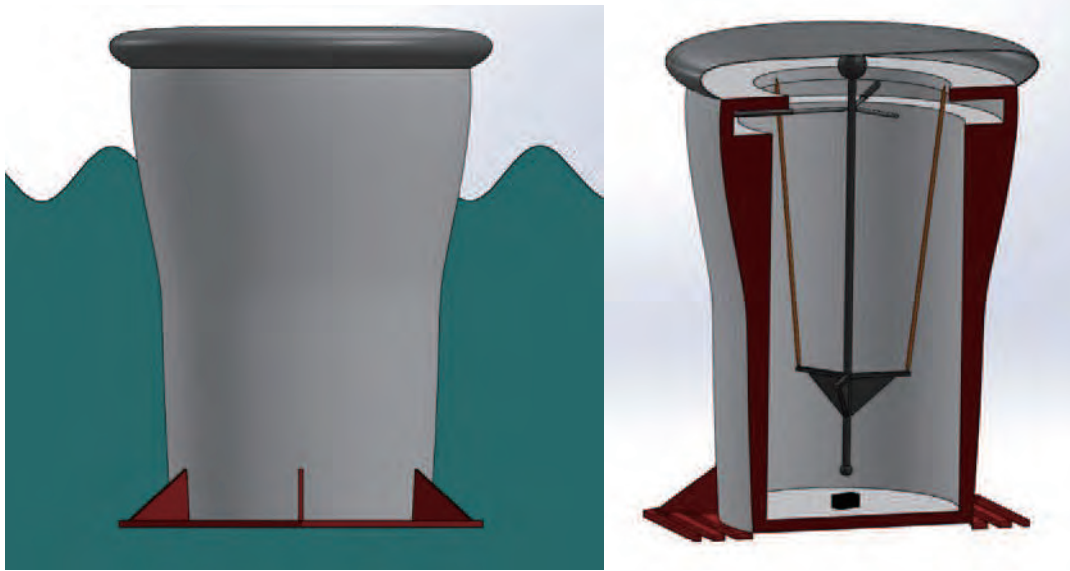
Fig. 3 A fully enclosed multi axis combined surge and pitch WEC.
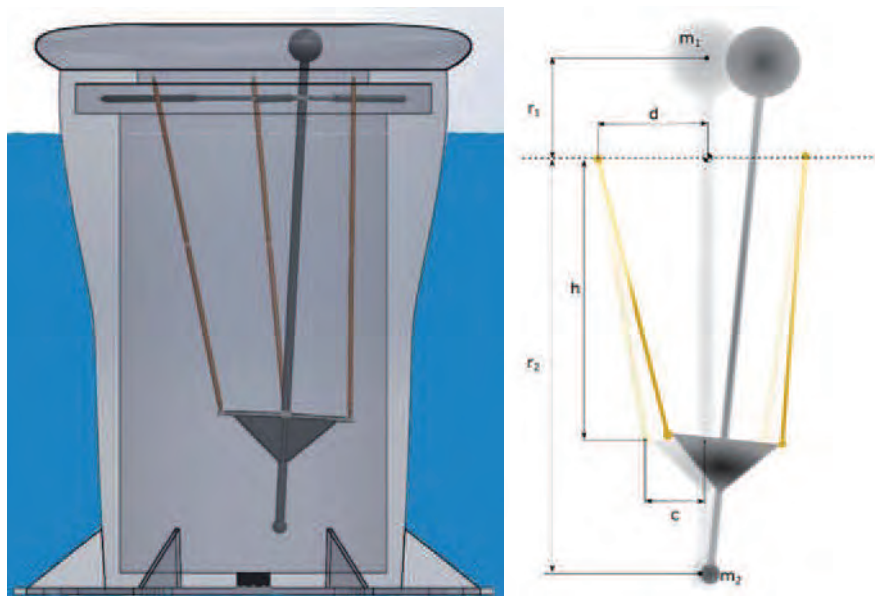
Fig. 4 Rest and limit position of the inertial mass along with the basic parameters of the suspension geometry.

4 Indicative Implementations - A standalone 1MW rated power WEC

The wave energy level is expressed as power per unit length along the wave crest or along the shoreline direction. Typical values for "good" offshore locations range between 20 and 70 kW/m as annual average and occur mostly in moderate to high latitudes, as for e.g. in the North Sea. A design approach for a peak energy level of 40 kW/m (also considering good locations in the Mediterranean Sea) can be reasonably used as a target value to be reached by the subsequent WECs to be designed.

The actual power that can be absorbed by a pitching and surging WEC is expressed by the value of the Capture Width, which is around $L = \lambda/\pi$, for pitching and surging WECs [7]. A typical value for the wavelength of $\lambda \approx 50 \div 100$ m is assumed. Calculating L and multiplying this value with the wave power per unit length,
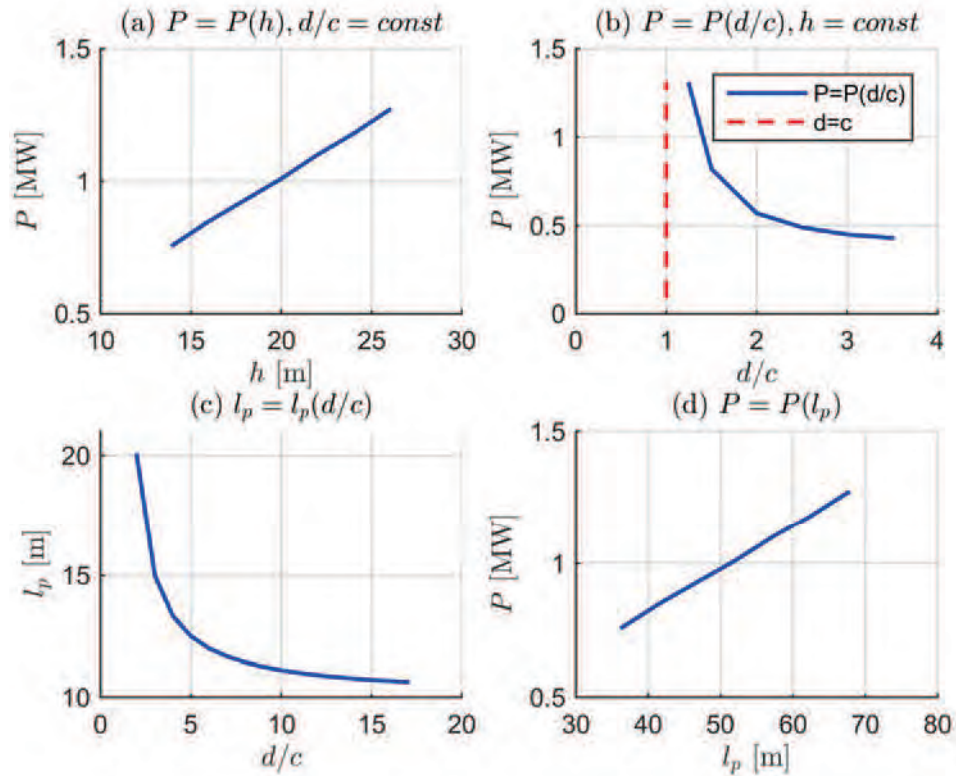
Fig. 5 (a) Output power for varying values of h. (b) Output power for varying values of the ratio d/c. (c) Equivalent pendulum length l_p for varying values of the ratio d/c. (d) Output power for varying values of l_p.

results to a total value of a power around 0.6-1.3 MW [13], which can be absorbed by a unique WEC.

Moreover, assuming the buoy to be of a hemispherical shape, estimates for the optimum radius of the buoy $R = 0.262T_w^2$ can be derived [8], although this value has been proved for heaving motion only. Taking into account wave periods of $6 \div 10$ seconds, this leads to buoy with a radius of at least $10 \div 26$ m, able to capture the amount of power calculated previously. The above estimates are in line with the results found in corresponding sources [24].

Therefore, an indicative mechanism for a standalone 1MW WEC is presented. A body consisting of two unequal spheres and a beam that links them together will be used as an inertial mass. This body is suspended with three links inside a sealed vessel. All the other additional components such as the hydraulic system and the rams are also enclosed in the vessel. This basic configuration has the form presented in Figures 3 and 5. It should be noted, that hydraulic power take of systems can offer a reliable and efficient approach for wave energy conversion [25].

As figure 3 indicates, the vessel is a fully sealed hull with a plate at the bottom for maximizing reaction, increasing the added mass and lowering the center of mass of the external vessel. The hydraulic system power pack can be placed at the bottom, while the rams operate in the same plane with the center of mass of the oscillating body.

The detailed design of the hull is beyond the scope of this paper, since emphasis is placed on the design of the mechanism itself. However, efficient procedures for its optimal design can be applied [26, 27].

Examination of equation (77) of the output power, for different values of the four-bar mechanism's lengths h, d, c, as noted on figure 2 and also the masses and distances between the two spheres of the "pendulum", has led to the following graphs shown on figure 4.

For this task, a preliminary set of geometrical restrictions has been set, by examining the configuration of the system:

- $d > c$

- $h < r_2$

- $h > c$

- $d > r_2 \sin \Phi_s$

The first sphere, made of iron, has a radius of $R_1 = 1.22$ m, while the second $R_2 = 0.77$ m. The centers of those two components have a distance of 37.5 m. Assuming that the weight of the beam and the supporting brackets are evenly distributed along the total length, the values of $m_1 = 60$ tn, $r_1 = 7.5$ m and $m_2 = 15$ tn and $r_2 = 30$ m are reached, where m_1, m_2 and r_1, r_2 are defined in figure 4.

- m_s: total mass of body S,

- m_1: mass of 1st sphere,

- m_2: mass of 2nd sphere,

- r_1: distance of m_1 from C,

- r_2: distance of m_2 from C.

Considering that $m_s = m_1 + m_2$ and $m_1/m_2 = r_2/r_1$, the moment of inertia of the body S:

$$I_{S_C} = m_s r_1 r_2 \ [kg \cdot m^2] \tag{80}$$

and

$$I_S \equiv I_{S_O} = m_s (r_1 r_2 + a^2) \ [kg \cdot m^2] \tag{81}$$

The linear correlation between the output power and the equivalent pendulum length l_p is obvious in equation (77), same with the total mass m_s. The length l_p on Eq.(53) depends solely on the choice of the lengths h (linear), d, c as shown on figure 5.

Figure 5b, shows that as the ratio d/c moves closer to the value 1 ($d = c$), output power is ascending. Of course, this ratio is restricted by the geometry of the mechanism and the system as a whole.

In general, the geometric parameters of the vessel and consequently the suspended body's and the suspension geometry's, should be selected primarily based on the depth of the water that this WEC will be installed as this is a basic restriction.

It should be clarified, that the values of Table 1, refer just to an indicative implementation of a mechanism for a WEC and they are by no means optimized. Such an approach is obviously necessary in full association to the design of an optimized external vessel.

The combined values of power and suspended mass in Table 1 compare more than favorably to those necessary for other types of internally reacting WECs, such as PSFrog [14] or SEAREV [13, 27] or other technologies [28]. Far more important, the suspension geometry and the simplicity of the PTO, render this design far more reliable and easily implementable than all other known types of internally reacting masses.

Next, considering the non-linear form of the system, are presented the most important simulations.

Figure 9 shows how various geometric parameters of the system, respond as functions of angle ϕ. It is worth noting the observation that for small perturbations of the angle ϕ, parameters like μ, σ, r_x, r_y and the angles ψ, γ and δ, remain approximately constant which showcases the validity of the assumption of small perturbations during the linearization of the model.
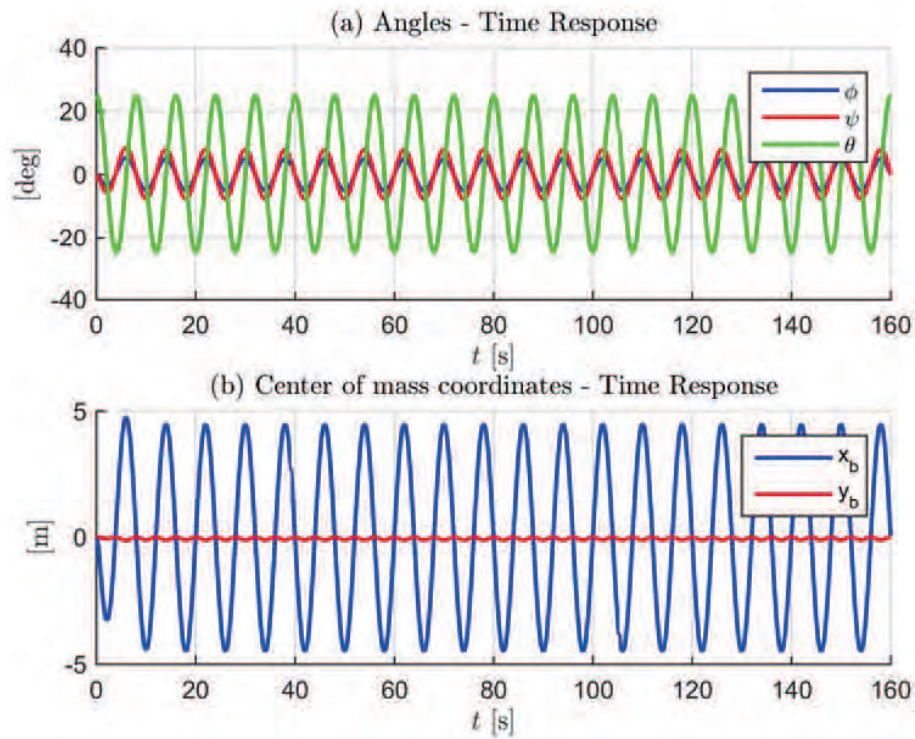
Fig. 6 (a) Response of the angles φ, θ, ψ for harmonic excitation of the system (b) Movement of the body's center of mass C, according to the $Rx_b y_b$ coordinate system during the excitation.
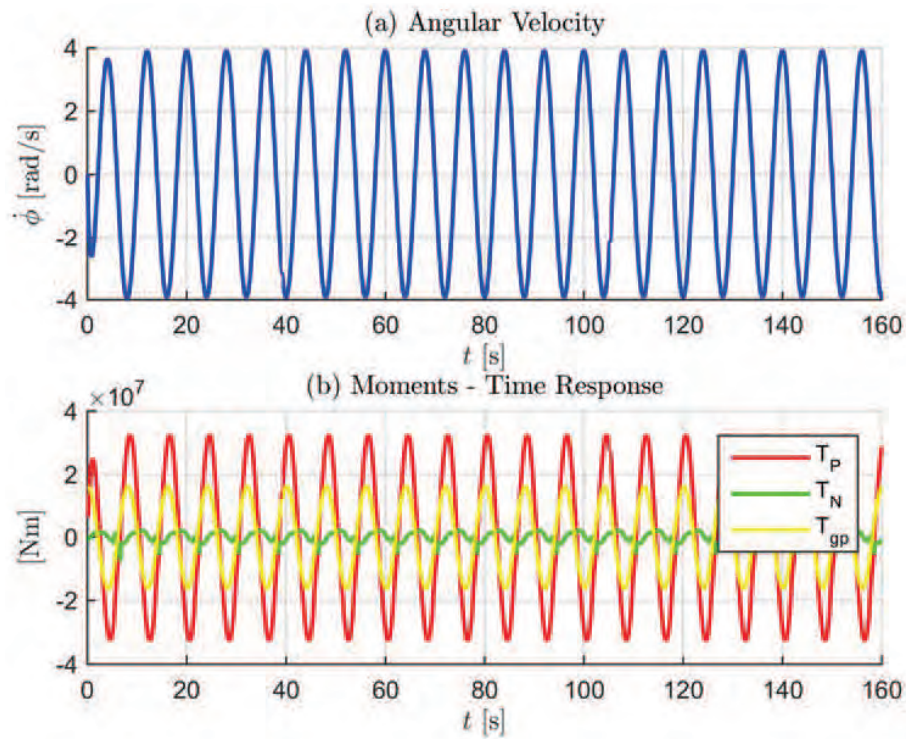
Fig. 7 (a) Response of the angular velocity $\dot{\varphi}$ (b) Response of the output forces of the system.
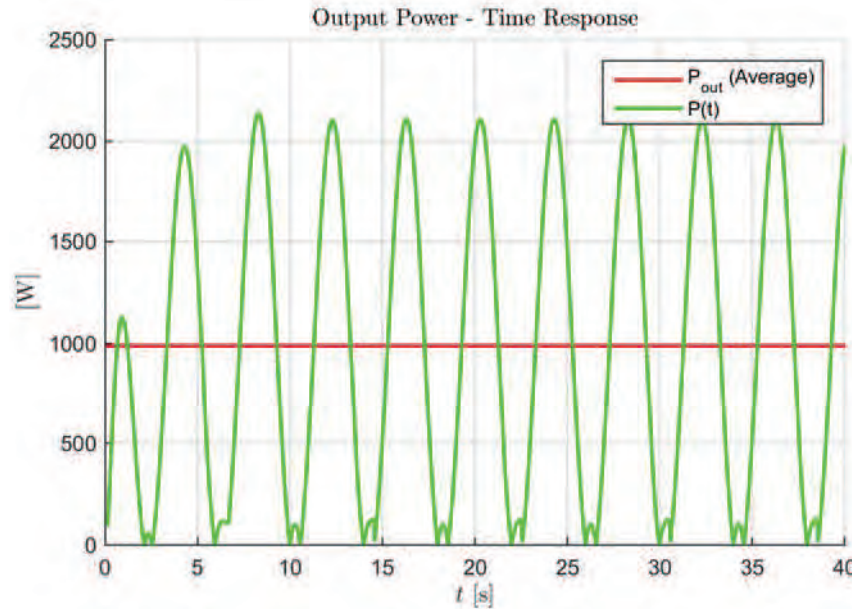
Fig. 8 Time response of the output power of the system and mean output power.
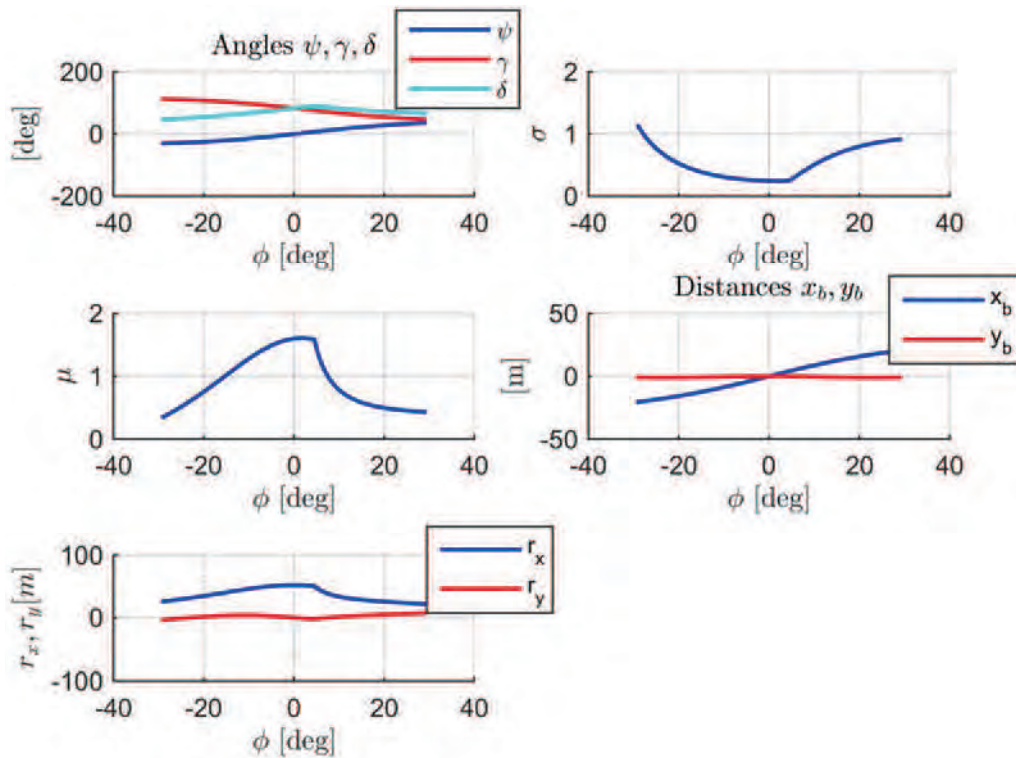
Fig. 9 (a) Angles ψ, γ and δ as a function of angle φ. (b) Dimensionless parameter σ as a function of angle φ. (c) Dimensionless parameter μ as a function of angle φ. (d) Coordinates of the body's S center of mass C, as a function of angle φ. (e) Parameters r_x and r_y, which express the relation between the velocities of point C and angular velocity $\dot{\varphi}$, as a function of angle φ.

Table 1 Input data for numerical simulations of periodic motions ($\delta = 0.5, \alpha = -10.0, \beta = 10.0, Q_0 = 10.0$)

Four-bar mechanism						
h [m]	d [m]	c [m]	γ_0 [°]	l [m]	μ	l_p [m]
20.00	6.50	4.00	82.87	20.16	1.60	52.00
Body & Vessel						
m_1 [tn]	m_2 [tn]	r_1 [m]	r_2 [m]	a [m]	b [m]	
60.00	15.00	7.50	30,00	5,00	2,50	
m_s [kg]	I_s [kg·m^2]	I_p [kg·m^2]	I_ϕ [kg·m^2]	D_V [m]		
7.50E+04	1.88E+07	4.80E+07	2.22E+08	33.54		
Response Parameters						
Θ_c [°]	Φ_s [°]	T_w [s]	ω [rad/s]	M_e [kg·m^2/s^2]	X_M [m]	
25,00	5,00	8.00	0.79	6.79E+07	4.54	
PTO						
R_p			K_p		P_{out}[MW]	
4.32E+08			1.37E+08		1.01	

Where T_w is the wave period and D_V the vessel's outer diameter.

5 Conclusions

The novel class of Wave Energy Converters, consisting from fully enclosed inertially reacting bodies under appropriate suspension geometry from an external floating vessel can provide a reliable design, able to meet the severe conditions for survivability under extreme weather conditions.

As it results, the linear motion of the center of mass of the suspended body enables the introduction of a quite simple form of a PTO design. Moreover, the simplicity and the symmetry of the suspension geometry and of the PTO mechanism, ensure a quite simple and robust technological implementation.

Moreover, the optimal dynamic design of the geometry, the mass and the inertia distribution of the internal body ensure the maximal conversion and storage of the wave energy. This results to a significant reduction of the suspended mass, compared to other internal reacting designs.

The concept is flexible and parametrically designed, enabling its implementation in any form of floating vessels. A first option is as standalone WEC, fully enclosed in appropriately designed hulls. Moreover, an alternative direction for their implementation consists in properly embedding them in floating offshore platforms, supporting wind turbines. Such a design can drastically enhance the performance, the efficiency and the potential of floating offshore energy applications.

References

[1] Gunn, K. and Stock-Williams, C. (2012), Quantifying the global wave power resource, *Renewable Energy*, **44**, 296-304.
[2] Richardson, D.S. and Aggidis, G.A. (2013), The Economics of Multi-Axis Point Absorber Wave Energy Converters, *Ocean Renewable Energy*, **8**.
[3] Bedard, R. and Hagerman, G. (2005), *Offshore Wave Power Feasibility Demonstration Project: Project Definition Study*, Final Summary Report, EPRI.
[4] Athanasia, A. and Genachte, A.B. (2013), *Deep Water: The next step for offshore wind energy*, URL http://www.ewea.org/fileadmin/files/library/publications/reports/Deep_Water.pdf.
[5] Serri, L., Sempreviva, A., Pontes, T., Murphy, J., Lynch, K., Airoldi, D., Hussey, J., Rudolph C., and Karagali I. (2012), *Resource Data and GIS Tool: For Offshore Renewable Energy Projects in Europe,* URL http://www.orecca.eu/c/document_library/get_file?uuid=757326c6-102f-4dd3-8790-916755694103&groupId=10129.
[6] Drew, B., Plummer, A., and Sahinkaya, M.N. (2009), A review of wave energy converter technology, *Proceedings of the Institution of Mechanical Engineers, Part A: Journal of Power and Energy*, **223** (8), 887-902.

[7] Falcao, A.F. and de O. (2010), Wave energy utilization: A review of the technologies, *Renewable and Sustainable Energy Reviews*, **14**(3), 899-918.

[8] Lynch, K. and Murphy, J. (2012), *Deliverable D3.6: Overview of offshore wind and ocean energy technologies,* URL http://www.marina-platform.info/dissemination.aspx.

[9] Bracewell, R. (1990), *Frog and PS Frog: a study of two reactionless ocean wave energy converters,* Ph.D. thesis, Lancaster University, UK.

[10] McCabe, A., Bradshaw, A., Meadowcroft, J., and Aggidis, G. (2006), Developments in the design of the PSg Frog Mk 5 wave energy converter, *Renewable Energy*, **31**(2), 141-151.

[11] Korde, U.A. (1999), On providing a reaction for efficient wave energy absorption by floating devices, *Applied Ocean Research,* **21**(5), 235-248.

[12] Korde, U.A. (2001), Phase control of floating bodies from an on-board reference, *Applied Ocean Research,* **23**(5), 251-262.

[13] Babarit, A., Clement, A., and Gilloteaux, J. (2005), Optimization and time-domain simulation of the SEAREV wave energy converter, *Proceedings of 24th International Conference Offshore Mechanics Arctic Engineering*, **2**, 703-712, Halkidiki, Greece.

[14] Widden, M.B., French, M.J., and Aggidis, G.A. (2008), Analysis of a pitching-and-surging wave-energy converter that reacts against an internal mass, when operating in regular sinusoidal waves, *Proceedings of the Institution of Mechanical Engineers, Part M: Journal of Engineering for the Maritime Environment*, **222**, 153-161.

[15] W. Ltd. (2015), *The Penguin Wave Energy Converter*, URL http://www.wello.eu/penguin.php.

[16] EERE (2016), *Wave Energy Prize*, URL http://waveenergyprize.org.

[17] Zhang, D., Aggidis, G., Wang, Y., Mccabe, A., and Li, W. (2013), Experimental results from wave tank trials of a multi-axis wave energy converter, *Applied Physics Letters,* **103**(10).

[18] Salcedo, F., Ruiz-Minguela, P., Rodriguez, R., Ricci, P., and Santos, M. (2009), Oceantec: sea trials of a quarter scale prototype, *Proceedings of 8th European Wave Tidal Energy Conference*, 460-5.

[19] Perez, T., Santos-Mujica, M., and Ruiz-Minguela, J.P. (2009), Performance analysis and control design of a gyro-based wave energy converter, *Control Conference (ECC) 2009 European*, 3743-3748.

[20] Kanki, H., Arii, S., Furusawa, T., and Otoyo, T. (2009), Development of advanced wave power generation system by applying gyroscopic moment, *Proceedings of the 8th European Wave and Tidal Energy Conference*.

[21] Waizmann, G. (2011), *The Wave Gyro*, Master thesis, University of Southampton, UK.

[22] Bracco, G., Giorcelli, E., and Mattiazzo, G. (2011), ISWEC: A gyroscopic mechanism for wave power exploitation, *Mechanism and machine theory*, **46**(10), 1411-1424.

[23] Antoniadis, I.A. and Georgoutsos, V. (2015), Wave energy conversion with fully enclosed multi-axis inertial reaction mechanisms, *DSTA2015, 13th International Conference, Dynamical Systems - Theory and Applications*, 7-10/12/2015. Lodz, POLAND.

[24] Babarit, A. (2015), A database of capture width ratio of wave energy converters, *Renewable Energy*, **80**, 610-628.

[25] Gaspar, J.F., Calvrio, M., Kamarlouei, M., and Soares, C.G. (2016), Power take-off concept for wave energy converters based on oil-hydraulic transformer units, *Renewable Energy*, **86**, 1232-1246.

[26] McCabe, A. (2013), Constrained optimization of the shape of a wave energy collector by genetic algorithm, *Renewable Energy*, **51**, 274-284.

[27] Cordonnier, J., Gorintin, F., Cagny, A. D., Clment, A., and Babarit, A. (2015), SEAREV: Case study of the development of a wave energy converter, *Renewable Energy*, **80**, 40-52.

[28] Mekhiche, M. and Edwards, K.A. (2014), Ocean power technologies power buoy: System-level design, development and validation methodology, *Proceedings of the 2nd Marine Energy Technology Symposium, Seattle*, WA, USA.

Discontinuity, Nonlinearity, and Complexity

Multi-parametric Dependence of Deformation Work of Zona Pelucida in Fertilization Process Trough Quasi-static Continual Shell-like ZP Model

Andjelka Hedrih[1†], Katica (Stevanovic) Hedrih[1,2]

[1] Department of Mechanics, Mathematical Institute of Serbian Academy of Sciences and Arts, (MI SANU),
   11 000 Belgrade Serbia, Mathematical institute SANU, 11 000 Belgrade, Serbia
[2] Faculty of Mechanical engineering, University of Nis, 18 000 Nis, Serbia

Abstract

Zona Pelucida (ZP) is highly specialized glycosylated and sulfated polymer gel that surrounds mammalian oocyte, exhibits elastic or viscoelastic properties and change of diameter in different maturation stages. In process of in vitro fertilization, sperm cells affect the external ZP surface and transfer certain amount of energy to the ZP structure that goes through the deformation work. ZP thickness and number of motile sperm cells are important factors that may influence the fertility. Using the quasi-static approximate ZP model in the form of hollow sphere the numerical analysis of how specific deformation work depends of different variables like: ZP thickness, specific point in ZP, external pressure that comes from sperm cells were done. According to the model, sperm that make pressure upon ZP surface are in the form of homogeny discrete continuum distribution in radial directions. For specific ZP point in the model, analytical expressions of component stresses and strains were obtained as well as deformations and volume dilatation in ZP. The results are discussed from biomechanical aspect of fertilization. Limitations of the model are also discussed.

©2017 L&H Scientific Publishing, LLC. All rights reserved.

1 Introduction

Zona Pelucida (ZP) is mechanically responsive structure [1, 2] that responses on mechanical stimulation. The ZP can be considered as an oscillatory structure that exhibits transition in oscillatory behaviour before and after fertilization [3, 4]. Using atomic force microscope and Arruda–Boyce eight-chain model viscoelastic properties of ZP could be modelled [2]. A computational model of impact of one sperm to the ZP was done in [5].

During the process of fertilization many spermatozoa will influence the surface of ZP. Spermatozoa are motile cells and in ejaculate there are in range of 10^6 with different velocities and morphological characteristics. Only 10% are functionally capable of fertilizing the oocyte. During the external impact of spermatozoa certain amount of kinetic energy is transfer to ZP. Numbers of progressively motile spermatozoa, as well as their kinetic characteristics are crucial for fertilization success. Different distributions of spermatozoa with same/different

---

[†]Corresponding author.
   Email address: handjelka@gmail.com

kinetic parameters result in different distributions of external forces acting on the ZP surface. Each individual spermatozoid generates certain force that acts upon the ZP surface [6] and their conjoint action will give specific distribution of force on the ZP surface [7]. Currently acceptable opinion in science is that distribution of spermatozoa upon ZP surface is stochastic process –which means that distribution of spermatozoa upon ZP surface is random; it is not symmetric and uniform. Parameters that determine sperm distribution upon ZP surface are not jet identified. Based on results of numerical experiments we suggest possibility of existence of correlation between kinetic parameters of spermatozoa and its impact angle upon ZP surface [8].

The schematic representation of hypothetical sperm distribution upon the ZP surface is presented in Figure 1. Centrally symmetric or asymmetric distribution of external surface forces produced by action of spermatozoa upon ZP surface will cause different stresses, strains and specific deformation work in ZP [7]. Impact of spermatozoa upon ZP surface is not only mechanical but also involved receptor-recognition mechanism. Specific deformation work could be used as a criteria for determine the point/area of ZP where sperm penetration could occurred. The point/are where the specific deformations work has the lowest values there will be the highest probability for sperm penetration. This point/area could be the "weak spot." ZP thickness is an independent parameter that affects the success of *In vitro* fertilization (IVF) protocols: the ticker ZP (smoking, age of female partner, serum levels of follicle-stimulating hormone (FSH) [9, 10]) the lower the probability for conception.

In this paper, using numerical analysis of quasi-static continual ZP model in form of hollow sphere we test how distance from the center of the oocyte affects different parameters relevant for fertilization process like: stresses and strains state at arbitrary point that appear in ZP hollow sphere in the fertilization process; how specific deformation work in ZP and volume dilatation would depend of ZP thickness; and external pressure.

2.1 Stress and strains and specific deformation work in mechanical quasi-static continual ZP hollow sphere model- analytical approach

In the reference [11] local stress and strain state of ZP as well as contact phenomenon between ZP and one spermatozoa are investigated using finite element method (FEM). In present paper we use primarily analytical approach that enables us to analyze impact pressure of many sperm cells at the same time with certain approximations. According to the mechanical approximate quasi-static continual ZP hollow sphere model [7] ZP is in a form of deformable ideal elastic body, bounded by two spheres with inner R_i and outer R_o radiuses of the oocyte, ZP thickness $\delta = R_o - R_i$ in natural, unloaded state before the process of fertilization starts. Outer surface of ZP is exposed to the impact of centrally symmetric distributed pressure of sperm cells. Sperm impact upon the ZP surface is in in the form of discreet homogeneous continuum distribution in radial direction. As differences in mechanical properties on ZP surface could be neglected [12] ZP is considered as homogeneous structure in this model. Although the structural [13] and [1] mechanical differences of inner and outer layers of ZP exists for the simplicity of the ZP hollow sphere model, ZP is considered as a homogeneous structure trough all it's thickness as well as in circular and meridian direction.

Quasi-static continual hollow sphere ZP model (Figure 2) introduces the following approximations:

We made some assumptions of the model: ZP is a structure with ideal linear elastic properties; spermatozoa form uniform arrangement on ZP surface. All spermatozoa have same velocities and sperm impact angles, which result in uniform arrangement of external pressure in radial direction upon the ZP surface. In definite time moment sperm impact is in the form of constant external pressure $\vec{p}_o = -p_o\frac{\vec{r}}{r} = -p_o\vec{r}_0$ in radial direction on the outer surface of hollow sphere ZP model external contour. Pressure on the inner spherical surface of the ZP model is in the form: $\vec{p}_i = p_i\frac{\vec{r}}{r} = p_i\vec{r}_0$, (see Figure 2. a and b). These formulas present vector expressions of external and internal central symmetric specific surface forces – central symmetric pressures distributed along external and internal boundary spherical surface of the model. $\vec{r}_0$ is unique vector in radial direction at corresponding point.. For special case pressure on inner sphere is equal to zero, $p_i = 0$: The thickness of the ZP $\delta = R_o - R_i$ in unperturbed state is uniform. The model and the external discrete continually distributed pressures are centrally symmetric. After deformation the ZP remains symmetric. Displacements of material particles of ZP and on inner and outer ZP surface are central symmetrical and only in radial direction. There is
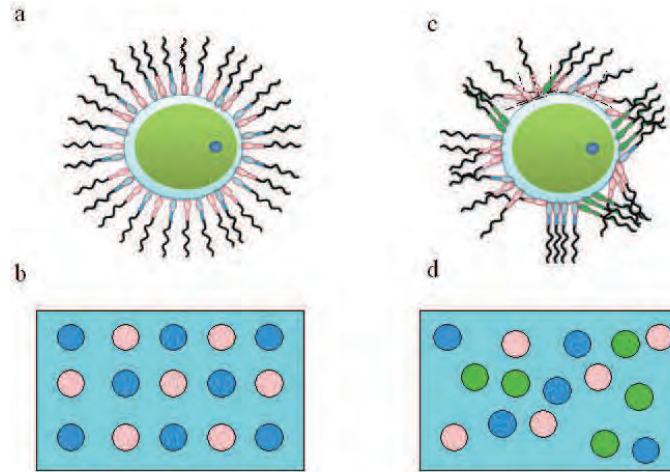
Fig. 1 Hypothetical arrangement of spermatozoa on ZP surface. a. Symmetrical arrangement of spermatozoa having two different swimming velocities and same impact angles. b. Symmetrical distribution of areas with same mechano-chemical impact on ZP surface. c. Asymmetrical arrangement of spermatozoa having three different swimming velocities and different impact angles arbitrary arranged. d. Asymmetrical distribution of areas with same mechano-chemical impact on ZP surface. Different colors of spermatozoa (pink, blue or green) on a and c. denote their different swimming velocities. Different colors on b and d denote areas with different mechano-chemical influence of corresponding spermatozoa. Published in [7]).
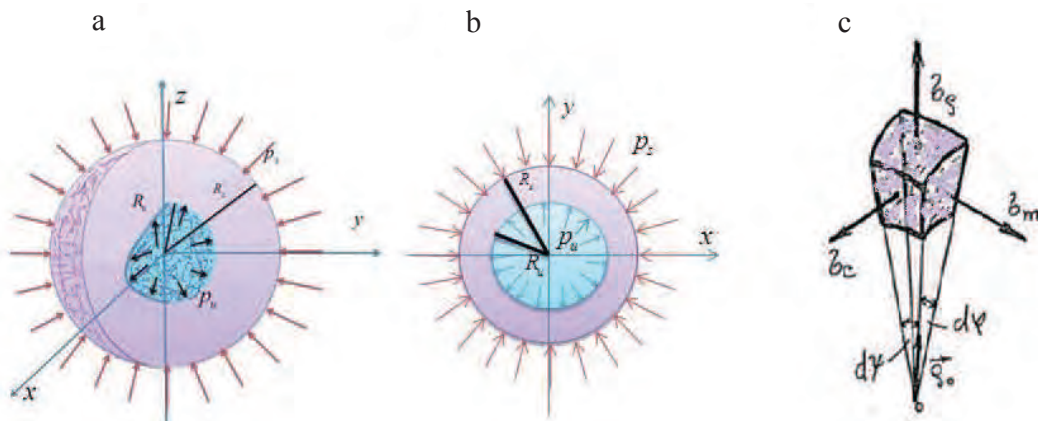
Fig. 2 Mechanical hollow sphere ZP model with centrally symmetric distribution of external pressure a and b. c. Volume element of ZP hollow sphere model in spherical coordinates. The figure was done according to the hollow sphere model l model loaded with internal and external pressure taken from [17].

no shearing stress. In this model we take into account only two static configurations: one in natural stationary state before actions of numerous spermatozoa impacts and final deformed configuration of the ZP under static centrally symmetric pressures. Similar model is presented in Figure 2.

Taking into account previous assumption the problem could be treated as quasi-static. According to the model (Figure 1) and knowledge from Theory of elasticity solved in the books [16, 17] it is possible to write the expressions for component stress, strains, displacements, and specific and total deformation work when hollow sphere ZP model is under constant uniformly distributed central symmetric external and internal pressure [7].

Volume element of ZP (Figure 2c) in spherical coordinates has three main normal component stresses in radial σ_r, circular σ_c and meridional σ_m direction. Analytical expressions of the elements stress tensor of stress

state in the certain point $N(r, \varphi, \vartheta)$ of hollow sphere ZP model are in the form [7, 16, 17]:

$$\sigma_r = \frac{1}{1 - \psi^3}[\psi^3(1 - \frac{R_o^3}{r^3})p_i - (1 - \psi^3\frac{R_o^3}{r^3})p_o], \tag{1}$$

$$\sigma_c = \sigma_m = \frac{1}{1 - \psi^3}[\psi^3(1 + \frac{R_o^3}{r^3})p_i - (1 + \psi^3\frac{R_o^3}{r^3})p_o], \tag{2}$$

Where $\psi = \frac{R_i}{R_o}$, p_o pressure at external couture spherical surface of hollow sphere ZP model, p_i- pressure at internal couture spherical surface of ZP, $r-$ distance from the center of the sphere. Tangential components of the stresses in each point are equal to zero due to central symmetry of the proposed ZP model. Form expressions (1) and (2) we can see that normal component stresses are linear functions of external and internal pressure, but nonlinear function of inner and outer radius of contour ZP surfaces, as well as relation of this radiuses ψ, and nonlinear function of distance r from the center of the sphere in which the normal component stresses are determined.

For the case when specific shear deformations are equal to zero $\gamma_{rc} = 0$, $\gamma_{rm} = 0$ and $\gamma_{cm} = 0$, strain-dilatation of line elements in radial ε_r, circular ε_c and meridian ε_m directions are defined by following expressions [7, 16, 17]:

$$\varepsilon_r = \frac{1}{G(1 - \psi^3)}[\frac{\psi^3 p_i - p_o}{2(1 + 3\mu k)} - \psi^3\frac{p_i - p_o}{2}\frac{R_o^3}{r^3}], \tag{3}$$

$$\varepsilon_c = \varepsilon_m = \frac{1}{2G(1 - \psi^3)}[\frac{\psi^3 p_i - p_o}{(1 + 3\mu k)} + \psi^3\frac{p_i - p_o}{2}\frac{R_o^3}{r^3}], \tag{4}$$

Where G - is shear modulus μ- Poisson ratio of lateral contractions, $k = \frac{1}{1 - 2\mu}$. Previous component of dilatation present approximate elements of the strain tensor of specific deformation for line element in the arbitrary point $N(r, \varphi, \vartheta)$ of the ZP model.

From expressions (3) and (4) we can conclude that dilatations –specific deformations of line elements in certain point of ZP are linear functions of external and internal pressures, nonlinear function of inner and outer radius of the oocyte, as well as relation of this radiuses ψ, and nonlinear function of distance r from the center of the oocyte in which the component dilatation are determined.

Volume element of ZP model (Figure 2.c) expressed in sphere coordinates is with sides:

$$dr, r\cos\psi d\varphi \text{ and } rd\psi \text{ is}: dV = r^2\cos\psi dr d\varphi d\psi.$$

Volume dilatation ε_V of ZP volume element in the point $N(r, \varphi, \vartheta)$ at distance r from the center of the oocyte has the following form:

$$\varepsilon_V = \varepsilon_r + \varepsilon_c + \varepsilon_m = \frac{3}{2G(1 + 3\mu k)}\frac{\psi^3 p_i - p_o}{1 - \psi^3}, \tag{5}$$

From expression (5), we can conclude that volume dilatation ε_V is linear function of external and internal pressure, nonlinear function of inner and outer radius of the oocyte, as well as relation of these radiuses ψ. Volume dilatation ε_V is not the function of distance r from the center of the oocyte. This volume dilatation is the same in all points of this hollow sphere ZP model due to central symmetry of stress and strain states. Volume dilatation is first invariant ε_1 of deformation and is sum of tree orthogonal line specific deformations, or sum of three principal strains. In our case, principal strains (dilatations) are: $\varepsilon_r = \varepsilon_1$, $\varepsilon_c = \varepsilon_2$ and $\varepsilon_m = \varepsilon_3$, and is same as expression (5). Second invariant of deformation at corresponding point is in the form:

$$\varepsilon_2 = \varepsilon_r\varepsilon_c + \varepsilon_r\varepsilon_m + \varepsilon_m\varepsilon_c \tag{6}$$

Third invariant ε_3 of state deformation at considered body point is multiplication of tree principal strains (dilatations):

$$\varepsilon_3 = \varepsilon_r\varepsilon_c\varepsilon_m \tag{7}$$

For each point of deformed body independently of system coordinates used for expression of elements of deformation tensors, invariants of deformation in a form of scalar of matrices of tensor deformation are independent of coordinate system. Relation between first invariant of stress and strain state is in the form: $N_1 = \sigma_r + \sigma_c + \sigma_m$ and deformation $\varepsilon_1 = \varepsilon_V$ is:

$$N_1 = \sigma_r + \sigma_c + \sigma_m = \frac{E}{1-2\mu}\varepsilon_1 = \frac{E}{1-2\mu}\varepsilon_V = \frac{(1+\mu)G}{1-2\mu}\varepsilon_V \tag{8}$$

In the case of centrally symmetric straining of hollow sphere ZP model, invariant of stress in certain point is:

$$N_1 = \sigma_r + \sigma_c + \sigma_m = \frac{(1+\mu)}{(1-2\mu)}\frac{3}{2(1+3\mu k)}\frac{\psi^3 p_i - p_o}{1-\psi^3} \tag{9}$$

Other stress state invariants N_2 and N_3 in the stressed hollow sphere ZP model are:

$$N_2 = \sigma_r\sigma_c + \sigma_r\sigma_m + \sigma_m\sigma_c \tag{10}$$

$$N_3 = \sigma_r\sigma_c\sigma_m \tag{11}$$

because in considered stressed state of hollow sphere ZP model principal stress state directions ate radial, circular and meridional, and principal stresses are normal stresses $\sigma_r = \sigma_1$, $\sigma_c = \sigma_2$ and $\sigma_m = \sigma_3$. Component shearing stresses are equal to zero.

Using expressions (1-5) it is possible to analyze quasi-static component stresses and deformations around each ZP point in the model including points on the contour boundary surfaces of the proposed ZP model for the case when sperm cells are impacting external ZP surface in the form of external discreet continual distribution of surface forces.

2.2   Specific deformation work in continual hollow sphere ZP model

Deformation work of volume element of hollow sphere ZP model could be determined through component stresses and strains Specific deformation work could be express via pressure on the external and inner contour surfaces.

$$\mathbf{A}'_{def} = \frac{3}{2G(1-\psi^3)^2}\Big[\frac{(2+3\mu k)}{4(1+3\mu k)^2}\big(\psi^3 p_u - p_s\big)^2 + \psi^6 \frac{(p_u - p_s)^2}{4}\frac{1}{r^6}\Big], \tag{12}$$

Expression (12) is new and presents original results obtained on (1)-(2) and (5)-(6) and references [7, 16, 17].

According to the expression (12) specific deformation work - elastic potential of the deformed configuration of the hollow sphere ZP model in certain point $N(r, \varphi, \vartheta)$ is function of radiuses of boundary inner and outer spherical contour surfaces, square of inner and outer continually distributed pressures. Specific deformation work also depends inversely proportioned with distance r from center of spherical surfaces with sixth degree r^{-6} and with ratio of inner and outer spherical radiuses ψ^6. It is possible to make the analogy between deformation and occurrence of deformation work under external pressure caused by sperm cells. If we supposed that minimal and maximal values of specific deformation work of ZP in certain area contribute to the sperm penetration after ZP deformation (caused by impact pressure of numerous sperm cells upon the ZP surface in the form of discreet continuum distribution) we may conclude that specific deformation work in specific ZP point in this quasi-static model depends on radius of contour surfaces, square of inner and outer surface pressures, distance from the center of the sphere with ratio r^{-6}, relation of external and internal radius of the sphere ψ^6, and inversely proportioned to the shear modulus.

3.1   Stress and strains and specific deformation work in mechanical quasi-static continual hollow sphere ZP model-numerical approach

Now, we are interested in numerical analysis how of stress, strain, volume dilatation, and specific deformation work are related to: point distance from the center of the sphere, ZP thickness, ratio of the inner and outer radius,
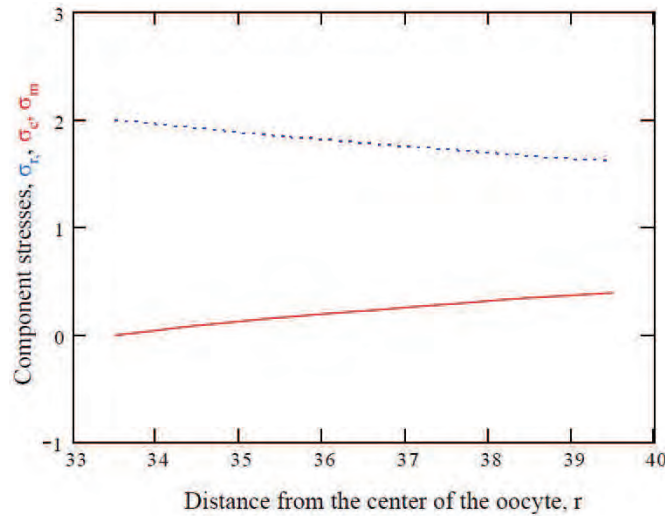
Fig. 3 Graph of normal component stresses in radial (σ_r), -circular (σ_c) and meridional (σ_m)- direction as a function of distance from center of the oocyte r, $R_o = 40\ \mu m$, $R_i = 33.5\ \mu m$, $\delta = R_0 - R_i = 6{,}5\ \mu m$, $p = 100\ \text{pN}/\mu\text{m}^2$. $r = 33.5, \dots, 40$ μm Graph of normal component stresses in circular (σ_c) and meridional (σ_m) direction are the same.

external pressure (different number of the sperm cells that impact pressure on external contour of the ZP surface) in the continual hollow sphere ZP model.

We are going to use the parameters from the literature that are related to mouse oocyte. Oocyte dimensions and ZP thickness are taken from [18]. $R_o = 40\ \mu m$, $R_i = 33.5\ \mu m$, ZP thickness in non-deformed state $\delta = R_0 - R_i = 6{,}5\ \mu$m. Values for shear modulus is taken from [19] and corresponds to agarose gels: $7{,}1\pm2{,}1$ KPa (approximately 710 Pa) *Poisson* ratio μ was set to 0.45.

As there is no experimental data for pressure that sperm head could generate upon the ZP surface during the impulsive impact (there are some data what is the work per sperm sell per pulse, $4{,}6 \times 10^{-16}$ *J* amplitude $9{,}8\pm2{,}6$ Nn and frequency 3,5-19,5 Hz, but as we don't have the values for sperm contact area the data are related to the bull sperm cells) [20] total pressure generated by sperm cells upon ZP surface was taken arbitrary as $100\ \text{pN}/\mu\text{m}^2$.

Component normal stress in radial (σ_r), -circular (σ_c) and meridional (σ_m)-directions as a function of distance from the center of the oocyte, $r_{(equations 1 and 2)}$ are presented in the Figure 3.

As the distance of the center of the oocyte increases, the radial component of normal stress increases too, but circular and meridian $\sigma_c = \sigma_m$ component of normal stress decreases (Figure 3 and 4). Radial component of stress is higher in points that are closer to the outer surface contour.

Graph of function of specific deformation in radial direction ε_r as well in circular and meridional direction $\varepsilon_c = \varepsilon_m$ as a function of distance from the center of the sphere/oocyte r are shown on Figure 5 and have same features as corresponding normal stresses. Deformation-stress curves $\sigma_r(\varepsilon_r)$ and $\sigma_c(\varepsilon_c = \varepsilon_m) = \sigma_m(\varepsilon_c = \varepsilon_m)$ for these conditions are obtained from equation (3 and 4) and shown in Figure 6.

Volume dilatation ε_V (equation 5) dependence of external pressure (0-1000 pN/μm2-approximate values and for the case when pressure on the inner ZP surface in the model is $p_i = 0$) are shown in Figure 7. As external pressure increases, the absolute value of volume dilatation increases. The volume dilatation is negative as external pressure increases - when numerous sperm cells impact (with impulsive forces) upon ZP surface causing its compression.

Specific deformation work $\mathbf{A'}_{def}$ as a function of distance from the center of the oocyter space in the point $N(r, \varphi, \vartheta)$ from the center of the oocyte (equation 5) is shown in the Figure 8. External pressure p_o is arbitrary taken as $100\ \text{pN}/\mu\text{m}^2$ and internal pressure as $p_i = 0$. According to the graph, we may conclude that points $N(r, \varphi, \vartheta)$ that are closer to the external surface of ZP, would have lower the specific deformation work $\mathbf{A'}_{def}(r)$.
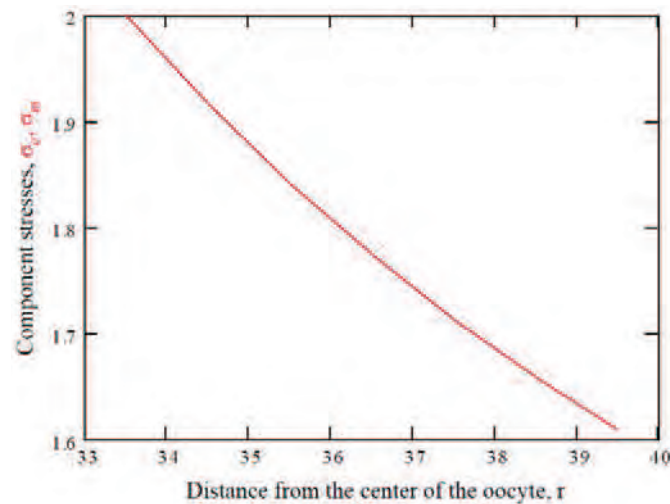
Fig. 4 Graph of normal stress in circular and meridional direction $\sigma_c = \sigma_m$ as a function of distance from the center of the sphere/oocyte γ.
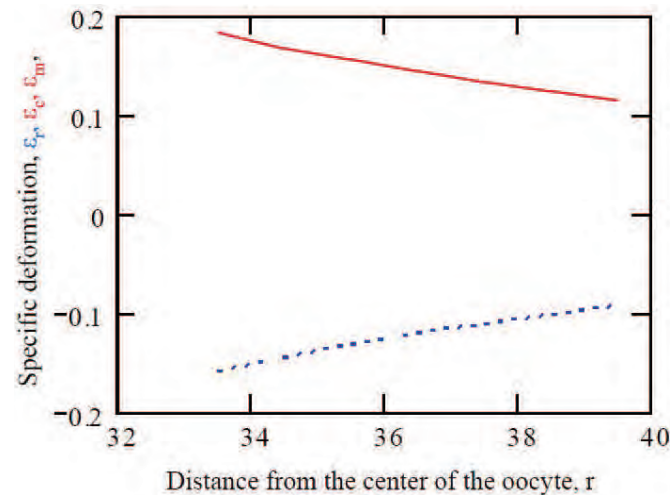

Fig. 5 Graph of function of specific deformation in radial ε_r and circular and meridional $\varepsilon_c = \varepsilon_m$ direction as a function of distance from the center of the sphere. $R_0 = 40 \ \mu m$, $R_i = 33.5 \ \mu m$, μ was set to 0.45. For shear modulus G 710 Pa from [17] and arbitrary values for external pressure of 100 pN/ μm^2, $p_i = 0$.

How specific deformation work $\mathbf{A}'_{def}(p_0, r)$ depends on external pressure p_0 on a distance $r = 36 \ \mu m$ from the center of the oocyte is shown in Figure 9. The higher the external pressure p_0 the higher the deformation work would be. If the number of sperm cells that act upon ZP surface increases the ZP would exhibit higher specific deformation work in certain point. The dependence is not linear but parabolic. In each point $N(r = cinst, \varphi, \vartheta)$ on surface $R_{i \leq r} = const \leq R_0$ specific deformation work $\mathbf{A}'_{def}(p_0, r = const) = const 1$ is constant, which is result of central symmetry of the model and supposed external pressure load.

From Figure 10 we can see that volume dilatation is negative. The ZP is compressed: in the points in the inner area of the ZP the absolute values of volume dilatation $\varepsilon_V(R_i)$ are higher, if the other parameters of the model are constant. According to the graph on Fig.10, ticker ZP would be less compressed. In clinical practices oocyte that have ticker ZP compare to physiological values, have less probability to be fertilize. Our numerical analysis show that volume dilatation-compression in ticker ZP would have lower values. This indicates that in ticker ZP volume dilatation/compression obtained by certain amount of sperm cells could not reach critical value for sperm penetration.
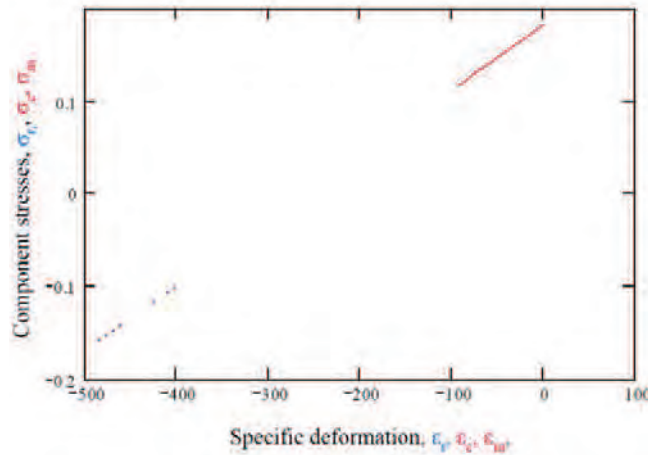
Fig. 6 Stress-deformation curves in radial $\sigma_r\,(\varepsilon_r)$ as well in circular and meridional direction $\sigma_c\,(\varepsilon_c = \varepsilon_m) = \sigma_m\,(\varepsilon_c = \varepsilon_m) - R_0 = 40\;\mu m,\;R_i = 33.5\;\mu m,\;\mu$ was set to 0.45. For shear modulus G 710Pa from [17] and arbitrary values for external pressure of 100 pN/ μm^2, $p_i = 0$.
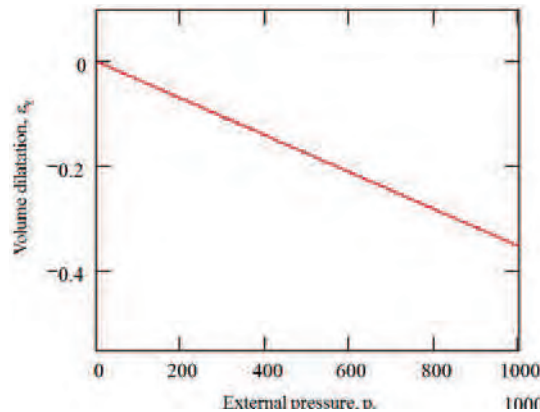

Fig. 7 Volume dilatation $\varepsilon_V\,(p_s)$ as a function of external pressure p_s. As external pressure increases (corresponds to the larger number of sperm cells) increases the absolute values of intensity of volume dilatation –compression (negative values on graph). $R_0 = 40\;\mu m,\;R_i = 33.5\;\mu m,\;\mu$ was set to 0.45. For shear modulus G 710 Pa from [17] and arbitrary values for external pressure from 0-1000 pN/ μm2, $p_i = 0$.

3.2   Limitations of the model

In real process of fertilization, sperm distribution is not centrally symmetric and the pressure generated by sperm cells is not uniform but depends of kinetic parameters of the sperm cells that are different for sperm cells even in the same ejaculate. For mentioned reasons the dynamical model of ZP, should be considered. The basic dynamical shell-like model of ZP was proposed in [7]. However, for solving this dynamical problem additional analytical, numerical and experimental data are needed.

One of the crucial questions in fertilization process is how ZP is doing the selection of sperm cell? How ZP select just one specific sperm and way that one? One of the biochemical explanations for this process is receptor recognition. Sperm cell that touches the oocyte plasma membrane first will fertilize the oocyte. The very process of penetration is not clarified. Different mechanisms of sperm penetration trough ZP are proposed in the literature: receptor recognition, oscillations of relaxation [11, 21]. According to the oscillatory model of fertilization [22] the condition for sperm penetration is resonance between oscillatory mods of single sperm cell and eigen mods of oscillation of ZP [22]. It is still not known if the predilection week spot/area in ZP exists, like structural imperfections in ZP predilected for sperm penetration, or predilected spot/area of sperm penetration
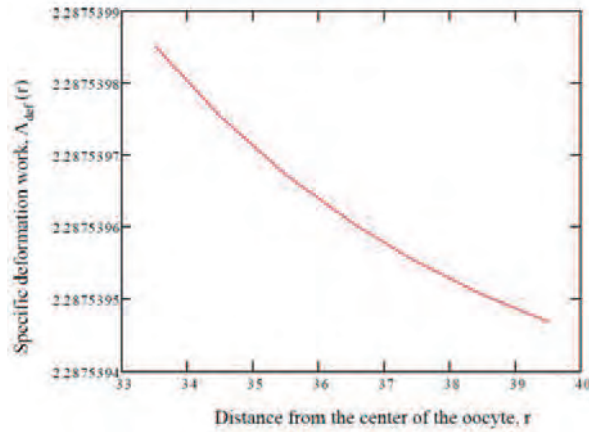
Fig. 8 Graph of specific deformation work $A'_{def}(r)$ as a function of distance from the center of the sphere r in the point $N(r,\varphi,\vartheta)$ from the center of the sphere. $R_0 = 40\ \mu m$, $R_i = 33.5\ \mu m$, μ was set to 0.45. For shear modulus G 710Pa from [17] and arbitrary values for external pressure 100 pN/μm^2, $p_i = 0$.
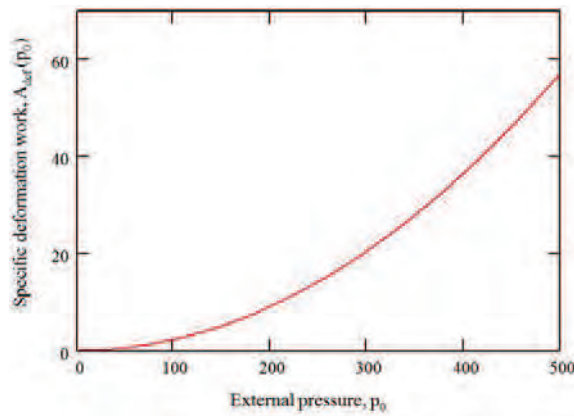
Fig. 9 Graph of specific deformation work $A_{def}(p_0)$ as a function of external pressure p_0 in the point $N(r,\varphi,\vartheta)$ at the distance $r = 36\ \mu m$ from the center of the sphere. $R_0 = 40\ \mu m$, $R_i = 33.5\ \mu m$, μ was set to 0.45. For shear modulus G 710Pa from [17] and arbitrary values for external pressure $p_0 = 500$ pN/μm^2, $p_i = 0$.
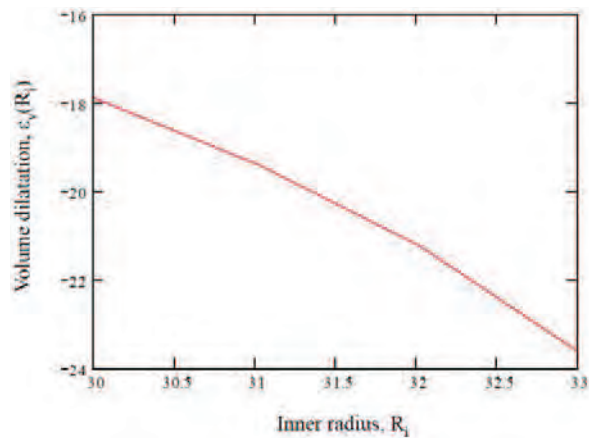
Fig. 10 Graph of volume dilatation $\varepsilon_V(R_i)$- as a function of inner radius for arbitrary taken external pressure values 100 pN/μm^2 and inner pressure $p_i = 0$. $R_0 = 40\ \mu m$, $R_i = 33.5\ \mu m$, μ was set to 0.45. For shear modulus G = 710Pa from [17].

is determined by specific set of pressure distribution on outer ZP surface?

We are of opinion that dynamical model that take into account non-uniform pressure distribution could be helpful in solving this problem. Dynamical ZP model described in [7] take into account stress and strain state of ZP that are time depended, unlike quasi-static hollow sphere ZP model that takes into account two states-before and after deformation. In dynamical ZP model [7] is considered case when distribution of pressure upon ZP surface is centrally symmetric and uniform. For the case that distribution of pressure is not uniform and not centrally symmetric (which will correspond to the real in vitro fertilization process) it is expected that parameters like volume dilatation, stress and specific deformation work in certain point of ZP are time dependent and depend of distribution of surface pressure. It is expected that points in ZP that are on same distance from the center of the oocyte will have different volume dilatation, stress state and deformation work depending of non-uniformity of surface pressure. In that case it would be possible to determine in what area volume dilatation or stress has minimal/maximal value depending of surface pressure distribution. Introducing the time as a parameter into the model would enable critical time necessary for certain are in ZP to get into critical deformation/stress state. As in this dynamical model we would have two new parameters –time and non-uniform surface pressure distribution, solving this problem would require numerical approach. Our further investigation would be oriented in further developing and improving the proposed [7] dynamical ZP model.

4 Discussion and Conclusions

We proposed quasi-static linear hollow sphere ZP model with central symmetric external surface loading. Analytical expressions and numerical multi-parametric analysis for stress and strain state, volume dilatation and specific deformation work in the certain point of hollow sphere ZP model are obtained. Stress and strain state in certain point in hollow sphere ZP model show nonlinear dependence of: relation of inner and outer radiuses of the oocyte ψ, distance from the center of the oocyte r^3 (opposite proportional), and outer radius of the oocyte R_0 (R_0^3), but linear dependence of external pressure p_0. Volume dilatation at certain point in ZP model is inversely proportioned to the shear modulus G. Specific deformation work shows nonlinear dependence of inner and outer radiuses of the oocyte, ψ, external pressure (p_0^2), distance from the center of the oocyte r^6(opposite proportional) and linear dependence of shear modulus G (inversely proportional). It follows that the value of the specific deformation work in certain point of ZP model is the most influence by: thickness of the ZP, number of sperm cells that affect ZP surface (increases with the square of the pressure producing by spermatozoa)) and the specific point in the thickness of the ZP.

Our numerical analysis show that volume dilatation-compression in ticker ZP would have lower values. This indicates that in ticker ZP volume dilatation/compression obtained by certain amount of sperm cells could not reach critical value for sperm penetration. As the ZP thickness increases the higher absolute values of volume dilatation – higher compression of ZP would be necessary/or the higher force/energy is needed to sperm to penetrate trough ZP thickness. In clinical praxis ticker, ZP is associated with lower IFV protocol success and sterility. Theoretically, sperm cell needs more energy to penetrate some critical ZP thickness. As the energy of each motile sperm cell decreases in time, that could mean that this energy could be depleted before sperm cells passes the critical distance trough ZP thickness.

Some questions remain open: what is the balance of ZP thickness and applied external pressure (number of spermatozoa) that result in values of specific deformation work in ZP that are suitable for successful sperm penetration? Is the maximum specific deformation work a condition for sperm penetration? If it is, the whole process of sperm penetration would be energetically non-rentable and would destroy the minimum energy principle.

Considering that proposed model is static, specific deformation work in certain point of ZP in fertilization process could be conceder as elastic potential that could repulse the out coming sperm cell or allow sperm penetration in the point of specific minimal deformation work. If the specific deformation work at arbitrary point of the model could be considered as resistance that sperm cell have to overcome and is result of reaction at external pressure, minimal deformation work would be the principal of sperm penetration.

In the hypothesis of plastic deformation and flow, minimal stresses and minimal specific deformation work should be use as criteria for damage of material or for its plastic flow.

The idea is that plastic deformation and plastic flow of viscoelastic material occurs when material is exposed to the certain minimal value of specific deformation work. This critical deformation work in certain point/area of ZP could lead to weakening of the material (ZP) and its plastic flow. It is possible that this local plastic flow of ZP could initiate the process of sperm penetration.

Acknowledgments

References

[1] Murayama, Y., Mizuno, J., Kamakura, H., Fueta, Y., Nakamura, H., and Akaishi, H. (2006), Mouse zona pellucida dynamically changes its elasticity during oocyte maturation, fertilization and early embryo development, *Human Cell*, **19**, 119-125.

[2] Boccaccio, A., Lamberti, L., Papi, M., De Spirito, M., Douet, C., Goudet, G., and Pappa- lettere, C. (2014), A hybrid characterization framework to determine the visco- hyperelastic properties of a porcine zona pellucida, *Interface Focus*, **4**, 20130066. http://dx.doi.org/10.1098/rsfs.2013.0066.

[3] Hedrih, A. (2014), Transition in oscillatory behaviour in mouse oocyte and mouse embryo through oscillatory spherical net model of mouse Zona Pellucida, in Applied Non-Linear Dynamical Systems, Springer Proceedings in Mathematics & Statistics 93, J. Awrejcewicz (ed.), **93**, 295-303. Springer International Publishing Switzerland 2014 ISBN 978-3-319-08265-3; DOI 10.1007/978-3-319-08266-0_21.

[4] Hedrih, N.A. and (Stevanović) Hedrih, R.K. (2014), Analysis of energy state of discrete fractional order spherical net of mouse zona pellucida before and after fertilization, *International Journal of Mechanics,* SI, **8**, 371-376.

[5] Kozlovsky, P. and Gefen, A. (2013), Sperm penetration to the zona pellucida of an oocyte: a computational model incorporating acrosome reaction, *Computer Methods in Biomechanics and Biomedical Engineering*, **16**(10), 7.

[6] Hsiao, W.W., Liao, H.S., Lin, H.H., Ding, R.F., Huang, K.Y., and Chang, C.S. (2013), Motility Measurement of a Mouse Sperm by Atomic ForceMicroscopy, *Analtycal Science*, **29**, 3-8.

[7] Hedrih, N.A. and Hedrih (Stevanovic), R.K. (2015), Deformation work of Zona Pelucida in process of fertilization. 13th International Conference on Dynamical Systems - Theory and Applications, Proceedings-Mechatronics and Life Sciences, DSTA Lody 2015, Edited by J.A. Awrejcewicz, M. Kazmierczak, J. Mrozowski, P. Olejnik, Lodz, December 7-10, 2015, Poland, ISBN 978-83-7283-707-3, Department of Automation, Biomechanics and Mechatronics, Lodz, 217-226.

[8] Hedrih, A., Lazarevic, M., and Mitrovic-Jovanovic, A. (2015), Influence of sperm impact angle on successful fertilization through mZP oscillatory spherical net model, *Computers in Biology and Medicine*, **59**, 19-29.

[9] Shiloh, H., Lahav Baratz, S., Koifman, M., Ishai, D., Bidder, D., Weiner-Meganzi, ZM., and Dirnfeld, M. (2004), The impact of cigarette smoking on zona pellucida thickness of oocytes and embryos prior to transfer into the uterine cavity, *Human Reproduction*, **19**(1), 157-159.

[10] Jennings, C.P., Merriman, A.J., Beckett, L.E., Hansbro, M.P., and Jones, T.K. (2011), Increased zona pellucida thickness and meiotic spindle disruption in oocytes from cigarette smoking mice, *Human Reproduction*, **26**(4), 878-884. doi:10.1093/humrep/deq393.

[11] Hedrih, A. and Banic, M. (2016), The effect of friction and impact angle on the spermatozoa - oocyte local contact dynamics, *Journal of Theoretical Biology*, **393**, 32-42.

[12] Murayama, Y., Constantinou, E.C., and Omata, S. (2004), Micro-mechanical sensing platform for the characterization of the elastic properties of the ovum via uniaxial measurement, *Journal of Biomechanics*, **37**, 67-72.

[13] Martinova, Y., Petrov, M., Mollova, M., Rashev, R., and Ivanova, M. (2008), Ultrastructural study of cat zona pellucida during oocyte maturation and fertilization, Animal Reproduction Science, **108**, 425-434.

[14] Papi, M., Brunelli, R., Familiari, G., Frassanito, M.C., Lamberti, L. et al. (2012), Whole-Depth Change in Bovine Zona Pellucida Biomechanics after Fertilization: How Relevant in Hindering Polyspermy?, *PLoS ONE*, **7**(9), e45696. doi:10.1371/journal.pone.0045696.

[15] Boccaccio, A., Frassanito, M.C., Lamberti, L., Brunelli, R., Maulucci, G., and Monaci, M. et al. (2012) Nanoscale characterization of the biomechanical hardening of bovine zona pellucida. Journal *of theRoyal Society, Interface*, **9**, 2871-2882. doi:10.1098/rsif.2012.0269.

[16] Hedrih (Stevanović), R.K. (1988), Izabrana poglavlja Teorije elastičosti, Masinski fakultet Univerziteta u Nisu.pp 424. http://hdl.handle.net/123456789/3766

[17] Rašković, P.D. (1985),*Teorija elastičosti* (*Theory of Elasticity),* Nauča knjiga, 1985, 414. http://hdl.handle.net/123456789/3765

[18] Wassarman, P.M. and Litscher, E.S. (2012), Influence of the zona pellucida of the mouse egg on folliculogenesis and fertility, The *International Journal of Developmental Biology*, **56**, 833-839. doi: 10.1387/ijdb.120136pw

[19] Glozman, T. and Azhari, H. (2010), A Method for Characterization of Tissue Elastic Properties Combining Ultrasonic Computed Tomography With Elastography, *Journal of Ultrasound in Medicine*, **29**, 387-398.

[20] Allen, M.J., Rudd, R.E., Mc Elfresh, M.W., and Balhorn, R. (2010), Time-dependent measure of a nanoscale force-pulse driven by the axonemal dynein motors in individual live sperm cells, *Nanomedicine: Nanotechnology, Biology, and Medicine*, **6**, 510-515.

[21] Green, D.P.L. and Purves, R.D. (1984), Mechanical Hypothesis Of Sperm Penetration, *Biophysical Journal*, **45**, 659-662.

[22] Hedrih, A. (2011), Modelling oscillations of zona pelucida before and after fertilization. ENOC Young Scientist Prize Paper. *EUROMECH Newsletter* 40, Europian Mechanics Society, **40**, 6-14.

[23] Bedford, J.M. (2006), Why do penetrating sperm create an oblique path in the zona pellucida?, *Reproduction*, **131**, 23-25.

[24] Papi, M., Sylla, L., Parasassi, T., Brunelli, R., and Monaci, M. et al. (2009), Evidence of elastic to plastic transition in the zona pellucida of oocytes using atomic force spectroscopy, *Applied. Physical. Letters*. **94**, 153902.

Fatigue Cracks Detection in Rectangular Plates with Circular Hole with the Use of Elastic Waves

Marek Barski[†], Adam Stawiarski, Piotr Pająk

Department of Mechanical Engineering, Cracow University of Technology, 37 Jana Pawła II Street, 31-864, Cracov, Poland

Abstract

The current work is devoted to the problem of fatigue cracks detection and evaluation in the case of isotropic rectangular plates with circular holes. The cutout is located in the geometrical center of the plate. The structure is subjected to the cyclic tension. It causes the formation of the fatigue cracks in the vicinity of the hole. This type of damages can be effectively detected by the analyzing of elastic waves propagation. In the presented work the propagation of the elastic waves in the vicinity of a hole is simulated with the use of the finite element method. It is assumed that the elastic waves are excited and picked up by piezoelectric sensors. The most effective position of the piezoelectric actuator is looked for while the position of the array of sensors is fixed. Four different possibilities of the location of the actuator are studied. Moreover, the advanced algorithm of crack detection and evaluation is also discussed.

©2017 L&H Scientific Publishing, LLC. All rights reserved.

1 Introduction

Nowadays the problem of detection of various defects in engineering structures is becoming very important. For this purpose, advanced systems known as SHM (Structural Health Monitoring), are designed. According to Rytter [1], we can distinguish four levels of the SHM systems, namely:

- level 1: detection of damage,

- level 2: detection and localization of damage,

- level 3: detection, localization and evaluation (type, size, orientation, etc) of damage,

- level 4: estimation of lifetime of structure with detected damage.

Additionally, together with discovering smart materials (shape memory alloys), another level of the SHM systems should be taken into consideration. This level is strictly connected with the possibility of self-repairing of

---

[†]Corresponding author.
Email address: mbar@mech.pk.edu.pl

the structure, where the damage has been detected (Park et al. [2]). However, the majority of works are devoted to the SHM systems of the 1 and 2 levels. It seems that designing the SHM systems of the 3 level is very difficult.

In order to investigate a structure, the propagation of elastic waves is very frequently used to detect various defects in solid structures. Depending on the properties of the medium in which the wave propagates we can distinguish different types of waves. The comprehensive description of those waves can be found in numerous monographs, for example: [3–5]. It is worth noting here that in practical applications two types of elastic waves are mainly used. They are Lamb waves [6] and Rayleigh waves [7]. The waves are most frequently generated by using piezoelectric transducers. Regardless of the type of the applied elastic waves, damage is detected and located by means of substantially two methods, i.e. Pulse - Echo and Pitch - Catch [8]. The Pulse - Echo method is based on recording the signal which is reflected from a flaw. Here the actuator and sensors are placed on the same side of the investigated structure. In the Pitch - Catch configuration, the elastic waves travel across the investigated structure and they are then captured by a sensor at the other end of the wave path. If a defect is present in the object, the signal captured by the sensor will be changed and will be different from the signal received in the case of an intact structure. Moreover, using the array of sensors, it is possible not only to detect damage but also precisely locate and evaluate it.

The above-discussed methods are successfully applied in the case of rails [9], pipes and cylinders [10, 11] or thin-walled structures like, for example, elements of aircraft skin [12, 13]. The method based on the propagation of the elastic waves can also be applied in the case of composite materials in order to detect defects which are characteristic for this kind of materials, e.g. matrix cracking, delaminations or fiber debonding [14, 15]. They can also be used to evaluate mechanical properties (spring constants) of composite materials [16] thickness measurement [17] or phase velocity [18].

The work presented in this article is devoted to the problem of detecting and evaluating a fatigue crack which is localized in the vicinity of a hole. The existence of different perforations in members of support structures is necessary due to, for example, fuel or hydraulic lines, rivet joints or simply reduction of the structure's weight. Moreover, all discontinuities of this kind cause stress concentration which, in consequence, can trigger the fatigue crack growth. It especially happens when the object is subjected to the cyclic tension. In practice, the access to the places where the holes are present can be often very difficult or even impossible. Therefore, development of the special SHM system which is dedicated to this problem seems to be very important. However, this task is rather complicated mainly due to the reflection of the incident wave from the edges of the hole. The detection of the crack is rather easy, though. The main problem is connected with the effective evaluation of the crack length.

Only a few papers can be quoted where similar investigations are carried out. Chang and Mal [19] studied scattering of Lamb waves in the vicinity of the rivet hole. They used a modified finite element method (global local FE). The theoretical results were compared with experimental ones and a broad agreement was observed between them. Fromme and Sayir [20] analyzed also scattering of the guided wave (anti-symmetric A0 mode of the Lamb wave) in the vicinity of the rivet hole. They observed a significant reduction of the amplitude of the received signal in the case of the structure with a crack. They also conducted numerical simulations with the use of a different finite method. The work by Hong et al. [22] has also been devoted to the problem of detection and localization of a fatigue crack on the edge of the hole. The numerical simulations of elastic waves propagation are also performed by Barski et al. [24] and Stawiarski et al. [25].

In the above-mentioned papers, the experimental studies are generally compared with the numerical simulations. However, there are also available works in which a pure analytical approach is utilized. For example, in the work by Grahn [21], the scattering problem of an incident plane symmetric S0 Lamb wave in a plate with a circular partly through-thickness hole is considered. McKeon and Hinders [23] studied the Lamb waves scattering in the vicinity of the hole in an analytical manner.
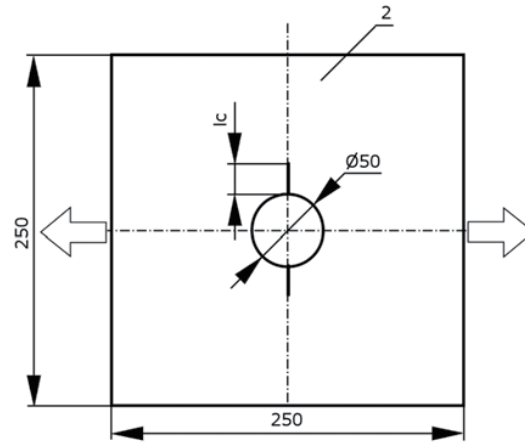
Fig. 1 Investigated aluminum square plate with circular hole l_c denotes the crack length.

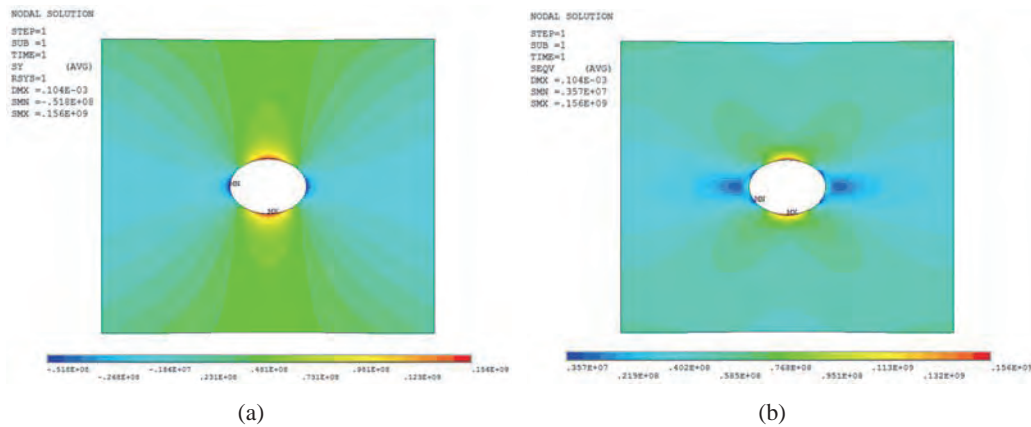

(a)   (b)

Fig. 2 Stress distribution in uniformly stretched plate a) Circumferential component of stress, b) stress equivalent.

2 Analyzed structure

The analyzed structure is shown in Fig. 1. It is the square plate with the circular hole placed in the geometric center of the structure. The length of the external edge is equal to $a_0 = 250$ [mm] and the diameter of the cutout $d = 50$ [mm]. The structure is made of the aluminum alloy PA38 with the following mechanical properties: $E = 69.5$ [GPa], $v = 0.33$, and the density $\rho = 2700$ [kg/m^3]. It is assumed that the studied structure is subjected to the uniform tension in the horizontal direction, which is symbolically shown in Fig. 1 (a horizontal arrow).The applied load (uniform pressure or uniform displacement) causes stress concentration in the vicinity of the hole. The distribution of the circumferential stress component and the stress equivalent is shown, respectively, in Fig. 2. These figures are obtained as a result of a basic finite element analysis. Both vertical edges have been uniformly stretched, where $\Delta u = 0.01$ [mm]. The maximum value of the circumferential stress component (tension) is about three times greater in comparison with the absolute value of the minimal stress component (compression). Moreover, the circumferential stress component is dominant. It is confirmed by the fact that the maximum equivalent stress is identical with the maximum circumferential stress component. In the case of a cyclic load, in the areas where the circumferential stresses achieve their maximum, the fatigue crack can be initiated. After damage initialization, the crack will grow strictly in the vertical direction. It is shown in Fig. 1. Therefore, the main aim of this work is to design the SHM system of the 3-th level. The proposed SHM system not only should detect the crack at an early stage of its creation but it also should enable the estimation of the actual length of the crack. It is necessary in order to determine the safe lifetime of the structure.
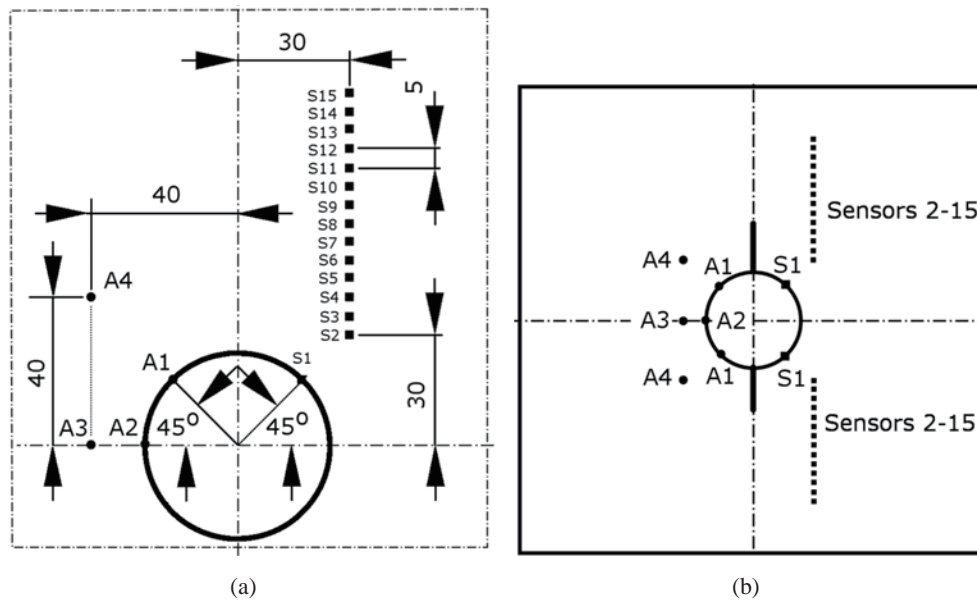
Fig. 3 Localization actuators and sensors [mm] a) dimensions b) general view.

3 Designed SHM system

The proposed SHM system utilizes Lamb waves that propagate through plates. It is based on the comparison of the signal received in the case of the intact structure with the signal from the structure that contains damage. This kind of an approach is called a Pitch - Catch method. An appropriate signal is generated by a single piezoelectric actuator and next the incident wave is received by the array of piezoelectric sensors. The localization of the sensors is constant and it is shown in Fig. 3. One sensor, S1, is placed directly on the edge of the cutout. If the crack is very small (an initial stage of the crack growth), this sensor should immediately indicate the presence of a flaw. To estimate the actual length of the crack, 14 sensors are installed in the vicinity of the hole, i.e. sensors S2 - S15. The distance between these sensors is constant and equal to $l_s = 5$ [mm]. The exact localizations of the mentioned piezoelectric elements are depicted in Fig. 3. The detailed description how to evaluate the crack length taking into account the information obtained from the sensors is discussed in the next section. The effectiveness and sensitivity of the developed SHM system depends on the optimal position of the actuator. In Fig. 3, there are presented possible localizations of the actuators, namely: a) the A1 actuator is placed at the point where the edge of the hole is intersected by the line which starts from the geometrical center of the hole and is oriented at an angle of 45° with respect to the horizontal direction, b) the A2 actuator is also located on the edge of the hole at the point where the horizontal line intersects the edge of the cutout, c) the A3 actuator is shifted to the left with respect to the A2 sensor, d) the A4 actuator is placed at some distance from the hole

In cases a) and b), the incident wave propagates along the edge of the cutout and any additional effects connected with the reflection are avoided. However, in cases c) and d) the incident wave at first is reflected from the free edge of the hole and then is received by the sensors. This fact can make the process of damage detection more difficult. It has to be noted that in the real structure the crack grows on both sides of the hole in the vertical direction. Therefore, identical set of sensors has to be installed in a symmetric manner with respect to the horizontal axis of symmetry of the hole. Moreover, taking under consideration the symmetry of the investigated structure, in cases a) and d) it is also necessary to use a pair of actuators which should be activated sequentially in order to test the bottom and top surroundings of the hole.

4 An applied method for fatigue damage detection

The proposed SHM system is based on the comparison of the actually received signal by the sensor with the signal obtained in the case of the intact or reference structure. The situation when these signals are different can be caused by the presence of a flaw in the inspected plate. In order to estimate the magnitude of the change in the picked up signal, the linear correlation coefficient is introduced:

$$\lambda_{fg}^* = \frac{\sum\limits_{i=1}^{N} \left[(f_i - \mu_f)(g_i - \mu_g) \right]}{\sqrt{\sum\limits_{i=1}^{N} (f_i - \mu_f)^2} \sqrt{\sum\limits_{i=1}^{N} (g_i - \mu_g)^2}} \tag{1}$$

where N is a number of discrete values describing the compared signals; f_i, g_i denote the value of the reference and actual signals; and μ_f, μ_g are the average values computed for the signals f and g. Generally, the values of λ_{fg}^* belongs to the range $[1, -1]$. However, for identical signals, the coefficient $\lambda_{fg}^* = 1$, Further, the results obtained from the set of sensors should be normalized. Another disadvantage of this approach is that the coefficient λ_{fg}^* is very sensitive in the case when the actual signal is shifted in phase. On the other hand, the value of the λ_{fg}^* is quite insensitive to the reduction of the amplitude of the actual signal in comparison with the reference signal (without a change in phase). This fact could result in the process of damage identification being very difficult. In the next step, the appropriate damage index DI has to be defined [8]. Generally, this parameter should consist of two terms. The first term describes the qualitative or quantitative difference between the actual and reference signals. The second term defines the propagation path of the Lamb wave and assigns the computed value of the DI. In a two-dimensional case, the DI can be defined as follows:

$$DI(x,y) = (1 - \lambda_{fg}) \left(\frac{\beta - R(x,y,x_a,y_a,x_s,y_s)}{\beta - 1} \right) \tag{2}$$

$$R(x,y,x_a,y_a,x_s,y_s) = \begin{cases} R_c(x,y,x_a,y_a,x_s,y_s), & R_c(x,y,x_a,y_a,x_s,y_s) < \beta \\ \beta, & R_c(x,y,x_a,y_a,x_s,y_s) \geq \beta \end{cases} \tag{3}$$

$$R_c(x,y,x_a,y_a,x_s,y_s) = \frac{\sqrt{(x-x_a)^2 + (y-y_a)^2} + \sqrt{(x-x_s)^2 + (y-y_s)^2}}{\sqrt{(x_a-x_s)^2 + (y_a-y_s)^2}} \tag{4}$$

where λ_{fg} is the normalized correlation factor; x_a, y_a are the coordinates of the actuator; x_s, y_s are the coordinates of the sensor; x and y are the space coordinates (In other words they are the coordinates of the point, where the value of the DI is evaluated) and β is a parameter which determines the width of the propagation path. It is convenient to mark each propagation path as follows: A1- S1, A1 - S2, etc. Moreover, in cases a), b) and c), the line which links the position of the actuator and sensor goes through the cutout. Thus, in these cases, the coordinates of the actuator are changed. Now, it is the point where the line passing through the sensor is tangent to the edge of the hole. The modified propagation path is shown in Fig. 4. Having prepared the damage indexes for all possible propagation paths, the resultant value is evaluated according to the following formula:

$$DI^{RES}(x,y) = \sum_{k=1}^{M} DI(x,y)^{A_m - S_k} \tag{5}$$

where the superscript m denotes the considered case, i.e. a), b), c) or d) and S_k means the number of sensor in the array of sensors (Fig. 3). Finally the A_m - S_k describes the particular path shown in the Fig. 3. Finally, the additional path L^{ADD} is introduced. This path begins at the point which belongs to the edge of the hole and where the appearance of the crack is most likely. This path is oriented strictly in vertical direction. This is the
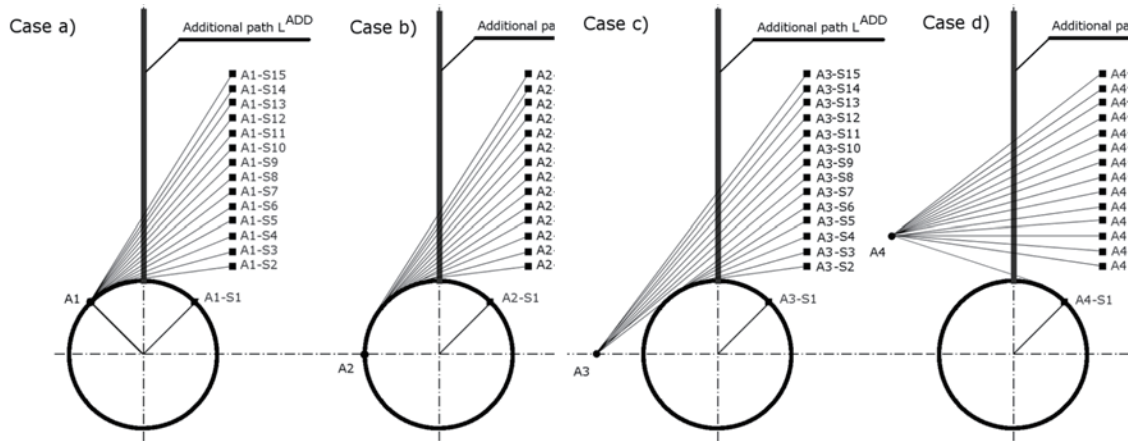
Fig. 4 The propagation paths and the additional path (expected crack direction)

expected direction of the damage evolution. Additionally, it is assumed that the value of the $DI = 1$. In order to estimate the crack length L^{CRK}, the following computation has to be carried out:

$$L^{CRK} = DI^{RES}(x,y) \cap L^{ADD} \tag{6}$$

Further, it is convenient to introduce a threshold value α. If the value of the parameter L^{CRK} is greater then α, the $L^{CRK} = 1$, otherwise $L^{CRK} = 0$. The last substitution allows precise estimation of the crack length. The main idea of the described algorithm for the discussed cases is depicted in Fig. 4.

5 Finite element model

The mesh size strongly depends on the excited signal and the length of the propagating wave. Due to the assumed level of simplicity of the numerical simulation, it is assumed that the wave is excited by the point force (normal to the surface of the plate) acting in the selected node. Therefore, it can be considered that only the antisymmetric mode S_0 of the Lamb wave is excited. The input signal is described by the following equation:

$$F(t) = \begin{cases} \dfrac{1}{2}F_0[1 - \cos(\dfrac{2\pi f_0 t}{n_0})]\cos(2\pi f_0 t), & t \le \dfrac{n_0}{f_0} \\[2ex] 0, & t > \dfrac{n_0}{f_0} \end{cases} \tag{7}$$

where $F_0 = 1[N]$ is the amplitude of the applied force, $f_0 = 250$ [kHz] is the frequency, and $n_0 = 5$ is the number of wave cycles. The wave speed in the studied plate can be estimated as follows:

$$v_{wave} = \sqrt{\dfrac{E}{\rho}} \tag{8}$$

Now it can be calculated that the wave length $\lambda = 20.294$ [mm]. It is worth stressing here that the chosen frequency f_0 of the excited signal causes the wave length λ to be much shorter than the shortest distance between the actuator and the sensor. It is very convenient when the picked up signal has to be interpreted as the incident or reflected wave. It is well known that in order to obtain reasonable results of the FE simulation there should be more than about 10 nodes per wave length. Therefore, it is assumed that the approximate element size $l_e \approx 2$ [mm] as a parameter of the automatic mesh generator. The simulations are carried out with the use of the commercial FE system ANSYS 12.1. The analyzed plate is considered as a shell structure. Thus, the standard
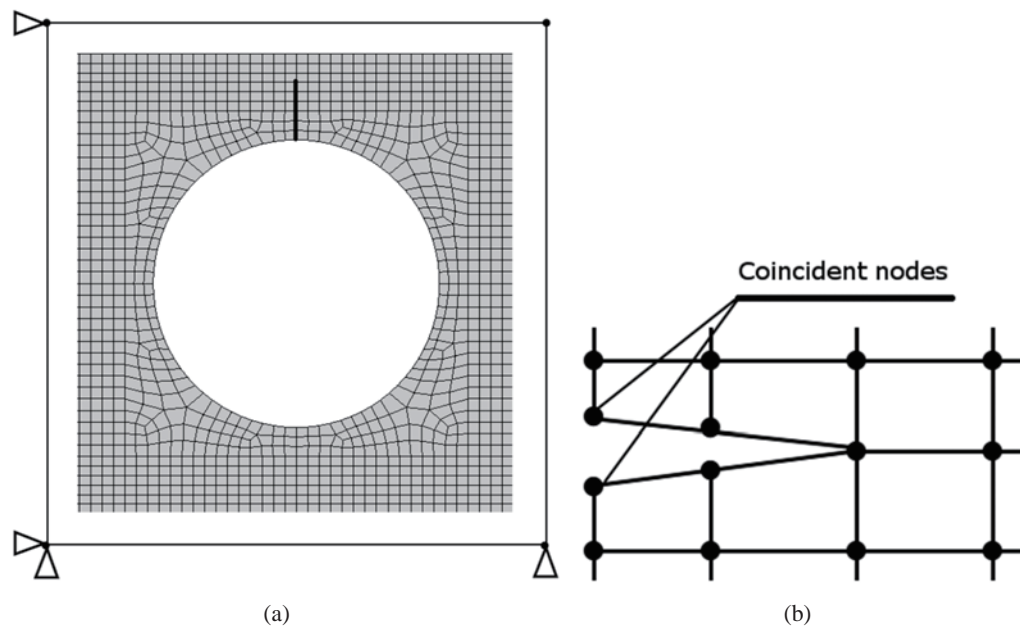
(a)   (b)

Fig. 5 Part of finite element mesh (a) and method of the crack modeling by the coincident nodes (b)

SHELL281 element is applied. This element has a quadratic shape function (higher order element) and in each node has 6 degrees of freedom: 3 transitional and 3 rotational ones. The element stiffness matrix is defined according to the first order shear deformation theory. The generated mesh consists of square-shape elements. Generally, the mesh is regular. However, in the vicinity of the cutout the mesh is irregular. In the Fig. 5 there is shown the part of FE mesh in the vicinity of the hole. The mesh consists of 16852 shell elements. The crack is modelled by the introduction of the coincident nodes. In other words, the nodes which belong to the crack are duplicated and their positions overlap each other. The idea of this approach is presented in Fig. 5. The plate is supported in the corners, as shown in Fig. 5, which makes the rigid motion of the structure impossible. Additionally, in all four corners, the possibility of motion in the direction perpendicular to the surface of the plate is also constrained.

6 Results and discussion

In the Fig. 6 there are shown four exemplary snapshots, which represent the wave propagation in the case a), where the wave is activated by the piezoelectric element A1. As it can be observed the existence of the crack of the length $l_c = 5$ [mm] significantly change the propagation of the elastic wave. It seems that the proposed location of the sensor array should be able to detect even small differences between signals received in the case of intact and damaged structure. It should be stressed here that the reflection from the crack of the incident signal can also be observed. Thus it seems that tin is possible to design the SHM system, which is based on the detection of the reflected from the crack signals. In that case the information about intact structure is not necessary. In the other hand it can be very difficult to detect the reflected signal because of a noise, which is present in the case of real structure. Moreover, the evaluation of the crack length could be also very difficult. A comparison of the received signals recorded by sensors S2, S5, S8, and S11 for intact and damaged structures is shown in Fig. 7. The numerical simulation is carried out in case a), where the assumed crack length is equal to $l_c = 10$ [mm] (Fig.4a). In other studied cases, the results of the numerical simulation are similar. It is worth stressing that the presence of the crack causes mainly the reduction of the amplitude of the received signal. Moreover, the signal obtained for the damaged structure is shifted in phase in comparison with the intact structure. The change
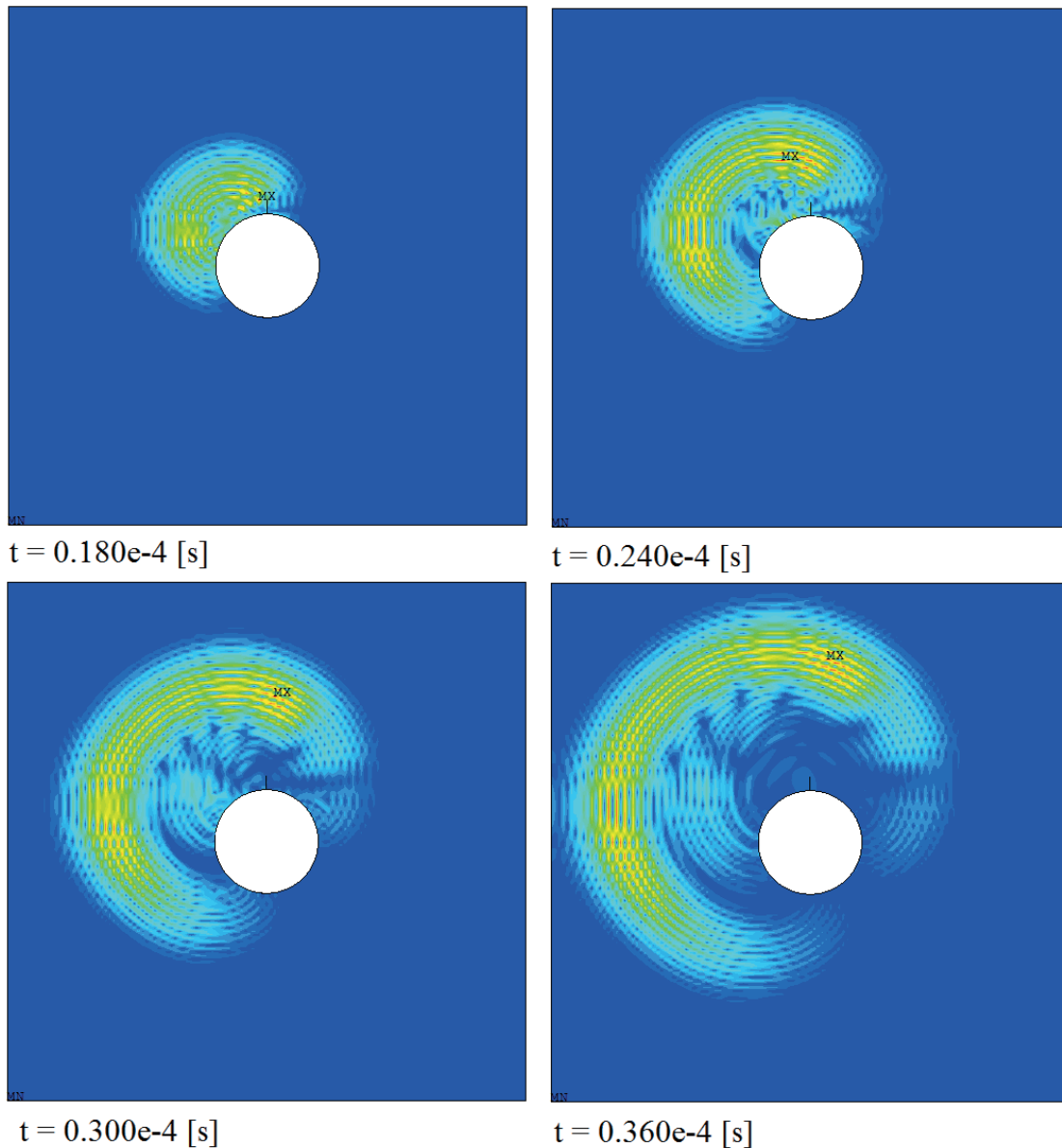
t = 0.180e-4 [s]   t = 0.240e-4 [s]

t = 0.300e-4 [s]   t = 0.360e-4 [s]

Fig. 6 Numerical simulation of elastic wave propagation in the case a).

of phase is significant in the cases when the propagation path goes through the crack. For other propagation paths, the reduction of the amplitude is mainly observed. The use of Fourier's transformation (not presented in this paper) shows that the frequencies of the analyzed signals are almost identical. In other words, the existence of the damage does not change the frequency of the applied signal. It should also be stressed that the main disadvantage of the linear correlation coefficient (1) is that it is very sensitive to the change of the phase in contrast to the reduction of the amplitude. Therefore, comparison of the signals recorded for the intact and damaged structures may not be quite effective. Fig. 7 also presents normalized values of the linear correlation coefficient. In this particular case the obtained values of λ_{fg} differ significantly for sensors S2 - S7. However, the values of λ_{fg}, computed for sensors S8 - S15 are close to unity $\lambda_{fg} \approx 1$. Thus, this fact could be used to evaluate the actual length of the crack. In the Fig. 8 and Fig. 9 there are depicted the results of using the Eq. (5) and (6) in the case a) for the crack length equal to $l_c = 5, 10$ and *15 [mm]*. In the case of relation (5) the board disturbance is observed.
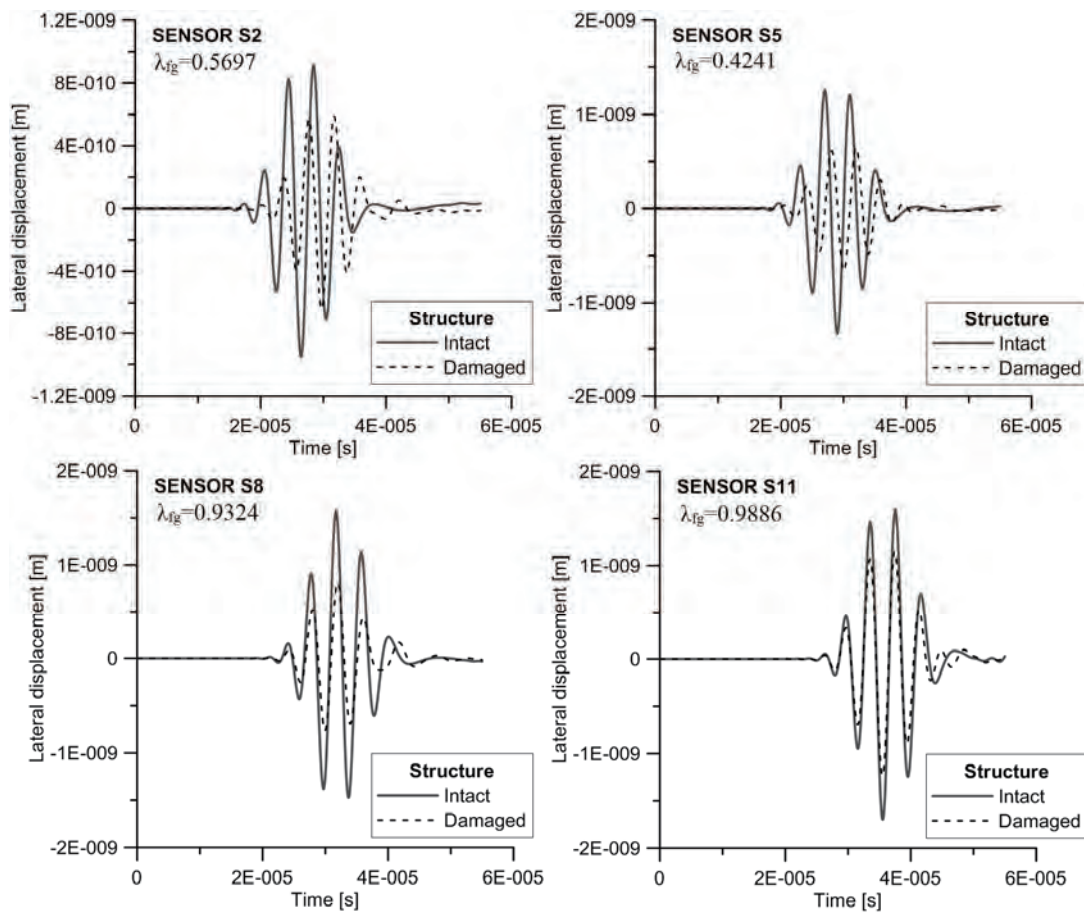
Fig. 7 Registered signals for intact and damaged structures, sensors S2, S5, S8, S11 in the case a)
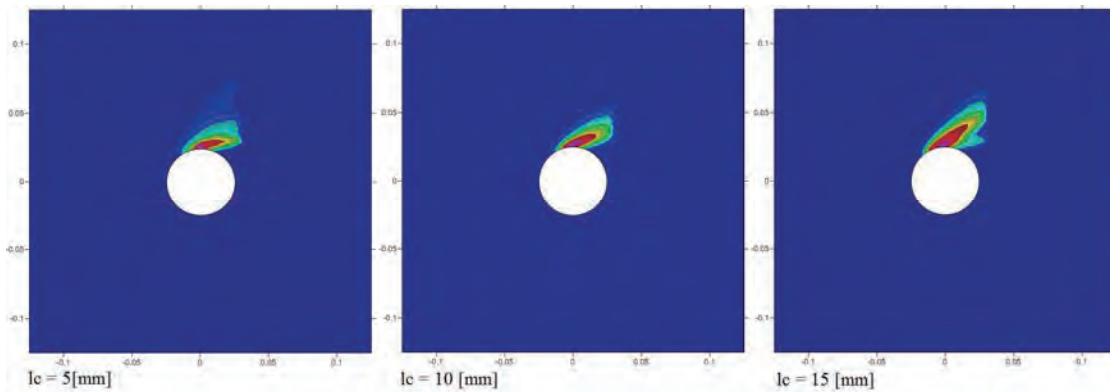
Fig. 8 Distribution of damage index, Eq. 5 in the case a)

The size of these disturbances corresponds to the crack length. However, on this stage of the proposed method the precise evaluation of the crack length is rather impossible. When the further step is applied, clear location and size of the detected crack is visible (Fig. 9).

Now, the question arises, where is the most effective position of the actuator. In order to find the answer to this question, four different locations of the actuator are studied as it is presented in Fig. 4. The results obtained with the use of the algorithm discussed in Section 4 of this paper are presented in Fig. 10. The normalized values of the relation (6) along the additional path L^{ADD} are also shown in Fig.10. The origin of the global coordinate

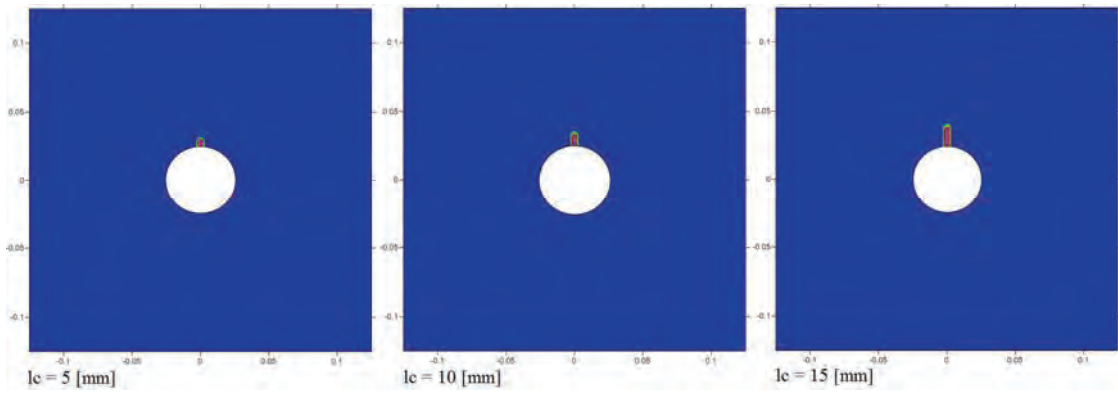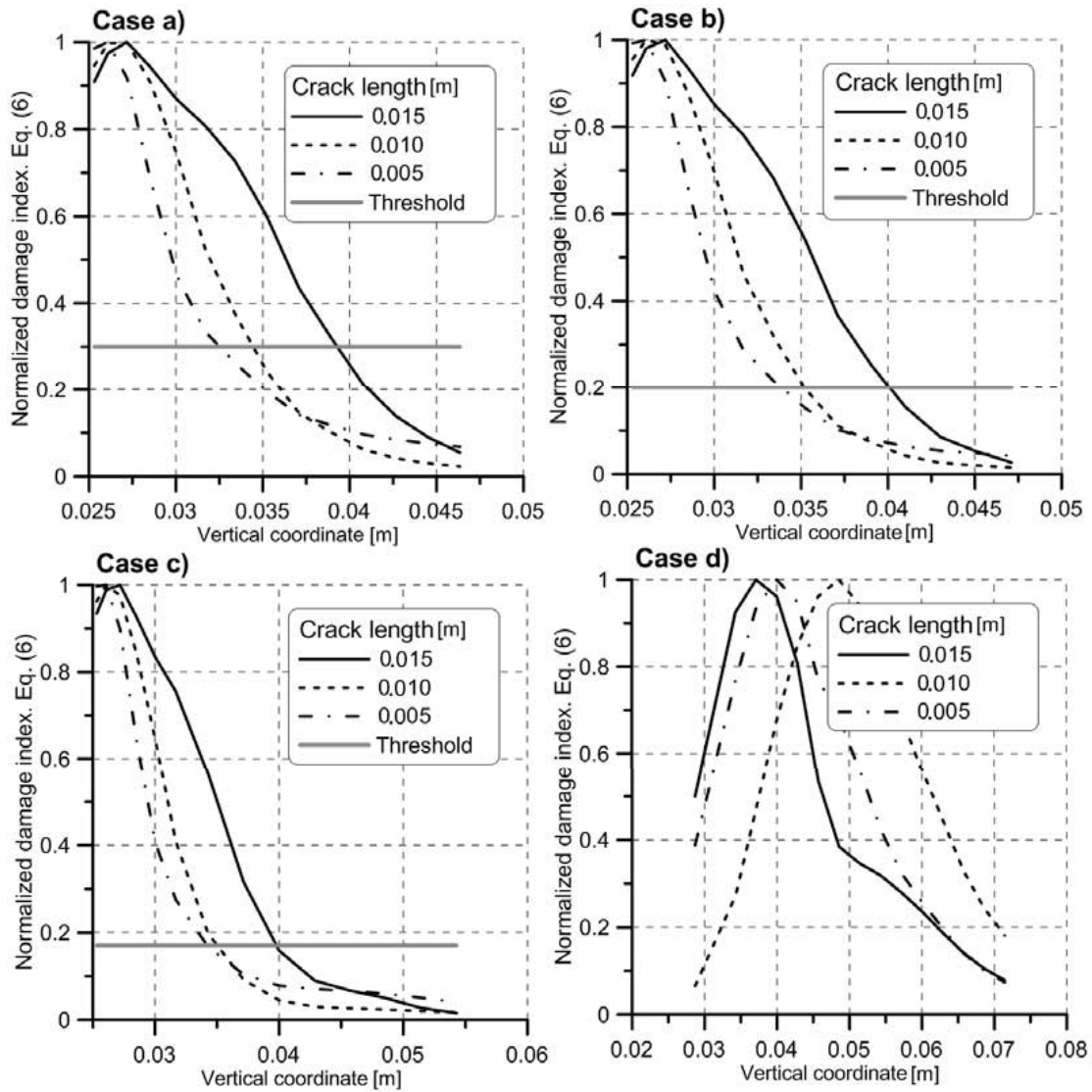**Fig. 9** Estimated crack length with the use of Eq. 6 in the case a).

Fig. 10 Values of Eq. 6 with thresholds along additional path L^{ADD} in the case a), b), c) and d).

system is in the geometrical center of the studied plate. The intersection point of the edge of the hole and the additional path L^{ADD} has a vertical coordinate $y = 250$ [mm]. For example, the crack tip of the length $l_c = 5[mm]$ has vertical coordinate $y = 300$ [m]. The discussed graphs also present the optimal values of the threshold α in particular cases. It seems that in case a) the obtained results are most reasonable. For the threshold $\alpha = 0.3$, the length of the longer crack ($l_c = 10$ [mm], 15 [mm]) is precisely estimated. However, in the case of the smaller crack $l_c < 5$ [mm], the length of the crack is overestimated. In case b), although the value of the threshold is different, i.e. $\alpha = 0.2$, the overestimation of the length of the small crack is more significant. The same effect can be observed in case c), where $\alpha = 0.17$. In contrast to the previous results, the curves which can be observed in case d) seem to be useless. Therefore, it is impossible to estimate the length of the crack taking into account the results obtained in case d).

7 Conclusions

The authors of the paper look for the most effective position of the actuator. Four different positions are studied. The most reasonable estimation of the crack length is obtained when the actuators are placed on the edge of the circular hole - cases a) and b). If the actuators are installed in some distance from the edge, the estimation of the damage size is inaccurate or even impossible. The main disadvantage of the studied approach is connected with the use of the linear correlation coefficient, which is very sensitive to the change of phase of the compared signals. The reduction of the amplitude does not cause significant variations of the linear correlation coefficient. It is very important since both effects are observed in performed numerical simulations.

References

[1] Rytter, A. (1993), Vibration based inspection of civil engineering structures, Ph.D. Dissertation, Department of Building Technology and Structural Engineering/ Aalborg University, Denmark.
[2] Park, G., Muntges, D.E., and Inman, D.J. (2001), Self-Monitoring and Self-Healing Jointed Structures, Damage Assessment of Structures, *Key Engineering Materials*, **204-205**, 75-84.
[3] Achenbach, J.D. (1984), Wave propagation in elastic solids, North-Holland Publ. Co., New York.
[4] Rose, J.L., (1999), Ultrasonic waves in solid media, Cambridge University Press.
[5] Viktorov, A. (1967), Rayleigh and Lamb waves - physical theory and applications, Plenum Press, New York.
[6] Lamb, H. (1917), On waves in an elastic plate, *Proceedings of the Royal Society, A Mathematical, Physical and Engineering Sciences*, **93**, 114-128.
[7] Lord, R. (1885), On Waves Propagated along the Plane Surface of an Elastic Solid, *Proceedings of the London Mathematical Society*, **s1-17**(1), 4-11.
[8] Su, Z. and Ye, L. (2009), Identification of damage using Lamb waves, Springer.
[9] Rose, J.L. and Avioli, M.J. (2000), Elastic waves analysis for broken rail detection, 15th World Conference on Non-Destructive Testing, Rome.
[10] Haig, A.G., Mudge, P., and Balachandran, W. (2008), *Advanced* transducer development for long range ultrasonic inspection systems, Proceedings of the 4th International Conference on Emerging Technologies in Non-Destructive Testing, 79-82.
[11] Li, J. and Rose, J.L. (2001), Excitation and propagation of non-axisymmetric guided waves in a hollow cylinder, *Journal of Acoustical Society of America*, **109**, 457-464.
[12] Diamanti, K. and Soutis, C. (2010), Structural health monitoring techniques for aircraft composite structures, *Progress in Aerospace Sciences*, **46**(8), 342-352.
[13] Hedl, R., Finda, J., and Parthasarathy, G. (2011), Advanced approach for multi-site damage monitoring on aircraft fuselage panel using sparse PZT actuator/sensor arrays, Structural Health Monitoring, *Condition Based Maintenance and Intelligent Structure - Proceedings of the 8th International Workshop on Structural Health Monitoring*, **1**, 643-650.
[14] Saravanos, D.A. and Heyliger, P.R. (1995), Coupled layerwise analysis of composite beams with embedded piezoelectric sensors and actuartors, *Journal of Intelligent Material Systems and Structures*, **6**, 350 - 362.
[15] Saravanos, D.A., Birman,V. and Hopkins, D.A. (1994), Detection of delamination in composite beams using piezoelectric sensors, *Proceedings of the 35th Structures, Structural Dynamics and Materials Conference of the AIAA*.
[16] Wu, T.T. and Liu, Y.H. (1999), On the measurement of anisotropic elastic constants of fiber-reinforced composite plate using ultrasonic bulk wave and laser generated Lamb wave, *Ultrasonics*, **37**(6), 405-412.

[17] Moreno, E. and Acevedo, P. (1998), Thickness measurement in composite materials using Lamb waves, *Ultrasonics*, **35**, 581-586.

[18] Grondel, S., Assad, J., Delebarre, C., Blanquet, P., and Moulin E. (1999), The propagation of lamb waves in multilayered plates: phase velocity measurement, *Measurement Science and Technology*, **10**(5), 348-353.

[19] Chang, Z. and Mal, A. (1999), Scattering of Lamb waves from a rivet hole with edge cracks, *Mechanics of Materials*, **31**, 197-204.

[20] Fromme, P. and Sayir, M.B. (2002), Detection of cracks at rivet holes using guided waves, *Ultrasonics* **40**, 199-203.

[21] Grahn, T. (2003), Lamb wave scattering from a circular partly through-thickness hole in a plate, *Wave Motion*, **37**, 63-80.

[22] Hong, M., Su, Z., Lu, Y., Sohn H., and Qing X. (2015), Locating fatigue damage using temporal signal features of nonlinear Lamb waves, *Mechanical Systems and Signal Processing*, **60-61**, 182-197.

[23] McKeon, J.C.P. and Hinders, M.K. (1999), Lamb wave scattering from a through hole, *Journal of Sound and Vibration*, **224**(5), 843-862.

[24] Barski, M., Stawiarski, A., and Pają, P. (2015), Numerical study of the optimal position of a Lamb wave actuator for detection of fatigue damage in an isotropic plate with a circular hole, Dynamical Systems, Mathematical and Numerical Approaches, Eds.: Awrejcewicz J., Kaźierczak M., Mrozowski J., Olejnik, 69-80.

[25] Stawiarski, A., Barski, M., and Pają, P. (2015), Fatigue crack identyfication by dynamic analysis of elastic waves propagation, Dynamical Systems, Mathematical and Numerical Approaches, Eds.: Awrajcewicz J., Kaźierczak M., Mrozowski J., Olejnik, 489-500.

Free Vibrations of Cantilever Bars with Linear and Nonlinear Variable Cross-Section

Jacek Jaworski[†], Olga Szlachetka

Department of Civil Engineering, Faculty of Civil and Environmental Engineering, Warsaw University of Life Sciences - SGGW, Nowoursynowska 166, 02-787 Warsaw, Poland

Abstract

The topic of this study is the first mode of natural transverse vibrations of isotropic, homogeneous and elastic bars (columns or beams) with clamped bottom and free head. The columns of the first group are shaped as truncated solid cones or as tubes with linearly variable wall thickness and with different inclination of lateral faces, from cylinder to cone. The columns of the second group were shaped in similar way, but the generatrices of the solids of revolution were curvilinear – in the shape of a parabola. The first frequency of free vibrations was determined using the Rayleigh method. The deflection line of the column axis during the vibration was assumed in form of the bending line of the column axis subjected to a uniform load. Resulting frequencies (or periods) were compared with these obtained with the use of FEM (ANSYS) and a good compliance of results was observed. As the expression for the energy of an elementary slice of material was integrated over the length of the rod, the formula for the frequency was obtained in form of an integral equation. In some cases an exact solution of integral equation was obtained, however in other cases only a numerical solution was possible.

1 Introduction

The frequencies of subsequent modes of free vibrations of a beam can be obtained by solving the equation of a Bernoulli-Euler beam for specific boundary conditions. Many authors solved this equation for beams with variable cross-section. For truncated cone and wedge beams, Conway and Dubil [1] obtained a solution in the form of the Bessel functions of the second order. Latterly, the natural frequencies of a truncated cone were also analysed by Coşkun et al. [2] (application of three different analytical approximate techniques) as well as Abdelghany et al. [3] (differential transformation method). There are solutions concerning special cases of hollow cones too, cf. Suppiger [4], Kang and Leissa [5]. Wu and Chiang [6] considered a simple task when the generatrices of the internal and external cone cross in a point on the cones' axis. Many papers concern beams with rectangular cross-section when one of the rectangle sides has a constant value and the second one varies according a given function, for example a linear, exponential or parabolic function. For beams with rectangular cross-section with the one side of a constant value and the second one linearly varying, Datta and Sil [7] obtained

---

[†]Corresponding author.
Email address: jacek_jaworski@sggw.pl

a solution in the form of the Bessel functions, Naguleswaran [8, 9] applied the Frobenius method. Ece et al. [10] analysed a bar having a constant thickness and exponentially varying width. Caruntu [11] investigated a bar with a constant width and parabolically varying thickness, using the Jacobi polynomials. Zhou and Cheng [12] analysed free vibrations of double tapered parabolic beams using the Rayleigh-Ritz method. Many authors analysed other cases of beams with variable cross-sections, e.g. Abrate [13] (the Rayleigh-Ritz method), Guo and Yang [14] (a method leading to a solution in the form of series), Firouz-Abadi et al. [15] (Wentzel-Kramers-Brillouin approximation). Caruntu [16] submitted the exact analytical solution for natural frequencies of a bar with circular cross-section, parabolic variability of radius and sharp end. The parabola was convex in relation to the cone longitudinal axis.

Thus, the determination of natural frequencies of hollow bars with variable cross-sections, especially having a shape of curvilinear truncated cone (cone tube) with hollows of different shapes, is still an actual problem. For many cases of curvilinear cones, e.g. parabolic, the authors did not find in the literature exact results which could serve as a benchmark for approximated solutions.

For cantilever constructions, such as towers or posts, a determination of a construction susceptibility to dynamic influences of wind is a part of calculations of wind load; in this aim, the natural frequency of the construction must be calculated. Here the first natural frequency of transverse vibrations is crucial. The authors, using the approximated Rayleigh's method, submitted an easy way to determine the first frequency of transverse vibrations of cantilever bars. Using the Rayleigh's quotient [17], the formulas for the first frequency of free (transverse) vibrations of cantilever bars having the shape of solids of revolution (solid truncated cone and hollow truncated cone, i.e. coaxially hollowed truncated cone) with parabolic curvilinear generatrices have been derived. Hereinafter, in this paper, such bars will be called parabolic truncated cone – solid or hollow. Comparing the obtained results to data from the literature, it has been stated for the example of a truncated cone that the accuracy equals $0.5 \div 1\%$, what is absolutely sufficient for engineering calculations. The obtained results for solid and hollow parabolic cones were compared to those achieved in FEM and those obtained for the solid and hollow truncated cone with linear generatrices, with the use of the formulas derived in [18] and [19], respectively.

The Rayleigh's method is approximated because requires to assume *a priori* a shape of the axis of a vibrating post. The deflection line of the bar axis during the vibration was assumed in form of the bending line of the bar axis subjected to a uniform load. Besides, it is assumed that the amplitude of the vibrations is small, the material is homogeneous, isotropic and ideally elastic, the bars are slender and the mass is distributed continuously. The assumption of the continuous mass distribution leads sometimes to severe difficulties during integration. However, if an exact solution can be found, as e.g. for a truncated-cone cantilever bar [18], the obtained formula is so simple that a pocket calculator is enough to calculate the first frequency (or period) of free vibrations. In the case of a hollow truncated cone with linear generatrices, the solution of some integrals needs to use numerical methods. In the case of parabolic solid and hollow truncated cones it is convenient to carry out calculations in a computer environment – the authors applied the Mathematica.

2 Hollow truncated cone post

2.1 General solution

The considerations concern free vibrations of a cantilever bar with the shape of hollow truncated cone with linear generatrices, the bar subjected to a continuous load having a constant value q (Fig. 1). The following denotations have been introduced

$$\eta = \frac{D}{d}, \tag{1}$$
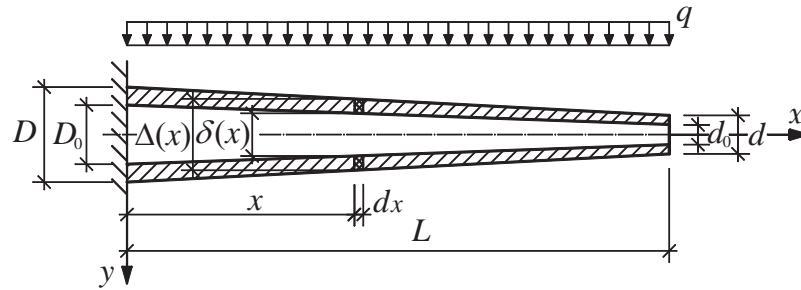
$$\alpha = \frac{D_0}{D}, \tag{2}$$

Fig. 1 Cantilever beam in form of a uniformly loaded hollow cone tube [19].

$$\beta = \frac{d_0}{d}. \tag{3}$$

The external and internal diameter of the bar as well as the second area moment in any cross section, given by a coordinate x, equal respectively

$$\Delta(x) = D - \frac{D-d}{L}x, \tag{4}$$

$$\delta(x) = D_0 - \frac{D_0 - d_0}{L}x, \tag{5}$$

$$J(x) = \frac{\pi}{64}\left[\Delta^4(x) - \delta^4(x)\right], \tag{6}$$

where x, y – coordinate axes, D, d – bigger and smaller external diameter of the bar, D_0, d_0 – bigger and smaller internal diameter of the bar, η – quotient of the diameters describing a convergence ratio of external walls of the truncated cone, L – bar length, J – second area moment of the bar cross section.

A deflection has been calculated by integration of the differential equation of bar elastic deflection curve

$$EJ(x)\frac{d^2u(x)}{dx^2} = -M(x) = \frac{qL^2}{2} - qLx + \frac{qx^2}{2}, \tag{7}$$

where $u(x)$ – deflection, E – longitudinal modulus of elasticity, M– bending moment in the bar section given by a coordinate x, q – continuous load of a constant value.

Equation (7) has been rewritten to a more convenient form, then decomposed in partial fractions

$$\frac{\pi E D^4}{32q}\frac{d^2u(x)}{dx^2} = \frac{L^2 - 2Lx + x^2}{(ax+b)(cx+e)(rx^2+sx+h)} = \frac{\alpha_1}{ax+b} + \frac{\alpha_2}{cx+e} + \frac{\beta_1 x + \beta_2}{rx^2+sx+h} \tag{8}$$

and integrated twice, so the bar deflection line has been obtained as

$$u(x) = \frac{32q}{\pi E D^4}P(x), \tag{9}$$

where $P(x)$ is a function of the geometrical parameters of the post and is expressed in a form

$$\begin{aligned}
P(x) =\ & C_1 x + C_2 + \frac{\alpha_1}{a^2}(ax+b)\left[\ln(ax+b) - 1\right] + \frac{\alpha_2}{c^2}(cx+e)\left[\ln(cx+e) - 1\right] \\
& -\frac{\beta_1 x}{r} + \frac{\beta_1(rx+s) - \beta_2 r}{2r^2}\ln(rx^2+sx+h) \\
& +\left[\frac{\beta_1\sqrt{4rh-s^2}}{2r^2} + (\beta_2 - \frac{\beta_1 s}{2r})\frac{2rx+s}{f\sqrt{4rh-s^2}}\right]\arctan\frac{2rx+s}{\sqrt{4rh-s^2}}
\end{aligned} \tag{10}$$

whereas integration constants C_1 and C_2 equal, respectively

$$C_1 = -\frac{\alpha_1}{a}\ln b - \frac{\alpha_2}{c}\ln e - \frac{\beta_1 x}{2r}\ln h - \left(\beta_2 - \frac{b_1 s}{2r}\right)\frac{2}{\sqrt{4rh - s^2}}\arctan\frac{s}{\sqrt{4rh - s^2}},$$

$$C_2 = -\frac{\alpha_1 b}{a^2}(\ln b - 1) - \frac{\alpha_2 e}{c^2}(\ln e - 1) - \frac{\beta_1 g - \beta_2 r}{2r^2}\ln h+ \tag{11}$$

$$-\left[\frac{\beta_1\sqrt{4rh - s^2}}{2r^2} + \left(\beta_2 - \frac{b_1 s}{2r}\right)\frac{s}{f\sqrt{4rh - s^2}}\right]\arctan\frac{s}{\sqrt{4rh - s^2}}$$

and the parameters, appearing in Eqs. (10) and (11), are described by the formulas

$$a = -\frac{\eta(1 - \alpha) - (1 - \beta)}{\eta L},$$

$$b = 1 - \alpha,$$

$$c = -\frac{\eta(1 + \alpha) - (1 + \beta)}{\eta L},$$

$$e = 1 + \alpha, \tag{12}$$

$$r = \frac{\eta^2(1 + \alpha^2) - 2\eta(1 + \alpha\beta) + (1 + \beta^2)}{\eta^2 L^2},$$

$$s = -\frac{2}{\eta L}\left[(1 + \alpha^4)\,\eta - (1 + \alpha\beta)\right],$$

$$h = 1 + \alpha^2.$$

Symbols α_1, α_2, β_1, β_2 are the quotients of the determinants

$$\alpha_1 = \frac{W_{\alpha_1}}{W}; \quad \alpha_2 = \frac{W_{\alpha_2}}{W}; \quad \beta_1 = \frac{W_{\beta_1}}{W}; \quad \beta_2 = \frac{W_{\beta_2}}{W} \tag{13}$$

and these determinants are obtained with the Cramer's method applied to solve the set of Eqs. (14). The determinants (13) arose as an effect of a comparison of two expressions of the right side of Eq. (8).

$$\alpha_1 cr + \alpha_2 ar + \beta_1 ac = 0,$$

$$\alpha_1(er + cs) + \alpha_2(br + as) + \beta_1(ae + bc) + \beta_2 ac = 1,$$

$$\alpha_1(es + ch) + \alpha_2(bs + ah) + \beta_1 be + \beta_2(ae + bc) = -2L, \tag{14}$$

$$\alpha_1 eh + \alpha_2 bh + \beta_2 be = L^2.$$

Assuming that the bar axis (Fig. 1) deflected during vibrations has a shape described by Eq. (9), the potential energy in a deflected position and the kinetic energy in the position of equilibrium have been calculated. The comparison of the energies yields a vibration frequency. The vibration period is equal to

$$T = \frac{2\pi}{\omega} = \frac{4\pi}{D}\sqrt{\frac{2\rho}{E}}\sqrt{\frac{\int_0^L (ax + b)(cx + e)P^2(x)\,dx}{\int_0^L P(x)\,dx}} \tag{15}$$

where T – vibration period, ω – vibration frequency, ρ – mass density, a, b, c, e – according to the Eq. (12).

Expansion of the terms in the integrals in the root in Eq. (15) yields i.a. the integrals in the form

$$x^3\ln(ax + b)\arctan(cx + e),$$

$$x^3\ln(ex^2 + rx + g)\arctan(cx + e). \tag{16}$$

These functions are not integrable analytically, therefore the values in Eq. (15) have been calculated numerically with the use of the Mathematica.
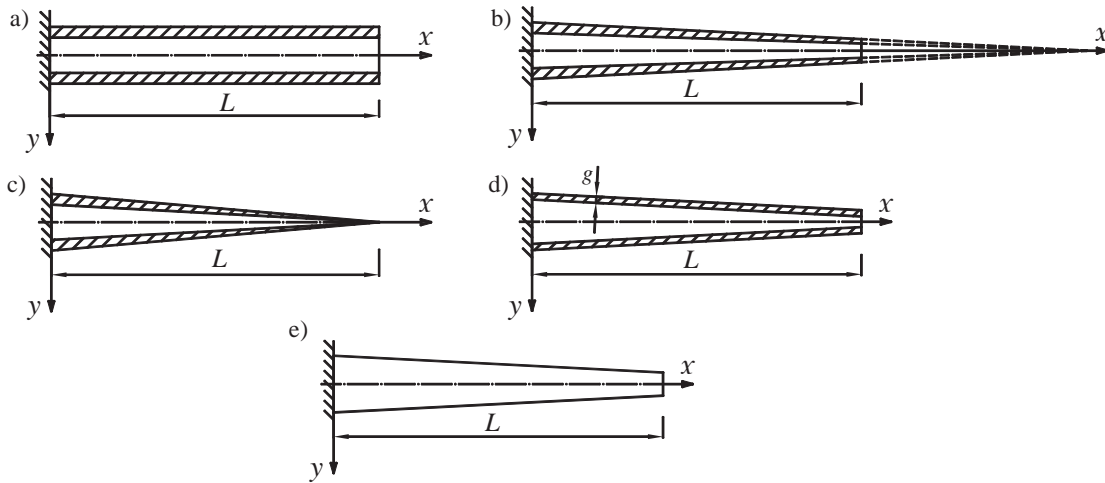
Fig. 2 Special cases: a) cylindrical tube, b) hollow truncated cone (conical tube), $\alpha = \beta$, c) hollow cone, d) conical tube with constant wall thickness, e) truncated cone.

2.2 Special cases

As the denominators in the formulas applied for transformations cannot equal zero, the four special cases presented in Fig. 2a-2d must be considered individually. The formulas for calculation of the vibration period for them are given in [19].

As a special case for $D_0 = 0$ and $d_0 = 0$, a solid truncated cone can be treated (Fig. 2e), for which the analytical solution of the integrals has been obtained [18] and the ultimate form of the solution can be presented as in Eq. (17), where the terms $A(\eta), B(\eta), C(\eta)$ are described by Eqs. (18)

$$T = \frac{4\pi L^2}{3D} \frac{\eta}{(\eta-1)^2} \sqrt{\frac{\rho}{E}} \sqrt{\frac{A(\eta) + 60B(\eta) \ln \eta}{10C(\eta)}} \tag{17}$$

$$
\begin{aligned}
A(\eta) &= 11\eta^6 - 87\eta^5 + 375\eta^4 - 1184\eta^3 + 3219\eta^2 - 4281\eta + 2817 - 1080\eta^{-1} + 234\eta^{-2} - 24\eta^{-3}, \\
B(\eta) &= 14\eta^3 - 33\eta^2 + 15\eta - 3 - 6\eta^3 \ln\eta, \\
C(\eta) &= 3\eta^4 + 10\eta^3 - 18\eta^2 + 6\eta - 1 - 12\eta^3 \ln\eta.
\end{aligned}
\tag{18}
$$

3 Parabolic solid truncated cone shape post

3.1 Beam deflection

Let us consider a solid of revolution having the shape of a curvilinear truncated cone (Fig. 3) whose generatrices are parabolas described by Eq. (19) which is a dependence of the post diameter in any cross section of the bar on the coordinate x. The substitution (20) has been applied and the second area moment is described by Eq. (21).

$$\Delta(x) = D\left(1 - \frac{\eta-1}{\eta}\sqrt{\frac{x}{L}}\right) = \frac{D}{k}(k - \sqrt{x}), \tag{19}$$

$$k = \frac{\eta\sqrt{L}}{\eta-1}, \tag{20}$$

$$J(x) = \frac{\pi\Delta^4(x)}{64} = \frac{\pi D^4}{64k^4}(k - \sqrt{x})^4. \tag{21}$$
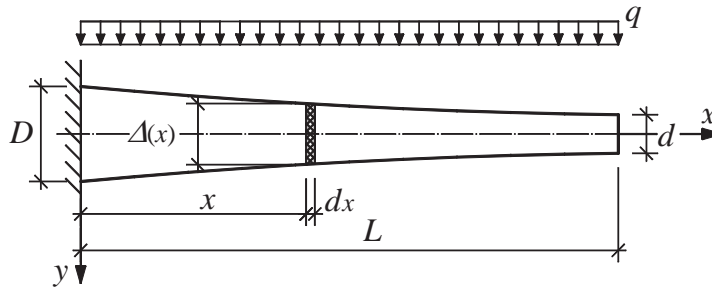
Fig. 3 Parabolic truncated cone shape cantilever bar, uniformly loaded.

The differential equation of a deflected neutral axis of the uniformly loaded bar has the form given in Eq. (7). After substitution of the second area moment (21) and taking the dependence (20) into consideration, an equation has been obtained

$$\frac{\pi E D^4}{32 q k^4} \frac{d^2 u(x)}{dx^2} = \frac{x^2 - 2Lx + L^2}{(k - \sqrt{x})^4}. \tag{22}$$

The integration by substitution and simplification yields

$$\frac{\pi E D^4}{32 q k^4} u(x) = S(x) \tag{23}$$

where

$$\begin{aligned}
S(x) =& C_1 x + C_2 + \frac{2}{3} \frac{k^2 (k^2 - L)^2}{(k - \sqrt{x})^2} - \frac{2k (17k^4 - 22k^2 L + 5L^2)}{3 (k - \sqrt{x})} + \frac{x^2}{2} + \frac{16}{3} k x^{\frac{3}{2}} \\
& - 2 \left[35k^4 - 20k^2 L + L^2 - 2x (5k^2 - L) \right] \ln (k - \sqrt{x}) - x (19k^2 - 2L) \\
& + 2k\sqrt{x} (14L - 30k^2) + 70k^4 - 30k^2 L
\end{aligned} \tag{24}$$

and integration constants C_1 and C_2 can be expressed as

$$C_1 = \frac{13k^4 - 14k^2 L + L^2}{3k^2} - 11k^2 + 12L - 4 (5k^2 - L) \ln k, \tag{25}$$

$$C_2 = 2 (35k^4 - 20k^2 L + L^2) \ln k - \frac{2}{3} (89k^4 - 25k^2 L - 4L^2). \tag{26}$$

3.2 Vibration period

Assuming that the axis of the post, deflected as a result of vibrations, has the shape described by Eq. (23), the potential energy in the deflected position and the kinetic energy in the non-deflected position can be calculated. The potential energy equals

$$E_p = \int_0^L \frac{1}{2} q u(x) \, dx = \frac{1}{2} \frac{32 q^2 k^4}{\pi E D^4} \int_0^L S(x) \, dx. \tag{27}$$

If the mass of a material slice with a thickness dx is denoted as $m(x)$, i.e.

$$dm(x) = \frac{\rho \pi \Delta^2(x)}{4} dx = \frac{\rho \pi D^2}{4k^2} (k - \sqrt{x})^2 \, dx \tag{28}$$

then the kinetic energy of the post is determined as

$$E_k = \int_0^L \frac{1}{2} \omega^2 u^2(x) \, dm(x) = \frac{1}{2} \omega^2 \frac{\rho \pi D^2}{4k^2} \left(\frac{32 q k^4}{\pi E D^4} \right)^2 \int_0^L (k - \sqrt{x})^2 S^2(x) \, dx. \tag{29}$$
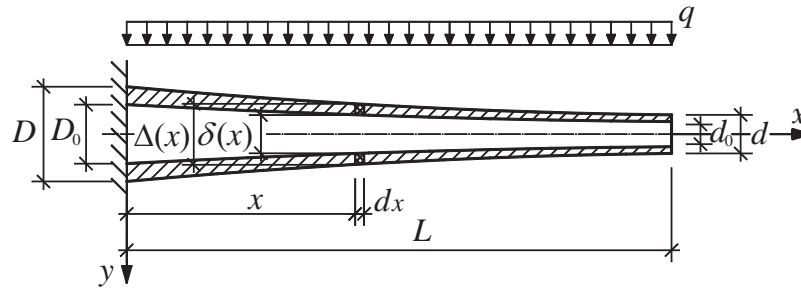
Fig. 4 Parabolic hollow truncated cone shape cantilever bar, uniformly loaded.

The energy comparison enables to determine the frequency. The period equals

$$T = \frac{2\pi}{\omega} = \frac{4\pi k}{D} \sqrt{\frac{2\rho}{E}} \sqrt{\frac{\int_0^L (k - \sqrt{x})^2 S^2(x)\, dx}{\int_0^L S(x)\, dx}} \tag{30}$$

where k, $S(x)$ – according to the Eqs. (20) and (24).

4 Parabolic hollow truncated cone shape post

Figure 4 presents a curvilinear solid of revolution (hollow cone) where the generatrices of the external and internal wall are parabolas. The external and internal diameters on a height determined by a coordinate x are described by Eqs. (19) and (31), respectively, and the parameters k and l – by Eqs. (20) and (32).

$$\delta(x) = D_0(1 - \frac{\mu - 1}{\mu}\sqrt{\frac{x}{L}}) = \frac{D_0}{l}(l - \sqrt{x}), \tag{31}$$

$$l = \frac{\mu\sqrt{L}}{\mu - 1}. \tag{32}$$

The denotations applied here comply with those in Eqs. (1), (2) and (3) and the quotient of the internal diameters is denoted as

$$\mu = \frac{D_0}{d_0}. \tag{33}$$

The second area moment is described by the equation

$$J(x) = \frac{\pi\Delta^4(x)}{64} - \frac{\pi\delta^4(x)}{64} = \frac{\pi}{64}\frac{D^4 l^4 (k - \sqrt{x})^4 - D_0^4 k^4 (l - \sqrt{x})^4}{k^4 l^4} \tag{34}$$

and the differential equation of deflected axis takes the form

$$\frac{\pi E}{32q}\frac{d^2 u(x)}{dx^2} = \frac{x^2 - 2Lx + L^2}{\frac{D^4}{k^4}(k - \sqrt{x})^4 - \frac{D_0^4}{l^4}(l - \sqrt{x})^4}. \tag{35}$$

The two-time integration allows to obtain the result in the form

$$\frac{\pi E}{32q}u(x) = R(x) \tag{36}$$

wherein the term $R(x)$ is too spacious to place it here.

Table 1 Comparison of values of frequency parameter Q for truncated cones with different convergence ratios

$\frac{1}{\eta} = \frac{d}{D}$	0.1	0.3	0.5	0.7	0.9
Q acc. [20]	2.684189	2.347181	2.150616	2.016664	1.916690
Q from this paper	2.697983	2.348014	2.153194	2.020153	1.920438

The comparison of the expressions for the potential and kinetic energies allows to determine the vibration period

$$T = \frac{4\pi}{kl} \sqrt{\frac{2\rho}{E}} \sqrt{\frac{\int_0^L [D^2 l^2 (k - \sqrt{x})^2 - D_0^2 k^2 (l - \sqrt{x})^2] R^2(x) dx}{\int_0^L R(x) dx}}. \tag{37}$$

Due to the size of these equations and to the necessity of numerical integration, it is the best to perform the calculations using a computer. The authors used Mathematica environment.

5 Comparison of results

5.1 Accuracy of results

The results for the truncated cone have been compared to those obtained by Lau [20] in the form of the Bessel functions replaced by polynomial equivalents (similarly as in [1]). In Table 1 the comparison of values of dimensionless frequency parameter Q, Eq. (38), for different convergence ratios is presented. A_0, J_0 are cross section area and second area moment of the bar for $x = 0$.

$$f = \frac{1}{T} = \frac{Q^2}{2\pi L^2} \sqrt{\frac{E J_0}{\rho A_0}}. \tag{38}$$

The accuracy of the parameter Q equals 0.5 %, hence – taking into consideration that in Eq. (38) this parameter is squared – the frequency (period) error does not exceed 1%. For practical calculations, such accuracy is sufficient. As the authors did not find in the literature any exact benchmark solutions for hollow curvilinear cones, the results have been compared to those obtained from FEM (ANSYS). For the analyzed truncated cone, the vibration period calculated in FEM was 0.2 % higher in average than in [1, 20], and the vibration period obtained by the authors was 0.4 % lower in average than in [1, 20].

The calculations in FEM for the hollow curvilinear cones were carried out in the following way. First, coordinates of 17 points on the generatrix of the internal and external curvilinear cone were calculated according to the curve equation. Next, the obtained points were joined with straight segments and a solid of revolution was made. Then, a regular HEXA mesh was created with application of SOLID elements. There was ca. 30 000 elements in total and 192 elements along the post's height.

5.2 Examples of calculation

The examples have been selected to show possibilities of typical engineering applications, to compare the results of the calculations according the derived formulas to those obtained in FEM and to investigate the influence of post slenderness to differences between those results. The examples of dependences of vibration period on the geometrical parameters of a conical tube shape cantilever bar are presented in Fig. 5. The following data have been assumed: $L = 2$ m, $D = 0.06$ m, $\sqrt{\rho/E} = 7 \cdot 10^{-4}$ s·m^{-1} (plastic). The convergence ratio of the bar walls varies within the range between the value for a cone ($\eta = \infty$, $d = 0$) to the value for a cylinder ($\eta = 1$, $d = D$), $\alpha = 0.7$, the values of the parameters β are diversified.

The curve for $\alpha = \beta$ concerns such a conical tube (considered on Fig. 2b) where the generatrices of the internal and external cone cross in the point placed on the longitudinal axis of the bar. The points of this curve
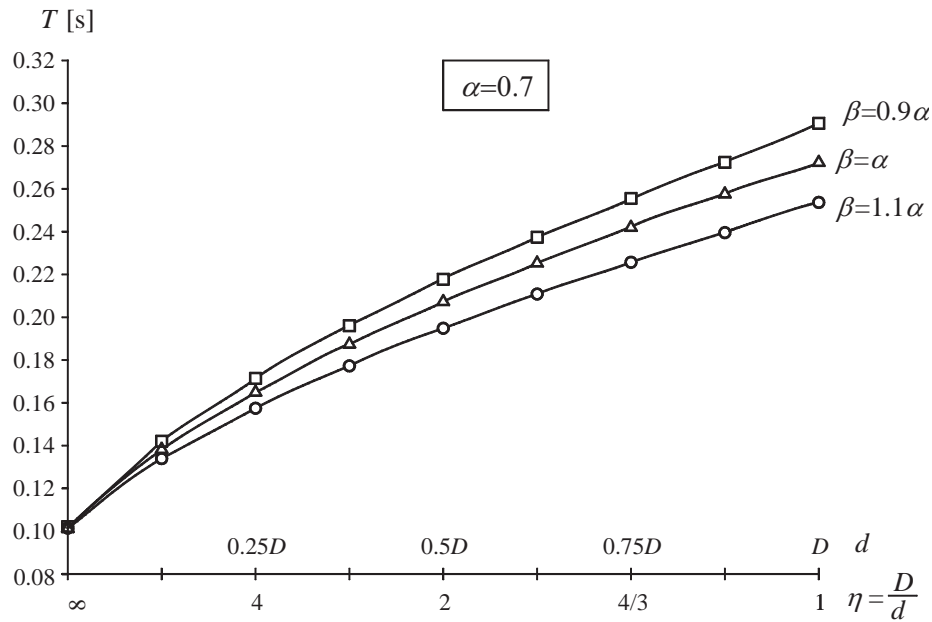
Fig. 5 Vibration period for conical tube [19], for $\alpha = 0.7$. Three cases are considered: for $\beta = 0.9\alpha$, $\beta = 1.0\alpha$, $\beta = 1.1\alpha$.
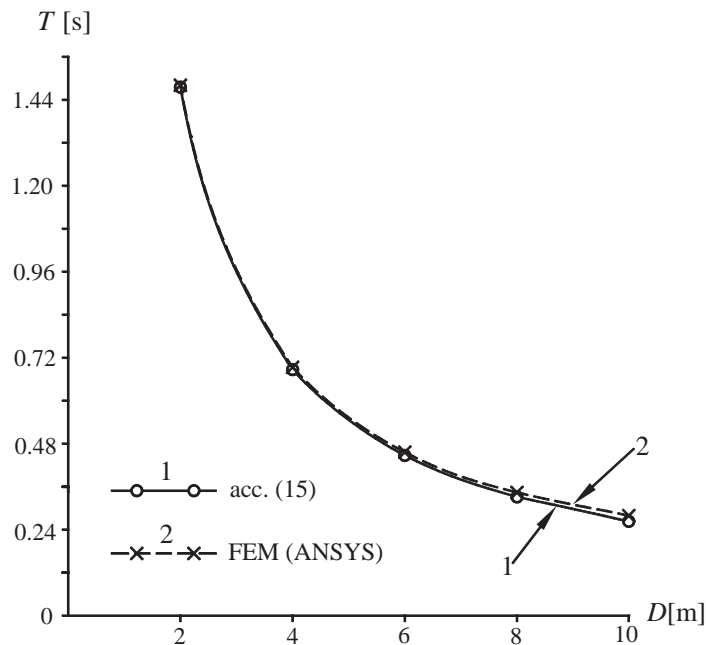

Fig. 6 Vibration periods of a ferroconcrete sheet construction [19] calculated: 1 - acc. Eq. (15), 2 - with FEM.

have been calculated according to the formula for a solid cone with consideration of appropriate corrective factor, given in [19]. It has been also checked that the obtained results exactly correspond to the vibration periods calculated according to Eq. (15) if, instead $\beta = \alpha$, it has been put $\beta = \alpha \pm \theta$, where θ is a quantity much smaller than α. For the tube ($\eta = 1$) and for the cone ($\eta = \infty$), the values of vibration period have been calculated from the formulas given in [19]. In this case, the approximated solution can also be obtained from Eq. (15) if there are placed the convergence ratios close to $\eta = 1$ and $\eta = \infty$, respectively. The obtained results for the case of hollow truncated cone show the conformity to the results for a hollow cone, hollow cylinder and
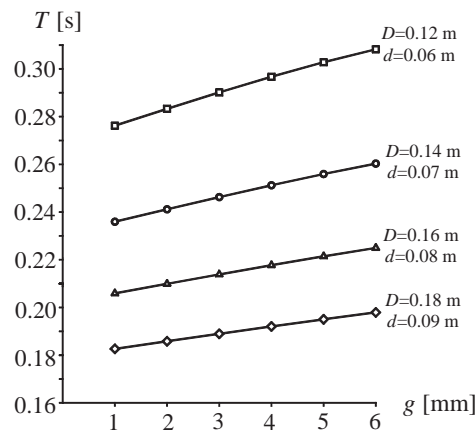
Fig. 7 Vibration periods of a steel post with a constant thickness [19].
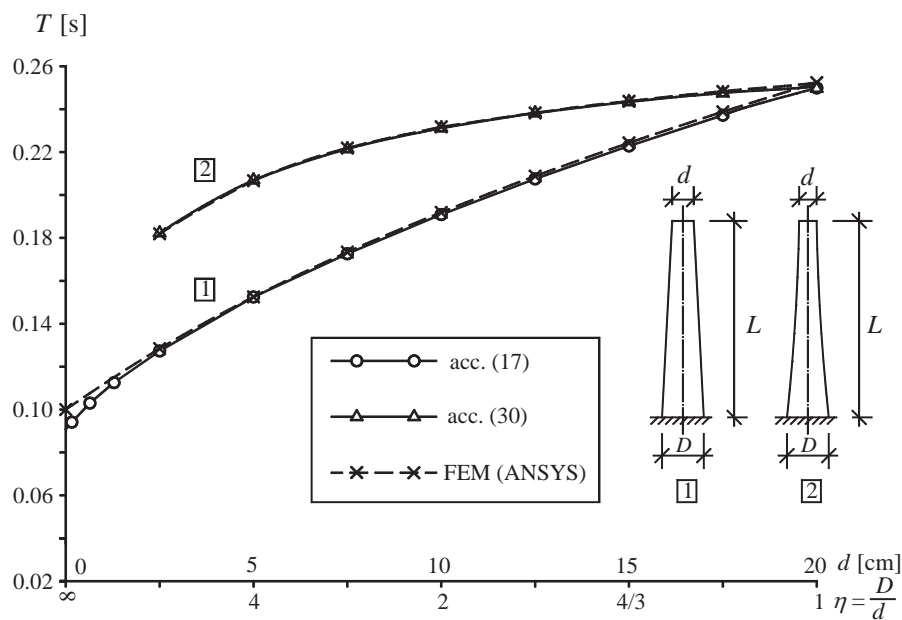

Fig. 8 Comparison of the vibration period of steel posts with the shape of truncated cone with linear and parabolic generatrix.

the special geometric case when $\alpha = \beta$.

Figure 6 presents the results of calculations of a vibration period of a ferroconcrete stress-skin construction in form of a conical tube (assumed $\sqrt{\rho/E} = 3.5 \cdot 10^{-4}$ s $\cdot$ m^{-1}) with the height $L = 48$ m, convergence ratio $\eta = 2$ and wall thickness (measured horizontally) by the base 0.27 m and by the head 0.06 m. Five diameters in the base have been considered, from $D = 2$ m to $D = 10$ m. In this range of diameters, the first natural frequency corresponds to bending vibrations. For the diameters $D \geq 12$ m, the first natural frequency corresponds to other forms of vibrations. The results of calculations according Eq. (15) have been compared to the results obtained with use of FEM (ANSYS). The great concordance of results is visible. For the diameters $D \leq 4$ m – what corresponds to the slenderness ratio (understood here as $\lambda = L/D$) greater or equal to 12 – the differences between these results are lower than 1 %. As the slenderness ratio diminishes, this difference increases and e.g. for $D = 10$ m ($\lambda = 4.8$) equals 5.6 %.

Figure 7 presents the results for a post made of steel sheet – such solution is very widely applied in practice. The post height has been assumed $L = 6$ m, diameters by the base D from 0.12 to 0.18 m, convergence ratio
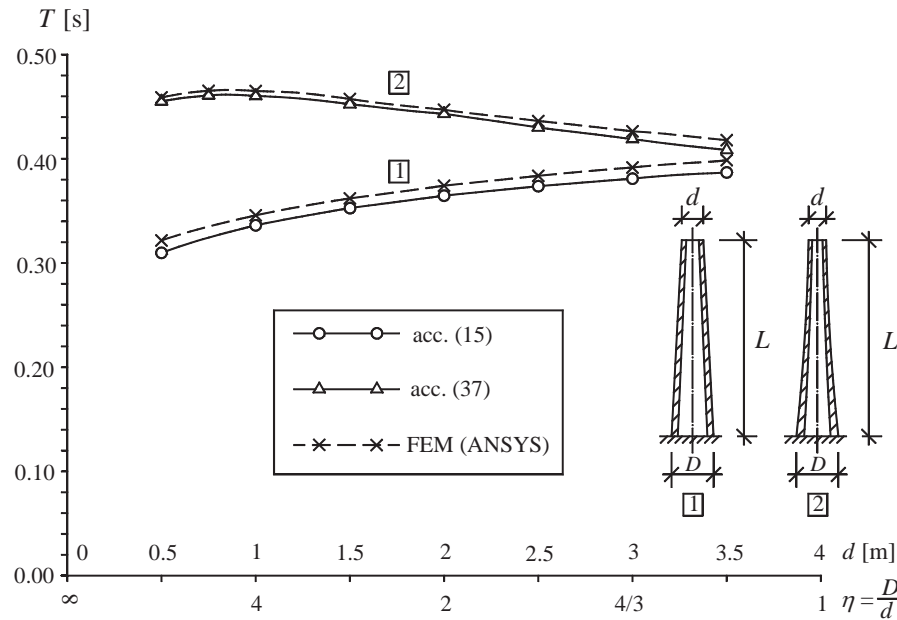
Fig. 9 Comparison of vibration period of ferroconcrete chimneys having the shape of a conical tube and parabolic cone tube.

$\eta = 2$. Various thicknesses g of the sheet have been considered, from 1 to 6 mm. It is a special case of the hollow cone as in Fig. 2d) – the formula for calculations was derived in [19]. The calculations could be also performed with some approximation, using Eq. (15) and assuming such parameters of the post so that the wall thickness be very close to a constant value g.

Figure 8 presents the comparison of the vibration periods for the solid truncated cone shape steel posts with parabolic generatrix and linear one. It has been assumed: $E = 205$ GPa, $\rho = 7850 \, \text{kg} \cdot \text{m}^{-3}$, post height $L = 6$ m, diameter by the base $D = 0.2$ m. Various ratios of inclination of lateral faces have been considered. The calculations have been performed according to the Eqs. (30) and (17). The results have been compared to those obtained in FEM (ANSYS). The slenderness of those posts is considerable ($\lambda = L/D = 30$), hence a very good concordance of results occurs.

The comparison of the vibration periods of two chimneys – hollow cone shape cantilever bars – is presented in Fig. 9. For the first of them, the generatrices of internal and external walls are linear (conical tube), for the second one - have the shape of a concave parabola (parabolic cone tube).

It has been assumed: $\sqrt{\rho/E} = 3.5 \cdot 10^{-4} \, \text{s} \cdot \text{m}^{-1}$, height $L = 32$ m, external diameter by the base $D = 4$ m, the wall thickness measured by the base 0.24 m and by the head 0.12 m, various convergence ratios corresponding to the external diameter by the head from $d = 3.5$ m to $d = 0.5$ m. The calculations have been performed according to Eqs. (15) and (37). The results have been compared to those obtained in FEM. The slenderness of the bars is not considerable ($\lambda = L/D = 8$) and the values of the vibration period calculated according to the formulas from this work and with the use of FEM differ from each other by 2% on average.

6 Conclusions

The formulas for the first natural frequency of bending vibrations of conical tube cantilever bars, derived from the Rayleigh method with the assumption that the neutral axis of the bar deflected during oscillations assumes a shape of a static deflection evoked by a constant continuous load, show compliance with the FEM solution, being satisfactory for practical calculations. Good compliance between the results for a tube having the shape of truncated cone has been also stated. The values of the integrals in the Rayleigh's quotient can be easily calcu-

lated in commonly accessible computational programs – the submitted proceeding is convenient for engineering calculations and in some cases can replace calculations in FEM.

In the case of truncated cone, an analytical solution of integrals has been found, thus the formula for vibration period (17) is so simple that a pocket calculator is enough for calculations. For the conical tube, the form of the formulas (10) and (11) demands to calculate the integrals in Eq. (15) in a numerical way. For the case of parabolic truncated cone the equation of bar deflection (23, 24) is not complicated but the calculation of the vibration period from Eq. (30) demands to integrate numerically. For the curvilinear cone tube with the parabolic generatrices of the wall, the equations are so spacious that the calculations should be performed in a computer environment, such like Mathematica. The amount of work needed to obtain a result in such way is small. The calculation results are very close to those obtained from FEM. The differences between the results are the smaller the higher the bar slenderness is and the vibration periods calculated in FEM are generally higher than those from the calculations according this paper.

The scheme of derivation of the formulas for natural frequencies for conical tubes and for hollow regular truncated pyramids is analogical. The analysis of quotients of areas and second area moments of the figures under consideration, which quotients are functions of a diameters or a side length, enables to determine correcting factors which allow to apply the formulas, derived in this paper, for regular truncated pyramids as well.

Acknowledgments

References

[1] Conway, H.D. and Dubil, J.F. (1965), Vibration frequencies of truncated-cone and wedge beams, *Journal of Applied Mechanics*, **32**(4), 932-934.

[2] Coşkun, S.B., Atay, M.T., and Öztürk, B. (2011), Transverse vibration analysis of Euler-Bernoulli beams using analytical approximate techniques, *Advances in Vibration Analysis Research*, InTech, Ebrahimi F. (Ed.), 1-22.

[3] Abdelghany, S.M., Ewis, K.M., Mahmoud, A.A., and Nassar, M.M. (2015), Vibration of a circular beam with variable cross sections using differential transformation method, *Beni-Suef University Journal of Basic and Applied Sciences*, **4**(3), 185-191.

[4] Suppiger, E.W. and Taleb, N.J. (1956), Free lateral vibration of beams of variable cross section, *Zeitschrift für angewandte Mathematik und Physik*, **7**(6), 501-520.

[5] Kang, J.H. and Leissa, A.W. (2004), Three-dimensional vibrations of solid cones with and without an axial circular cylindrical hole, *International Journal of Solids and Structures*, **41**(14), 3735-3746.

[6] Wu, J.S. and Chiang, L.K. (2004), Free vibrations of solid and hollow wedge beams with rectangular or circular cross-sections and carrying any number of point masses, *International Journal for Numerical Methods in Engineering*, **60**(3), 695-718.

[7] Datta, A.K. and Sil, S.N. (1996), An analysis of free undamped vibration of beams of varying cross-section, *Computers & Structures*, **59**(3), 479-483.

[8] Naguleswaran, S. (1994), A direct solution for the transverse vibration of Euler-Bernoulli wedge and cone beams, *Journal of Sound and Vibration*, **172**(3), 289-304.

[9] Naguleswaran, S. (1994), Vibration in the two principal planes of a non-uniform beam of rectangular cross-section, one side of which varies as the square root of the axial co-ordinate, *Journal of Sound and Vibration*, **172**(3), 305-319.

[10] Ece, M.C., Aydogdu, M., and Taskin, V. (2007), Vibration of a variable cross-section beam, *Mechanics Research Communications*, **34**(1), 78-84.

[11] Caruntu, D.I. (2007), Classical Jacobi polynomials, closed-form solutions for transverse vibrations. *Journal of Sound and Vibration*, **306**(3), 467-494.

[12] Zhou, D. and Cheung, Y.K. (2000), The free vibration of a type of tapered beams, *Computer Methods in Applied Mechanics and Engineering*, **188**(1), 203-216.

[13] Abrate, S. (1995), Vibration of non-uniform rods and beams, *Journal of Sound and Vibration*, **185**(4), 703-716.

[14] Guo, S.Q. and Yang, S.P. (2014), Transverse vibrations of arbitrary non-uniform beams. *Applied Mathematics and*

　　　Mechanics, **35**(5), 607-620.
[15] Firouz-Abadi, R.D., Haddadpour, H., and Novinzadeh, A.B. (2007), An asymptotic solution to transverse free vibrations of variable-section beams, *Journal of Sound and Vibration*, **304**(3), 530-540.
[16] Caruntu, D.I. (2009), Dynamic modal characteristics of transverse vibrations of cantilevers of parabolic thickness. *Mechanics Research Communications*, **36**(3), 391-404.
[17] Rao, S.S. (2011), *Mechanical vibrations*, Prentice Hall.
[18] Jaworski, J., Szlachetka, O., and Aguilera-Cortés, L.A. (2015), Application of Rayleigh's method to calculation of the first natural frequency of cantilever columns with variable cross-section, *Journal of Civil Engineering, Environment and Architecture*, **62**, 185-193 (in Polish).
[19] Jaworski, J. and Szlachetka, O. (2015), Free vibration of cantilever beams of various cross-section, *Dynamical Systems. Mechatronics and Life Sciences. DSTA'2015*, Awrejcewicz J. et al. (Eds.), 237-248.
[20] Lau, J.H. (1984), Vibration frequencies for a non-uniform beam with end mass. *Journal of Sound and Vibration*, **97**(3), 513-521.

Study of Negative Elements for Discrete Mechatronic Systems

Andrzej Buchacz[†], Damian Gałęziowski

Silesian University of Technology, Institute of Engineering Processes Automation and Integrated Manufacturing Systems, The Faculty of Mechanical Engineering, Konarskiego 18a Street, 44-100 Gliwice, Poland

Abstract

In the paper, the known problem of vibration control have been studied for elements which have defined configurations and connections of piezostack actuator with external electric network and can exhibits negative values. Depending on the phase of the synthesis process, used for the design of the mechatronic systems that have to comply with some given requirements, negative elements have been identified and described. Subsequently with the study on selection of corresponding negative stiffness and damping, presented in the graph form, optimal values for the systems can be compared. Following examples with selected calculations, the goal of this paper is to present limits and constrains that may support the physical realization, as well as applications of the considered systems.

1 Introduction

Technological development results in the automation and robotization of several different processes and products, in various industrial branches. Nowadays, all engineering work depends on the design that should correspond as much as possible to the defined models. With the help of the surrounding digitization, computer aided modeling (CAM), calculations, and smart materials, it's possible to determine new and consistently lower cost solutions for known physical problems. The unwanted effect of vibration, which is related mainly to machines and devices, as well as their work or use in different conditions, is one of the most important problems to solve That is due to the influence that durability, maintenance, and costs can generate. An optimization in the parameters of the modeled systems, on the assumed simplification level, will lead to calculable benefits and advantages in reality. As a consequence it will lead to the optimization of the costs in the fabrication and production of various goods.

The use of piezoelectric materials for vibration control is commonly known [1, 2]. First negative elements used for improving damping performance have been limited to the negative capacitance elements. That problem has been introduced while sound isolation by piezo polymer films [3], has been described based on analysis of one degree of freedom system in [2] and has been improved in [4]. The use of the synthesis to design and for modelling of mechatronic systems, have been introduced by the authors in [5]. Following the works [1–5], the

---

[†]Corresponding author.
Email address: Andrzej.buchacz@polsl.pl

authors investigated the possibilities to determine and use the parameters that lead to the negative value elements, as it has been introduced in [6]. As a result, it has been identified, that during synthesis process while reception of mechanical replacement model negative stiffness or damping elements can be received. The study on these elements has been done respectively in [7], and in [8–10].

The paper continues and extend the works done in the Gliwice Research Centre related to the design, analysis, and synthesis of various types of mechanical and mechatronic vibration systems [1,5,6]. Based on the recent world-wide studies, achievements connected to negative value elements [2–4,7–9] and authors work [5,6,10] a new approach for the problem of synthesis, that goes beyond known frames, is given. Investigations are focused for the details, limits and constrains connected with selection of major parameters. Negative capacitance and negative resistance elements, connected within specific circuits might be new interesting solutions in the vibration isolation area. Applying these achievements to the synthesis issue, it's possible to shorten the design time for the new systems that should work under specific and required conditions and widen the field of practical application in the area of vibration control

2 Mechatronic discrete systems

The considered mechatronic systems in each case are excited by the force $F(t)$ and include a mechanical part and a piezo stack actuator connected to an external electric network. Elements that can obtain negative values in these systems during solving the reverse task have been introduced by the authors in [6]:

- in mechanical replacement model: stiffness and damping

- in final mechatronic structure: negative capacitance and resistance.

All of them depend on the structure type, the complexity of the system (number of degrees of freedom – (DOF) and piezo elements), as well as selected synthesis method. More important, those related to mechanical replacement models are used indirectly. This is connected with the algorithm of synthesis [6] that contains transformation to dimensionless model and retransformation to final mechatronic structure phases.

3 Parameters identification

Due to complexity of the problem, the present study has been done based on the cascade discrete mechanical replacement model with 2 DOF (Fig. 1), received by the distribution of the dynamical characteristics function $U(s)$ [6] into continuous fractions. Dynamical characteristics function has been written as slowness function:

$$U(s) = H\frac{d_l s^l + d_{l-2} s^{l-2} + ... + d_0}{c_k s^k + c_{k-2} s^{k-2} + ... c_1 s},$$　(1)

where: l– odd degree of numerator, k– degree of denominator, $l - k = 1$, H– any positive real number.

The dynamic equation of the systems and the further analysis is done in dimensionless time τ:

$$\tau = \omega_{1,2} t.$$　(2)

To transform the electric parameters that comes from the piezo element characteristics from the non-dimensional model to the final mechatronic structure, the well-known piezoelectric equations are used:

$$\sigma = K_E s - eE,$$　(3)
$$D = es + \varepsilon_s E,$$　(4)

where: σ– mechanical stress, K_E– Young Modulus, s– mechanical strain, D– electrical displacement, ε_s– electrical permittivity, E– electrical field, e– piezoelectric constant.
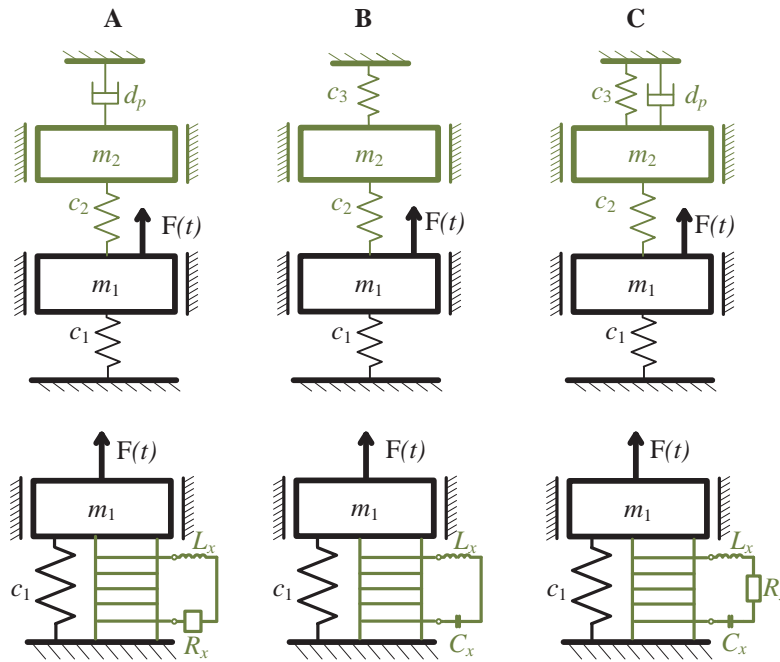
Fig. 1 Mechanical replacement models with 2 DOF and their final mechatronic structures that contains piezo actuators.

In the synthesis process, reception of mechanical replacement models have been algorithmized. A key parameter during the distribution, is the value of stiffness c_1 which determines the values of the other elements in the mechanical replacement model and indirectly impacts for the connection of the piezo with the electric circuit. Following Eq. (1), the selection range of c_1 is defined as:

$$(0, H\frac{d_0}{c_l}). \tag{5}$$

From the other side, the parameters related with applied piezo stack actuator, has been limited to the capacitance C_{ps}. That is needed to calculate the values of corresponding elements in the connected external circuits: *LRn*, *LCn*, *LRCn* (symbol n in written configuration types refers to negative values inside the network). The influence of the selection of both parameters that are leading to the optimal values and application constrains is shown in the next sections.

4 Passive *LR* configuration with negative resistance

To obtain the system represented in Fig. 1A, stiffness c_1 has to be equal to the upper limit (5). That generates in total the system with two inertial and stiffness elements in the mechanical replacement model. Here the damping element d_p normally should be considered according to the equations:

$$d_p = 2hm_2, 0 < h < |\omega_{\min}|, |\omega_{\min}| \neq 0. \tag{6}$$

However to adjust d_p for negative value, the value of parameter h has to be taken out of the limits (6) and should be below zero. That is generating after transformation and retransformation of the negative value of the resistance R_x, which has been used in vibration damping in [8, 9].

The impact of the selection of d_p out of defined frames (6) for the resistance in the *LR* configuration R_{xLR} of the considered systems is presented in Fig. 2.
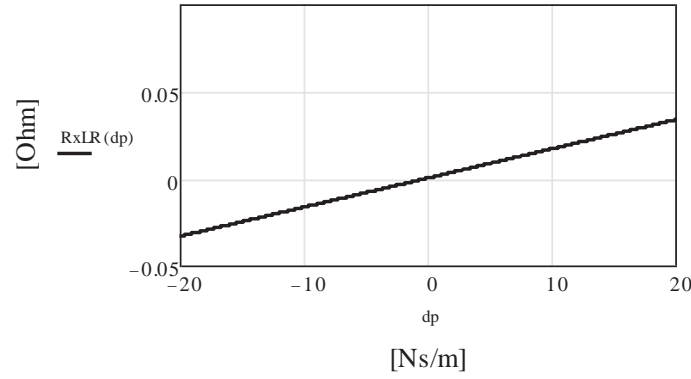
Fig. 2 Resistance R_{xLR} in the electric circuit in the function of damping d_p.
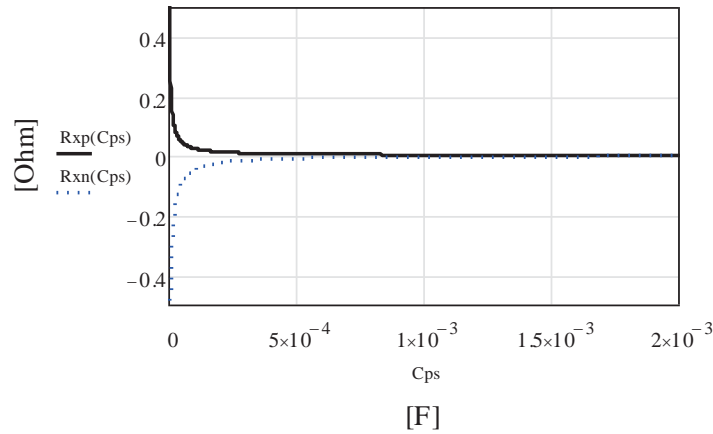

Fig. 3 Resistance in the electric circuit in the function of damping, for: the positive value of $d_p R_{xp}$, and negative value $-R_{xn}$.

The capacitance C_{ps} of the piezo can get only positive values. This is related to the fact that this value is connected with the applied stack actuator. The resistance R_x, is written as

$$R_x = \frac{d_p}{C_{ps} c_2}. \tag{7}$$

Following the Fig. 3 resistance R_x can get positive or negative values, depending on selection of damping element d_p in mechanical replacement model, Eq. (6).

5 *LC* configuration with negative capacitance

The *LCn* is one of the semi-active damping configuration of the system. Here the selection of c_1, determines all the parameters in the mechanical replacement model and what is the more important, it impacts on the appearance of additional c_3 stiffness in the system. Taking the value of c_1 out of its required range (5), it's possible to determine the negative values of the stiffness c_3, that determines together with the c_2 the dimensionless parameter δ (which directly impacts on capacitance C_x in the external electric network).

$$\delta = \frac{c_3}{c_2}, \tag{8}$$
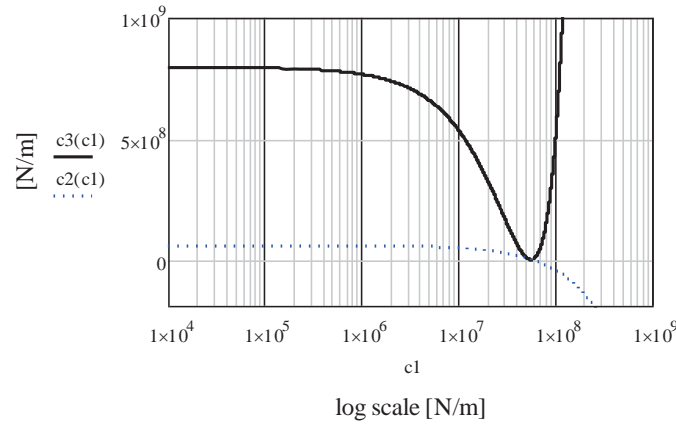
$$C_x = \frac{C_{ps}}{\delta}. \tag{9}$$

Fig. 4 The influence of selection of c_1 to c_2 and c_3 stiffness.
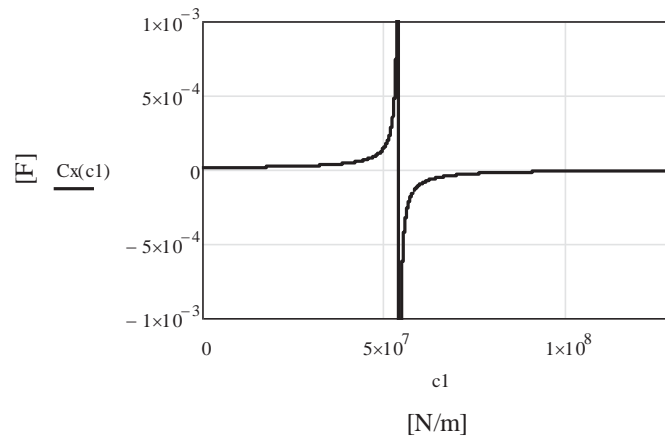

Fig. 5 Capacitance C_x in the function of c_1 stiffness.

In Fig. 4 the impact of the selection of c_1 to c_2 and c_3 stiffness has been highlighted. Then in Fig. 5, the behavior of the capacitance C_x is presented.

In the case of a *LCn* system, the selection of the c_1 impacts also on the inertial element m_2. That's having an indirect influence on the external inductance L_x. To check that impact, the following parameter λ is defined in the system as:

$$\lambda = \frac{\omega_1^2}{\omega_2^2}. \tag{10}$$

Based on Eq. (10), the dynamical equations of the mechanical replacement model and transformations done according to Eq. (2-4), the inductance L_x in electric network is written as:

$$L_x = \frac{\lambda}{C_{ps}\omega_1^2}. \tag{11}$$

The final dependence of the inductance L_x with constant C_{ps}, from selection of c_1 is presented in Fig. 6.

By increasing the value of the capacitance C_{ps} with the selection of piezo type actuator, referring to the Eq. (11) it's possible to decrease the value of L_x in the system.
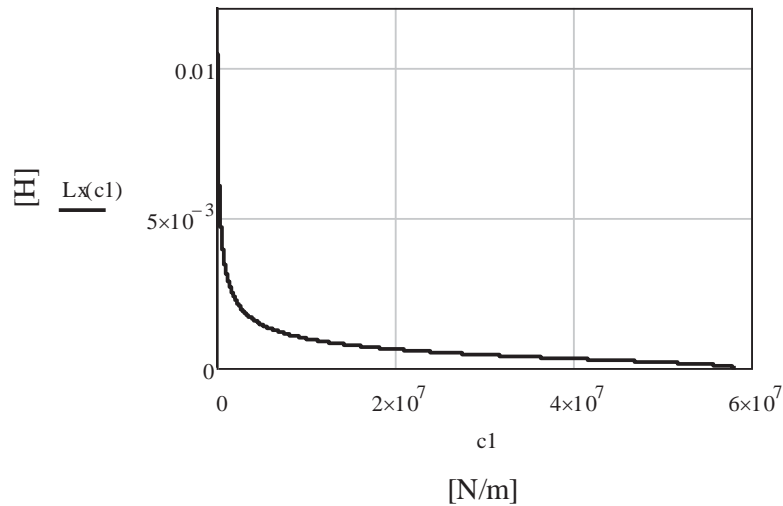
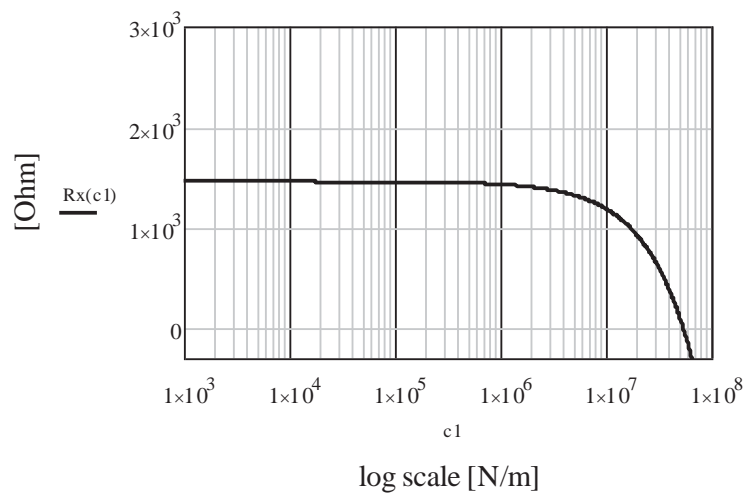**Fig. 6** Dependence of L_x, from selection of the stiffness c_1.

Fig. 7 Resistance R_x in the external electric network in the function of c_1.

6 *LRCn* configuration

Relations between inductance L_x, capacitance C_x and the selection of c_1, in case of the system *LRCn* are equal to *LCn* configuration. The difference is coming from the additional damping element, which, as opposed to *LRn* system is proportional to the stiffness element:

$$d_p = \chi c_3, 0 < \chi < \frac{2}{\omega_{\max}}, \omega_{\max} \neq 0. \tag{12}$$

Therefore the influence of c_1 to the external resistance R_x has been investigated and shown in Fig. 7. Its value is calculated following Eq. (7). Dependence of the stiffness c_2 from c_1 is the same as in Fig 4.

The selection of the stiffness c_1 in the case of various and increased values of requirements is shown in Fig. 8.

This has been presented due to the possibility of using the synthesis to design a system that has to comply with different requirements. It has been checked how the stiffness selection impacts the resistance in external electric network if resonant and anti-resonant frequencies are from the following ranges: 10^3 [rad/s] - solid line, 10^4 [rad/s] - dotted line, 15^4 [rad/s] - dashed line.
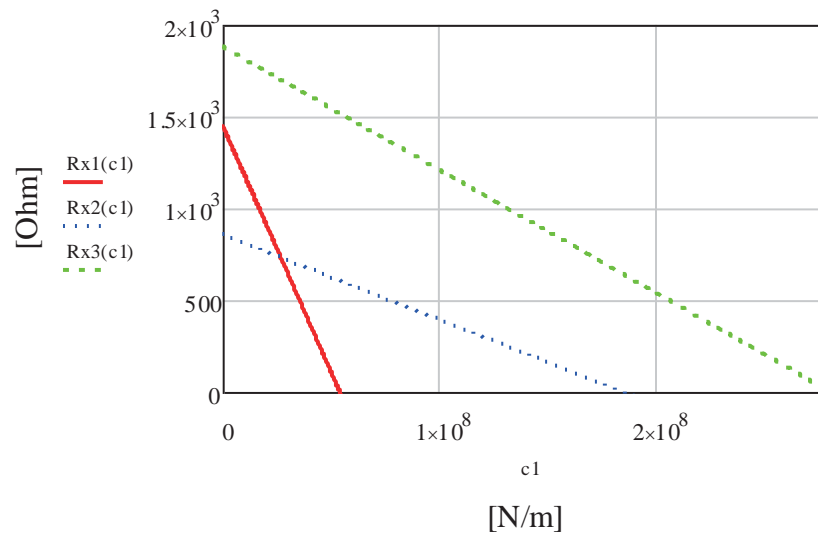
Fig. 8 Resistance R_x in the external electric network in the function of c_1.
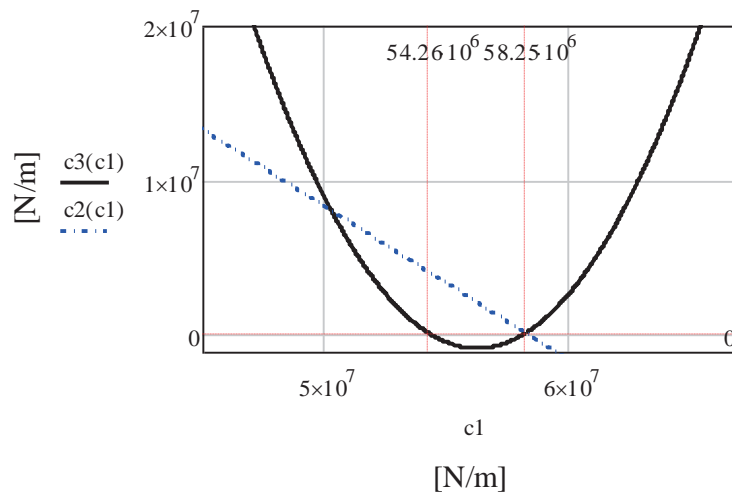

Fig. 9 Limits in the selection of c_1 for c_2 and c_3.

7 Physical realization study

From physical realization side, during the synthesis of considered systems, and the first phase of creation of mechanical replacement model, the selection of c_1 is the most important. As in the case of *LRn* configuration selection of c_1 doesn't have the influence on the parameters of the systems, in the case of *LCn* and *LRCn* it has to be taken into consideration while designing of structures that has to comply with given resonant and antiresonant frequencies. However there are some constrains that come from synthesis process. Selection of c_1 out of required range (5) results in the stiffness c_3 with negative value. Nonetheless this is realizable with the piezostack actuator connection with *LCn* or *LRCn* system, where electic circuit contains negative capacitance proposed in [2–4]. Taking the value of c_1 significantly larger than the upper limit (5), causes the value of c_3 gets again positive value, but c_2 receives in the same time a negative value, Fig. 9. That's out of the defined frames of considered systems, which means systems with negative stiffness c_2 are not possible to be synthesized.

Another issue has been identified as damping or resistance in *LRn* or *LRCn* system. As in the case of *LRn*, the value of damping has to be lower than zero from the definition, in the case of *LRCn* it can be as well, but this
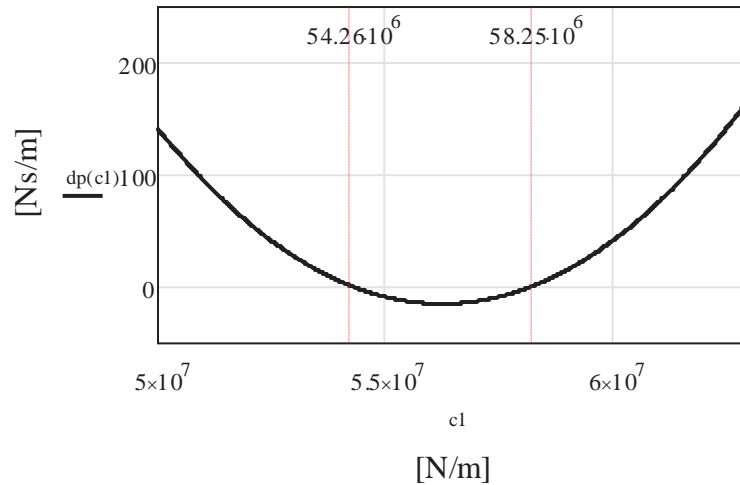
Fig. 10 Damping d_p in the function of c_1.

is not a must. With the selection of c_1, the value of d_p can be adjusted to a negative or positive value (Fig. 10) and used in the structure, following designer's needs.

8 Conclusions

In the present paper the negative elements and the most important parameters related to them, to find the optimal values while designing mechatronic discrete vibrational systems, have been studied. Physical realization constrains and range of the limits for the described parameters have been presented. Graphs that present the influence of selection of c_1 on the resistance in the external electric network, following the presented examples, give additional constrains and limits that should be taken into account while designing of mechatronic discrete systems. The paper is the verification and extension of the latest achievements related to the synthesis of considered systems and to use of piezo and negative elements in vibration control. Future work includes the study of this problem focusing on the use of novel negative resistance isolators in vibration control area.

Acknowledgments

References

[1] Buchacz, A. and Płczek, M. (2009), Damping of mechanical vibrations using piezoelements, including influence of connection layer's properties on the dynamic characteristic, *Solid State Phenomena*, **147-149**, 869-875.
[2] Neubaer, M., Oleskiewicz, R., Popp, K., and Krzyzynski, T. (2006), Optimization of damping and absorbing performance of shunted piezo elements utilizing negative capacitance, *Journal of sound and vibration*, **298**(1-2), 84-107.
[3] Fukada, M., Date, K., Kimura, and others. (2004), Sound Isolation by Piezoelectric Polymer Films Connected to Negative Capacitance Circuits, *IEEE Transactions on Dielectrics and Electrical Insulation*, **11**(2), 328-333.
[4] Han, X., Neubauer, M., and Wallaschek, J. (2013), Improved piezoelectric switch shunt dumping technique using negative capacitance, *Journal of Sound and Vibration*, **332**(1), 7-16.
[5] Białas, K., Buchacz, A., and Gałęziowski, D. (2013), Modelowanie dyskretnych układów mechatronicznych ze wzglęu na funkcję tłumienia, *Modelowanie In żnierskie*, **16**(47), 31-35.
[6] Buchacz, A. and Gałęziowski, D. (2015), Designing of discrete mechatronic vibrating systems with negative value

parameters, *Mechanical Systems and Signal Processing*, doi:10.1016/j.ymssp.2015.02.003.

[7] Kashdan, L., Conner, S.C., Haberman, M., and Wilson, P.S. (2012), Design, fabrication, and evaluation of negative stiffness elements using SLS, *Rapid Prototyping Journal*, **18**(3), 194-200.

[8] Yan, B., Zhang, X., and Niu, H. (2012), Design and test of a novel isolator with negative resistance electromagnetic shunt damping, *Smart Materials and Structures*, **21**(3), ID035003.

[9] Zhao, J. and Tang, J. (2013), Amplifying damage signature in periodic structures using enhanced piezoelectric networking with negative resistance elements, *Journal of Intelligent Material Systems and Structures*, **24**(13), 1613-1625.

[10] Buchacz, A. and Gałęziowski, D. (2015), Negative elements optimization in synthesis of discrete mechatronic systems, 13th International Conference Dynamical Systems Theory and Applications, December 7-10, 2015, Łódź Poland, DSTA2015 Book.

Fibre Spring-damper Computational Models in a Laboratory Mechanical System and Validation with Experimental Measurement

Pavel Polach[1†], Miroslav Byrtus[1], Zbyněk Šika[2], Michal Hajžman[1]

[1] New Technologies for the Information Society, European Centre of Excellence, University of West Bohemia, Plzeň, Univerzitní 8, Czech Republic

[2] Department of Mechanics, Biomechanics and Mechatronics, Czech Technical University in Prague, Prague, Technická 4, Czech Republic

Abstract

The paper deals with searching for the phenomenological model of a fibre. A multibody model of a simple weight-fibre-pulley-drive mechanical system is created. This mechanical system is focused on the investigation of a fibre behaviour and experimental laboratory measurements are performed on it. The carbon fibre, which is driven by one drive, is led over a pulley. On its other end there is a prism-shaped steel weight, which moves in a prismatic linkage on an inclined plane. Drive excitation signals can be of different shapes with the possibility of variation of a signal rate. Time histories of the weight position and of the force acting in the fibre are measured. At simulating with the multibody model of this system there is investigated the influence of dependences of the fibre spring-damper coefficients on the velocity of the weight motion in the computational model, on the coincidence of the simulation results and the experimental measurement results are evaluated. The aim of the simulations is to create a phenomenological model of the fibre, which will be utilizable in fibre modelling in the case of more complicated mechanical or mechatronic systems.

©2017 L&H Scientific Publishing, LLC. All rights reserved.

1 Introduction

The replacement of the chosen rigid elements of manipulators or mechanisms by fibres or cables [1] is advantageous due to the achievement of a lower moving inertia, which can lead to a higher machine speed, and lower production costs. Drawbacks of using the flexible elements like that can be associated with the fact that cables should be only in tension (e.g. [2, 3]) in the course of a motion.

Fibres and cables are used especially in the parallel kinematic mechanisms (PKM). Cable-driven variants of the PKM have further advantages, viz. a large range of motion, the possibility of antibacklash property [4] and easy reconfiguration. Their application scope ranges from the cargo handling [5] and astronomic applications [6, 7] to humanoid-arm manipulators [8] and snake-like manipulators [9]. Typical disadvantages of the cable-driven PKM are a relatively narrow frequency bandwidth of their feedback motion control and problems with the

---

[†]Corresponding author.
Email address: ppolach@ntis.zcu.cz

accurate positioning of the end-effector. The promising research direction for solution of these problems is the concept of multi-level mechanisms with a hierarchic structure composed of a parallel cable-driven mechanism for large and slow motions and an active structure connected to the mechanism platform for low and high frequency motions [10].

Experimental measurements focused on the investigation of the fibre behaviour are performed on an assembled weight-fibre-pulley-drive mechanical system (WFPDMS) [11–15] The fibre is driven with one drive, it is led over a pulley and on its other end there is a prism-shaped steel weight, which moves on an inclined plane. The position of the weight can be symmetric (see Fig.1) or asymmetric with respect to the plane of a drive-pulley symmetry (note: results with symmetric position of the weight are presented in this paper). It is possible to add an extra mass to the weight. Time histories of the weight position and of the force acting in the fibre are measured. The same system is numerically investigated using multibody models created in the *alaska* simulation tool [16]. The influence of the model parameters on the coincidence of the results of experimental measurements and the simulations results is evaluated. The simulation aim is to create a phenomenological model of a fibre, which will be utilizable in fibre modelling in the case of more complicated mechanical or mechatronic systems.

The fibre damping coefficient, the fibre stiffness and the friction force acting between the weight and the prismatic linkage were considered to be the system parameters of the phenomenological model. The parameters determined at investigating the weight-fibre system [17] were applied in the fibre model of the WFPDMS. The friction force acting between the weight and the prismatic linkage, as it has been confirmed [11–13], is not the parameter of the phenomenological model. This quantity is dependent on angle α of the inclined plane (see Fig.1). At simulating the experimental measurements for a "slower" drive motion [11–13] the local extremes of the time histories of the weight displacement (THWD) and the time histories of the dynamic force (THDF) acting in the fibre are independent of the fibre stiffness and the fibre damping coefficient (considered in feasible intervals of values). At simulating the experimental measurements for "quicker" drive motion [11–13] the local extremes of the monitored time histories are dependent on both the phenomenological model parameters (to explain: frequencies of drive motion – i.e. frequencies of periodic input signal – higher than 1 Hz are designated as "quicker" drive motions, frequencies of periodic drive motion lower than 1 Hz are designated as "slower" drive motions). From the obtained results it is evident that these parameters of the fibre phenomenological model must be, in addition, considered dependent on the velocity of the weight motion [14, 15, 18]. That is why the influence of considering the velocity-dependent stiffness [18] and/or the velocity-dependent damping "coefficient" [14]/[15] in the fibre model on dynamic response of the system was investigated.

This paper is a modified and extended version of [19]. Comparing to [19], this paper contains, in addition, discussion of the approach to the evaluation of coincidence of two discrete time series and reasoning that the response of dynamic behaviour of the WFPDMS to the kinematic excitation is not related to the resonant vibration.

2 Experimental stand

As it has been already stated experimental measurements focused on the investigation of the fibre behaviour are performed on an assembled WFPDMS (see Fig. 1). A carbon fibre with a silicone coating is driven with one drive and it is led over a pulley. The fibre length is 1.82 meters (fibre weight is 4.95 grams), the pulley diameter is 80 millimetres. The weight position can be symmetric [11, 13] (see Fig.1) or asymmetric [12] with respect to the vertical plane of drive-pulley symmetry (distance of the weight from the vertical plane of drive-pulley symmetry is 280 millimetres in the case of the asymmetric weight position). At the drive the fibre is fixed on a force gauge. At the other end of the fibre there is a prism-shaped steel weight (weight 3.096 kilograms), which moves in a prismatic linkage on an inclined plane. It is possible to add an extra mass (weight 5.035 kilograms) to the weight [13]. The angle of inclination of the inclined plane can be changed. In the case of the symmetric weight position the angle is $\alpha = 30$ degrees and the pulley-fibre angle is $\varphi = 150$ degrees (in the case of the asymmetric weight position the angle is $\alpha = 30.6$ degrees and the pulley-fibre angle is $\varphi = 146$ degrees).
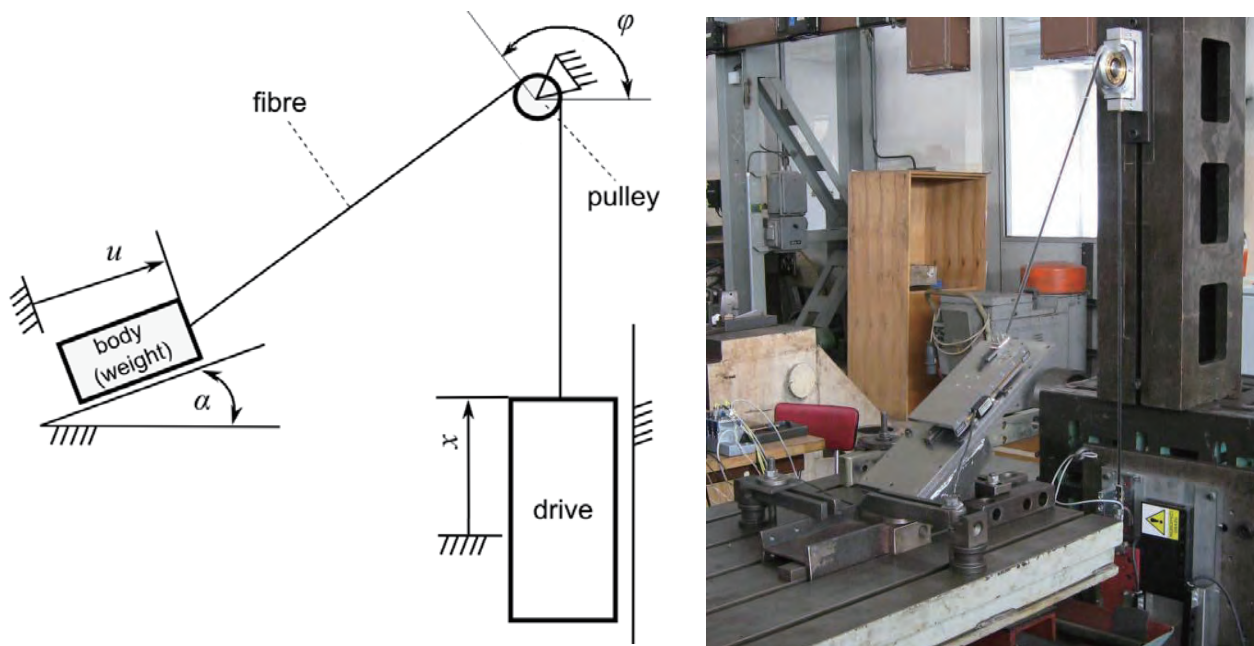
Fig. 1 Scheme and a real WFPDMS (symmetric position of the weight).

Drive periodic exciting signals can be of a rectangular, a trapezoidal and a quasi-sinusoidal shape and there is a possibility of variation of a signal rate [20]. The amplitudes of the drive displacements are up to 90 millimetres. Time histories of weight position u (in direction of the inclined plane; measured by means of a dial gauge), of drive position x (in vertical direction) and of the force acting in the fibre (measured by a force gauge at drive) are recorded using a sample rate of 2 kHz.

3 Possibilities of the fibre modelling

The fibre (cable, wire etc.) modelling [21] should be based on considering the fibre flexibility and suitable approaches can be based on the flexible multibody dynamics (see e.g. [22, 23]). Flexible multibody dynamics is a rapidly growing branch of computational mechanics and many industrial applications can be solved using newly proposed flexible multibody dynamics approaches. Studied problems are characterized by a general large motion of interconnected rigid and flexible bodies with the possible presence of various nonlinear forces and torques. There are many approaches to the modelling of flexible bodies in the framework of multibody systems. Comprehensive reviews of these approaches can be found in [22] or in [24]. Further development together with other multibody dynamics trends was introduced in [25]. Details of multibody formalisms and means of the creation of equations of motion can be found e.g. in [26] or [27].

The simplest way how to incorporate fibres in equations of motion of a mechanism is the force representation of a fibre (e.g. [28]). It is assumed that the mass of fibres is low to such an extent comparing to the other moving parts that the inertia of fibres is negligible with respect to the other parts. The fibre is represented by the force dependent on the fibre deformation and its stiffness and damping properties. This way of the fibre modelling is probably the most frequently used one in the cable-driven robot dynamics and control (e.g. [29, 30]). The fibre-mass system fulfils all requirements for modelling the fibre using the force representation of the fibre. A more precise approach is based on the representation of the fibre by means of a point-mass model (e.g. [31]). It has the advantage of a lumped point-mass model. The point masses can be connected by forces or constraints.

The massless fibre model is considered in this phase of investigation of the WFPDMS. The fibre model is considered to be phenomenological and it is formed by the forces which comprise e.g. influences of fibre

transversal vibration, "jumping" from pulley etc. The multibody models of the WFPDMS in the case of considering the symmetric and asymmetric position of the weight with respect to the plane of drive-pulley symmetry slightly differ [11, 12]. In the case of symmetric position the number of degrees of freedom in kinematic joints is 5 (in the case of asymmetric position the number of degrees of freedom in kinematic joints is 6). The weight (with added mass), the pulley and the drive are considered to be rigid bodies. A planar joint between the weight and the base (prismatic linkage), a revolute joint between the pulley and the base and a prismatic joint between the drive and the base (the movement of the drive is kinematically prescribed) are considered. Behaviour of this nonlinear system is investigated using the *alaska* simulation tool [16].

4 Simulation and experimental results

As it has already been stated the simulations aim was to create a phenomenological model of a fibre. When looking for compliance of the results of experimental measurement with the results of simulation influences of the fibre stiffness and the fibre damping coefficient are considered. The friction force acting between the weight and the prismatic linkage in which the weight moves was considered to be the phenomenological model parameter in the first phase of investigation [17].

Investigation of the (carbon) fibre properties eliminating the influence of the drive and the pulley was an intermediate stage before the measurement on the stand [17]. A phenomenological model dependent on the fibre stiffness, on the fibre damping coefficient and on the friction force acting between the weight and the prismatic linkage was the result of this investigation. When looking for the fibre model [17] that would ensure the similarity of the THWD and the THDF acting in a fibre as high as possible a fibre stiffness and a fibre damping coefficient were considered to be constant in this phase of the fibre behaviour research. The nonlinear friction force course (in dependence on the weight velocity) determined (especially on the basis [32, 33]) at investigating the weight-fibre mechanical system with the angle of inclination of the inclined plane $\alpha = 30$ degrees is applied in the model of the WFPDMS [11–13]. Values of fibre stiffness and fibre damping coefficient were calculated on the basis of the values determined in [11–13] (see Table 1).

At simulating the experimental measurements for a "quicker" drive motion [11–13] the local extremes of the time histories of the measured and the calculated weight displacement were more or less different. From these results it was evident that the parameters of the fibre phenomenological model must be, in addition, considered dependent on the velocity of the weight motion. That is why the influence of considering the velocity-dependent stiffness [18] and/or the velocity-dependent damping "coefficient" [14]/[15] in the fibre model on dynamic response of the system was investigated.

Velocity-dependent stiffness c of the fibre is supposed to be in the form

$$c = \begin{cases} c_c, & \text{if } v \leq v_{tr} \\ c_c + (v - v_{tr}) \cdot c_2, & \text{if } v > v_{tr}, \end{cases} \tag{1}$$

where c_c is the constant fibre stiffness (taken from [11]), c_2 is the constant, v is the instantaneous velocity of the weight and v_{tr} is the threshold value of the velocity of the weight. Optimal (constant) values of constant c_2 and threshold value of weight velocity v_{tr} were found. Threshold value of weight velocity v_{tr} was found in [18] and confirmed in [14, 15].

Velocity-dependent damping "coefficient" b of the fibre is considered similarly as the velocity-dependent stiffness (see Eq.(1))

$$b = \begin{cases} b_c, & \text{if } v \leq v_{tr} \\ b_c + (v - v_{tr}) \cdot b_2, & \text{if } v > v_{tr}, \end{cases} \tag{2}$$

where b_c is the constant fibre damping coefficient (taken from [11]), b_2 is the constant. The optimal (constant) value of constant b_2 was found.

The influence of the velocity-dependent stiffness and/or the velocity-dependent damping "coefficient" values on the THWD (and also on the THDF acting in the fibre) was evaluated partly visually and partly on the basis of

Table 1 Values of coefficients of the fibre model

	Threshold value of the velocity	Stiffness		Damping coefficients	
	[m/s]	[N/m]	[N/s]	[N·s/m]	[N]
	v_{tr}	c_c	c_2	b_c	b_2
Constant coefficients	–	$34 \cdot 10^3$		27.5	–
Velocity-dependent stiffness	0.4	$34 \cdot 10^3$	730	27.5	0
Velocity-dependent damping "coefficient"	0.4	$34 \cdot 10^3$		27.5	385
Velocity-dependent coefficients	0.4	$34 \cdot 10^3$	850	27.5	3.1

the value of the correlation coefficient between the records of the experimental measurements and the simulation results. Application of the approach based on the calculation of the statistical quantities that enables to express directly the relation between two time series has appeared to be suitable for comparing two time series in various cases – e.g. [34].

Correlation coefficient $R(\mathbf{p})$ [35] defined for two discrete time series $x^{(1)}$ (the time history recorded at experimental measurement) and $x^{(2)}(\mathbf{p})$ (the time history determined at simulation with the multibody model; function of investigated parameters $\mathbf{p}$) was calculated

$$R(\mathbf{p}) = \frac{\sum\limits_{i=1}^{n} (x_i^{(1)} - \mu_1) \cdot [x_i^{(2)}(\mathbf{p}) - \mu_2(\mathbf{p})]}{\sqrt{\sum\limits_{i=1}^{n} (x_i^{(1)} - \mu_1)^2 \cdot \sum\limits_{i=1}^{n} [x_i^{(2)}(\mathbf{p}) - \mu_2(\mathbf{p})]^2}}, \tag{3}$$

where μ_1 and $\mu_2(\mathbf{p})$ are mean values of the appropriate time series. The maximum value of the correlation coefficient is 1. The more the compared time series are similar to each other the more the correlation coefficient tends to 1. The advantage of the correlation coefficient is that it quantifies very well the similarity of two time series by scalar value, which is obtained using a simple calculation.

The problem can be put as the problem of the minimization of the objective function in the form

$$\psi(\mathbf{p}) = (1 - R(\mathbf{p}))^2. \tag{4}$$

In case of the computer simulations in the *alaska* 2.3 simulation tool, the whole process of the optimization was limited by the impossibility of executing the analysis from the statement line and evaluating the results of numerical simulations without the necessary human intervention. The whole process could not be automated. "Manual" change in the parameters on the basis of the chosen optimization method was the only solution. Comparing to automated optimization process it is not possible to perform so many iteration cycles in a short time. But the advantage is that during the evaluation it is possible to respect criteria that do not have to be strictly mathematically formulated (the correlation coefficient $R(\mathbf{p})$ given by Eq.(3) enables to imagine coincidence of (time) series, but it is not "universal").

In Table 1 there are given the optimal values of parameters in Eq.(1) and in Eq.(2) of the investigated model of the WFPDMS. From Table 2 it is evident that the values of correlation coefficient $R(\mathbf{p})$ are "better" for the determined velocity-dependent coefficients than for the constant coefficients in the fibre model. In the THDF acting in the fibre the correlation coefficient $R(\mathbf{p})$ improvement is not evident very much – see Table 3 (the values are of rather informative character). At the THDF acting in the fibre during determining the optimum values of velocity-dependent coefficients attention was paid especially to keeping the character of their course and achieving the best possible agreement of extreme values of the measured and calculated dynamic forces.

At "slower" drive motions the THWD recorded at the experimental measurements and computed at the computer simulations are approximately identical (see [11–15] and Fig.6(a)) and hence it is not desirable to change

Table 2 Values of correlation coefficient $R(\mathbf{p})$ [-] of the THDF acting in the fibre

Tested situation	Constant coefficients	Velocity-dependent stiffness	Velocity-dependent damping "coefficient"	Velocity-dependent coefficients
2	0.9929	0.9937	0.9934	0.9954
3c	0.7552	0.9365	0.9190	0.9464
7a	0.9999	0.9999	0.9999	0.9999
10	0.9834	0.9838	0.9838	0.9836
11	0.2187	0.6909	0.6890	0.6534

Table 3 Values of correlation coefficient $R(\mathbf{p})$ [-] of the THWD

Tested situation	Constant coefficients	Velocity-dependent stiffness	Velocity-dependent damping "coefficient"	Velocity-dependent coefficients
2	0.3904	0.3761	0.3847	0.2868
3c	0.03925	0.0909	0.2084	0.1640
7a	0.5673	0.5743	0.5743	0.5743
10	0.5078	0.5080	0.5142	0.5047
11	0.2323	0.6778	0.1146	0.1462

values of parameters of the fibre phenomenological model (i.e. it is not necessary to consider the parameters of the fibre phenomenological model velocity-dependent). It is evident that it was the reason why the threshold value of velocity v_{tr} of the weight was determined in such a way that the maximum velocity of the weight during "slower" drive motions should be lower than v_{tr} (see Table 1).

Results of experimental measurements and simulations of five selected tested situations at weight symmetric position are presented in this paper (see Figs. 2 to 7). Four tested situations are at a "quicker" drive motion (see time histories of the drive motion in Fig.2(a), Fig.3(a), Fig.4(a) and Fig.5(a)) and one situation is at a "slower" drive motion (see time history of the drive motion in Fig.6(a)).

General pieces of knowledge obtained at investigating the WFPDMS, independently of the combination of the position of the weight with respect to the plane of the drive-pulley symmetry (symmetric or asymmetric) [12] and of the mass of the weight (without or with added mass) [14], are similar.

As it has already been stated in [13–15], the highest frequency of the drive motion (i.e. the highest frequency of input signal) at investigation of the WFPDMS is 2 Hz (see Fig.2(a), Fig.3(a), Fig.4(a) and Fig.5(a)). This frequency of the drive motion is much lower than natural frequencies of the computer model of the linearized system in an equilibrium position. Natural frequency corresponding to the weight vibrations of the system with the weight without added mass is 25 Hz and natural frequency of the system with the weight with added mass is 15.25 Hz. It means that in case of weight vibration at "quicker" tested situations the excitation of resonant vibrations is not concerned, but vibrations that are given by strongly nonlinear behaviour of a fibre (as it has been already stated, fibres are able to transfer only tensile force, in "compression" they are not able to transfer any force), which can even have the character of chaos, are involved.

At the "quicker" tested situations the measured and the computed THWD are of the same character (see Fig.2(a), Fig.3(a), Fig.4(a) and Fig.5(a)). On the basis of results it is evident that considering the velocity-dependent stiffness of the fibre in the model (not published), considering the velocity-dependent damping "coefficient" [15] and especially considering both the velocity-dependent stiffness and the velocity-dependent damping "coefficient" [14] contribute greatly to the improvement of agreement of the measured and the computed time histories and the local extremes of the weight displacement (see Fig.2(a), Fig.3(a), Fig.4(a) and Fig.5(a)).

As it has already been stated in [11–15] at all the simulations when changing the computational model parameters the THDF acting in the fibre are different (more or less) but their character remains the same. From
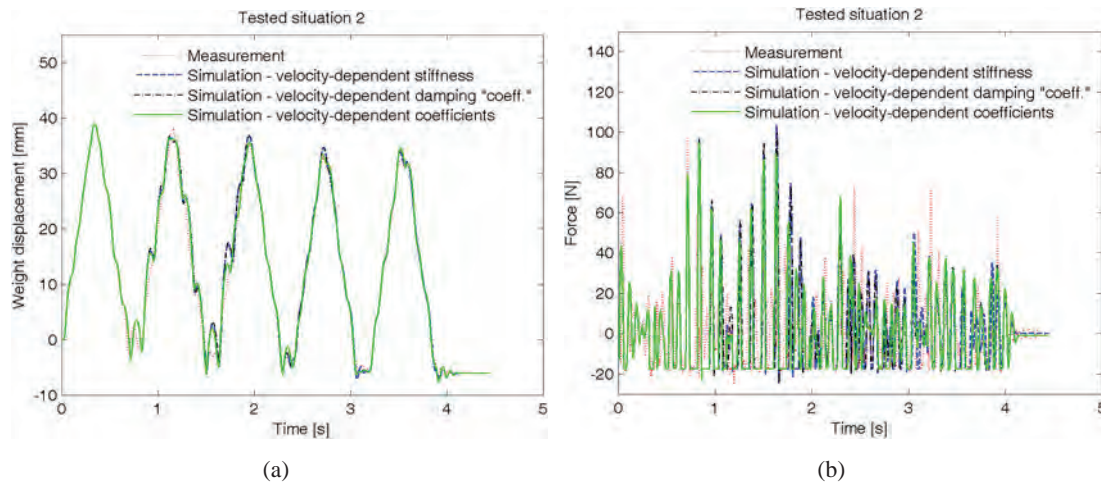
(a)　　　　　　　　　　　　　　　　　　(b)

Fig. 2 Time histories at a "quicker" tested situation (symmetric position of the weight, the weight without added mass): (a) Weight displacement and (b) dynamic force acting in the fibre.
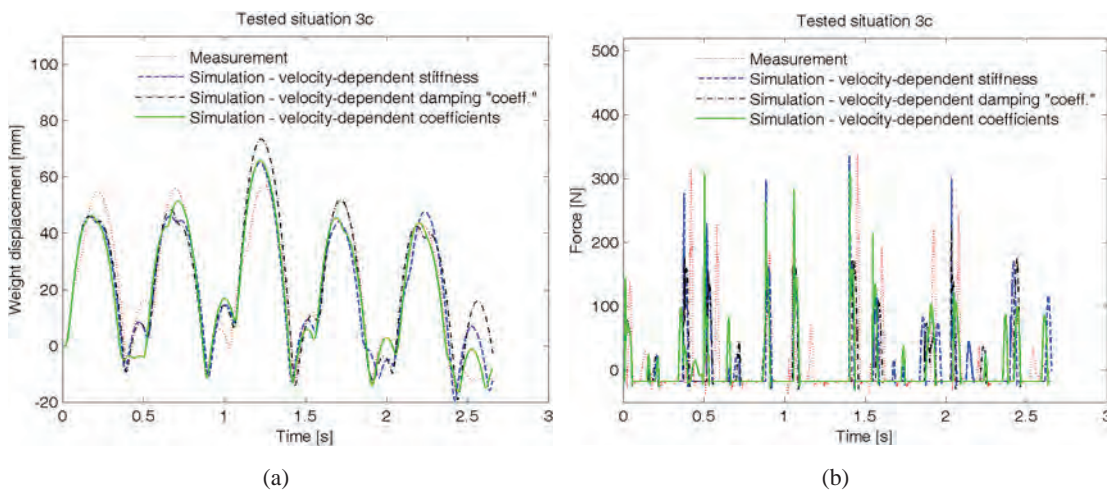

(a)　　　　　　　　　　　　　　　　　　(b)

Fig. 3 Time histories at a "quicker" tested situation (symmetric position of the weight, the weight without added mass): (a) Weight displacement and (b) dynamic force acting in the fibre.

Fig.2(b), Fig.3(b), Fig.4(b), Fig.5(b) and Fig.6(b) it is evident that the THDF acting in the fibre are not suitable for determining the parameters of the fibre phenomenological model. It follows from the fact that the phenomenological model of a fibre is to cover, as it has been stated, e.g. influences of the fibre transversal vibration, "jumping" from the pulley etc. As it does not include those phenomena physically (but by the change in the already introduced model parameters), it is evident, that the THDF acting in the fibre cannot be expected to be of the same course.

It is evident that for searching for the parameters of the fibre phenomenological model it is necessary to use the results of experimental measurements with the "quicker" drive motion. The possibility of performing experimental measurements with other time histories of drive motion or with a different geometrical arrangement of the experimental stand will be analysed.
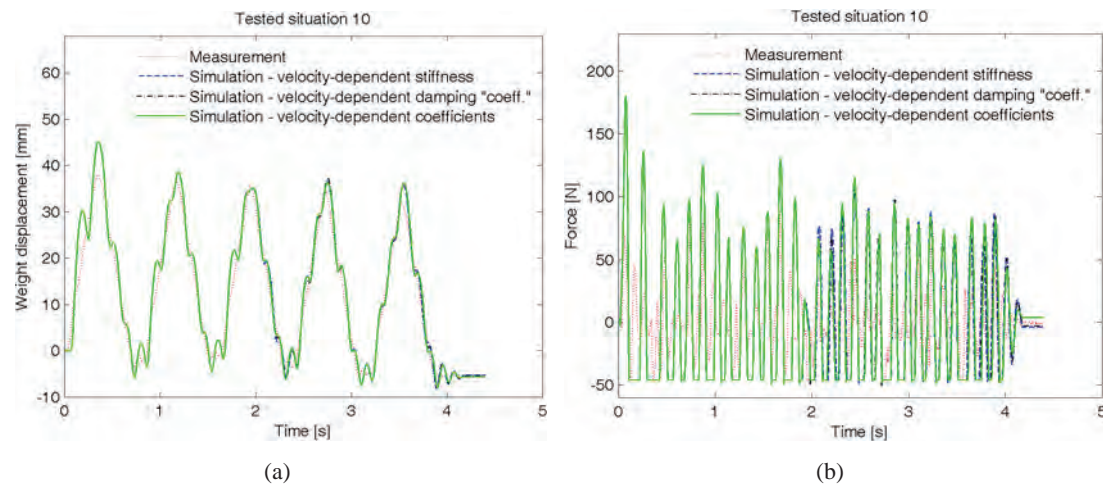
(a)   (b)

Fig. 4 Time histories at a "quicker" tested situation (symmetric position of the weight, the weight with added mass): (a) Weight displacement and (b) dynamic force acting in the fibre.
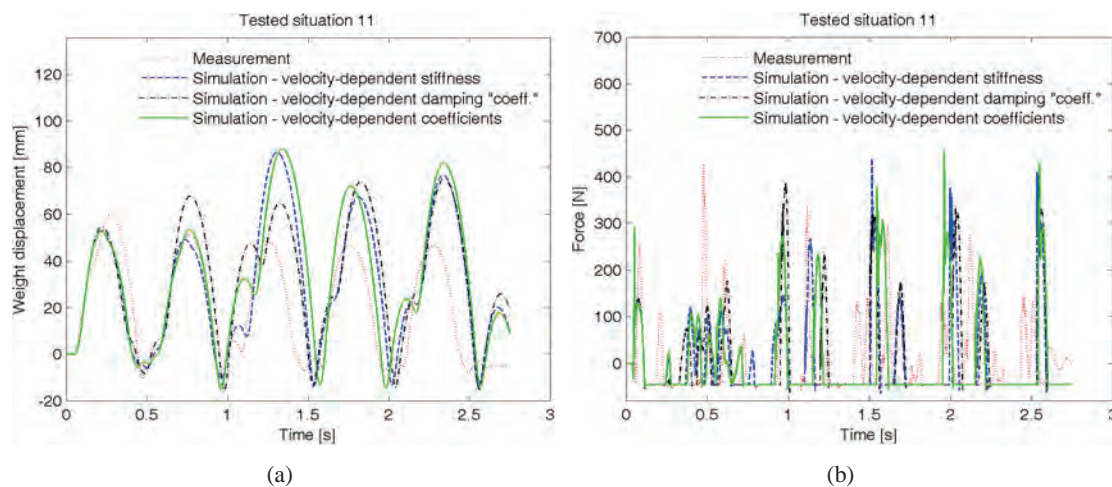

(a)   (b)

Fig. 5 Time histories at a "quicker" tested situation (symmetric position of the weight, the weight with added mass): (a) Weight displacement and (b) dynamic force acting in the fibre.

5 Conclusions

The approach to the fibre modelling based on the force representations was utilised for the investigation of the weight motion in the WFPDMS. The simulation aim was to create a phenomenological model of the fibre, which would be utilizable in fibre modelling in the case of more complicated mechanical or mechatronic systems. The created phenomenological model is assumed to be dependent on the velocity-dependent fibre stiffness and/or the velocity-dependent fibre damping "coefficient".

Development of the fibre phenomenological model continues. It can be supposed that in a more sophisticated phenomenological model of the fibre more complicated dependencies of the fibre stiffness and of the fibre damping "coefficient" on the weight velocity will be considered.

In addition it must be stated that the model of the fibre-pulley contact appears to be problematic in the computational model.
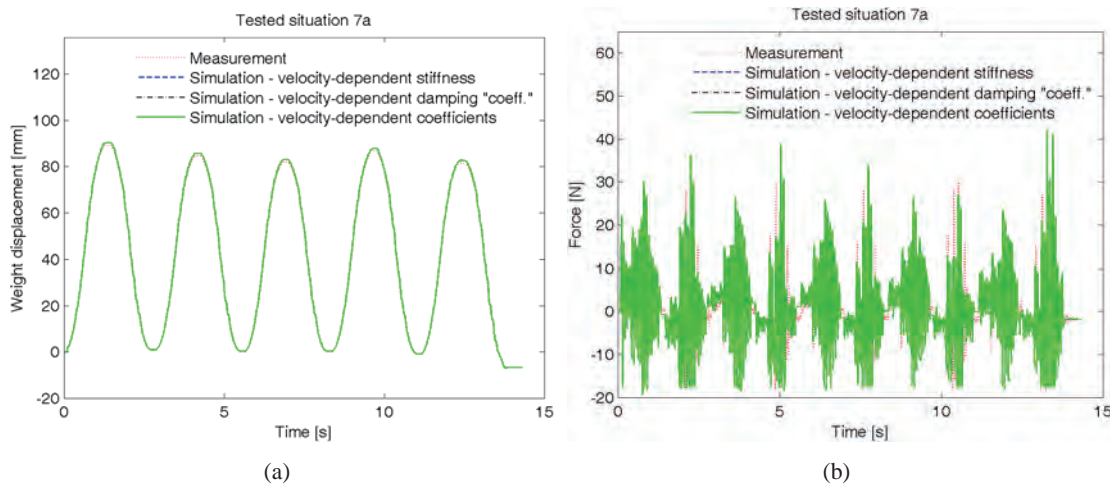
(a)　　　　　　　　　　　　　　　　　　(b)

Fig. 6 Time histories at a "slower" tested situation (symmetric position of the weight, the weight without added mass): (a) Weight displacement and (b) dynamic force acting in the fibre.
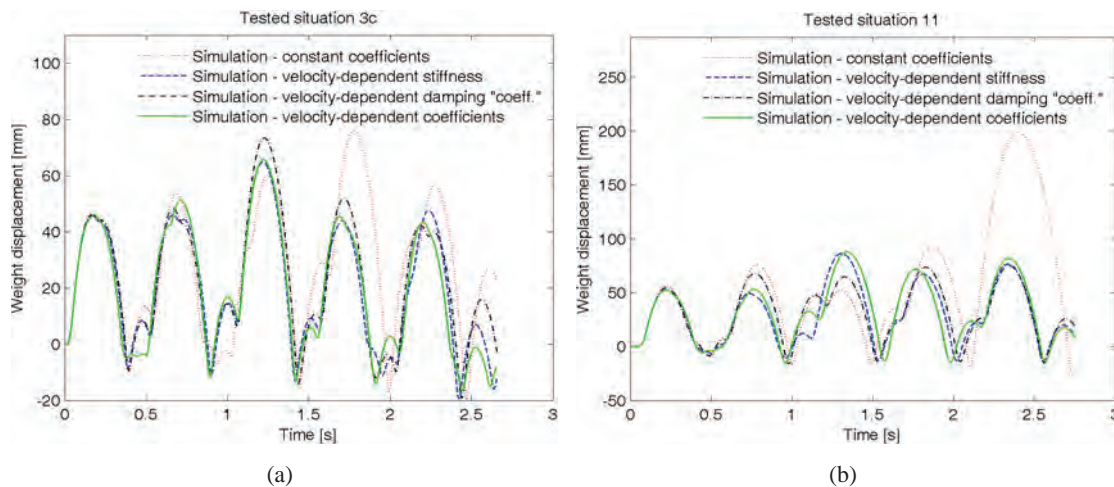

(a)　　　　　　　　　　　　　　　　　　(b)

Fig. 7 Time histories of the weight displacement at a "quicker" tested situation (symmetric position of the weight): (a) The weight without added mass and (b) the weight with added mass.

References

[1] Chan, E.H.M. (2005), *Design and Implementation of a High-Speed Cable-Based Parallel Manipulator, PhD Thesis*, University of Waterloo: Waterloo.

[2] Valášek, M. and Karásek, M. (2009), HexaSphere with Cable Actuation, *Recent Advances in Mechatronics: 2008-2009*, 239-244, Springer-Verlag: Berlin

[3] Gosselin, C. and Grenier, M. (2011), On the determination of the force distribution in overconstrained cable-driven parallel mechanisms, *Meccanica*, **46**(1), 3-15.

[4] Valášek, M. and Karásek, M. (2009), Kinematical Analysis of HexaSphere, *Proceedings of National Conference with International Participation Engineering Mechanics 2009*, Institute of Theoretical and Applied Mechanics AS CR, Svratka, CD-ROM (1371-1378).

[5] Patel, Y.D. and George, P.M. (2012), Parallel Manipulators Applications—A Survey, *Modern Mechanical Engineering*, **2**(3), 57-64.

[6] Zi, B., Zhu, Z.C., and Du, J.L. (2011), Analysis and control of the cable-supporting system including actuator dynamics, *Control Engineering Practice*, **19**(5), 491-501.

[7] Meunier, G., Boulet, B., and Nahon, M. (2009), Control of an Overactuated Cable-Driven Parallel Mechanism for a Radio Telescope Application, *IEEE Transactions on Control Systems Technology*, **17**(5), 1043-1054.

[8]   Chen, Q., Chen, W., Yang, G., and Liu, R. (2013), An Integrated Two-Level Self-Calibration Method for a Cable-Driven Humanoid Arm, *IEEE Transactions on Automation Science and Engineering*, **10**(2), 380-391.

[9]   Taherifar, A., Salarieh, H., and Alasty, A. (2013), Kinematic control of a new hyper-redundant manipulator with lockable joints, *Scientia Iranica, Transactions B: Mechanical Engineering*, **20**(6), 1742-1752.

[10] Duan, X.C., Qiu, Y., Du, J.L., Zhao, Z., and Duan, Q.J. (2011), Real-time motion planning for the macro-micro parallel manipulator system, *Proceedings of the 2011 IEEE International Conference on Robotics and Automation (ICRA 2011)*, IEEE, Shanghai, 4214-4219.

[11] Polach, P., Hajžman, M., Václavík, J., Šika, Z., and Svatoš, P. (2013), Model parameters influence of a simple mechanical system with fibre and pulley with respect to experimental measurements, *Proceedings of ECCOMAS Thematic Conference Multibody Dynamics 2013*, University of Zagreb, Faculty of Mechanical Engineering and Naval Architecture, Zagreb, CD-ROM.

[12] Polach, P., Hajžman, M., Václavík, J., Šika, Z., and Valášek, M. (2015), Investigation of a laboratory mechanical system with fibre and pulley, *International Journal of Dynamics and Control*, **3**(1), 78-86.

[13] Polach, P. and Hajžman, M. (2014), Influence of the Mass of the Weight on the Dynamic Response of the Laboratory Fibre-Driven Mechanical System, *Mechanisms and Machine Science 24, New Trends in Mechanism and Machine Science, From Fundamentals to Industrial Applications*, 233-241, Springer International Publishing Switzerland.

[14] Polach, P. and Hajžman, M. (2015), Influence of the fibre spring-damper model in a simple laboratory mechanical system on the coincidence with the experimental results, *Proceedings of ECCOMAS Thematic Conference on Multibody Dynamics*, Universitat Politècnica de Catalunya, Barcelona School of Industrial Engineering, Barcelona, 356-365.

[15] Polach, P., Hajžman, M., and Dupal, J. (2015), Influence of the Fibre Damping Model in a Simple Mechanical System on the Coincidence with the Experimental Measurement Results, *Proceedings of the 8th International Congress of Croatian Society of Mechanics*, Croatian Society of Mechanics, Opatija, USB flash drive.

[16] Maißer, P., Wolf, C.D., Keil, A., Hendel, K., Jungnickel, U., Hermsdorf, H., Tuan, P.A., Kielau, G., Enge, O., Parsche, U., Härtel, T., and Freudenberg, H. (1998), *alaska, User Manual, Version 2.3*, Institute of Mechatronics: Chemnitz.

[17] Polach, P., Hajžman, M., and Václavík, J. (2013), Experimental and Computational Investigation of a Simple Fibre-mass System, *Proceedings of the 19th International Conference Engineering Mechanics 2013*, Institute of Thermomechanics AS CR, Svratka, CD-ROM.

[18] Polach, P., Hajžman, M., Šika, Z., and Svatoš, P. (2014), Influence of fibre stiffness model in a weight-fibre-pulley-drive mechanical system on coincidence with experimental measurement results, *Proceedings of Extended Abstracts 30th Conference with International Participation Computational Mechanics 2014*, University of West Bohemia in Plzeň Špičák, CD-ROM.

[19] Polach, P., Hajžman, M., Byrtus, M., and Šika, Z. (2015), Influence of the fibre spring-damper computational models in a mechanical system on the coincidence with the experimental measurement results, *Proceedings of 13th International Conference on Dynamical Systems – Theory and Applications, Dynamical Systems – Mechatronics and Life Sciences*, Department of Automation, Biomechanics and Mechatronics, Faculty of Mechanical Engineering, Łódź University of Technology, Łódź, 419-430.

[20] Michalík, J. and Janík, D. (2012), *Development of software control system in LabView for support of experiment with linear drive controlled by Emerson Unidrive SP converter, User Manual*, University of West Bohemia: Plzeň (in Czech).

[21] Hajžman, M. and Polach, P. (2011), Modelling of Cables for Application in Cable-Based Manipulators Design, *Proceedings of ECCOMAS Thematic Conference Multibody Dynamics 2011*, Université catholique de Louvain, Brussels, USB flash drive.

[22] Shabana, A.A. (1997), Flexible Multibody Dynamics: Review of Past and Recent Developments, *Multibody System Dynamics*, **1**(2), 189-222.

[23] Gerstmayr, J., Sugiyama, H. and Mikkola, A. (2012), Developments and Future Outlook of the Absolute Nodal Coordinate Formulation, *Proceedings of the 2nd Joint International Conference on Multibody System Dynamics*, University of Stuttgart, Institute of Engineering and Computational Mechanics, Stuttgart, USB flash drive.

[24] Wasfy, T.M. and Noor, A.K. (2003), Computational strategies for flexible multibody systems, *Applied Mechanics Review*, **56**(6), 553-613.

[25] Schiehlen, W. (2007), Research trends in multibody system dynamics, *Multibody System Dynamics*, **18**(1), 3-13.

[26] Stejskal, V. and Valášek. M. (1996), *Kinematics and Dynamics of Machinery*, Marcel Dekker, Inc.: New York.

[27] Awrejcewicz, J. (2012), *Classical Mechanics: Dynamics*, Springer: New York.

[28] Diao, X. and Ma, O. (2009), Vibration analysis of cable-driven parallel manipulators, *Multibody System Dynamics*, **21**(4), 347-360.

[29] Zi, B., Duan, B.Y., Du, J.L., and Bao, H. (2008), Dynamic modeling and active control of a cable-suspended parallel robot, *Mechatronics*, **18**(1), 1-12.

[30] Heyden, T. and Woernle, C. (2006), Dynamics and flatness-based control of a kinematically undetermined cable suspension manipulator, *Multibody System Dynamics*, **16**(2), 155-177.

[31] Kamman, J.W. and Huston, R.L. (2001), Multibody Dynamics Modeling of Variable Length Cable Systems, *Multibody*

System Dynamics, **5**(3), 211-221.

[32] Půst, L., Pešek, L., and Radolfová, A. (2011), Various Types of Dry Friction Characteristics for Vibration Damping, *Engineering Mechanics*, **18**(3-4), 203-224.

[33] Awrejcewicz, J. and Olejnik, P. (2005), Analysis of Dynamic Systems With Various Friction Laws, *Applied Mechanics Reviews*, **58**(6), 389-411.

[34] Polach, P. and Hajžman, M. (2008), Design of Characteristics of Air-Pressure-Controlled Hydraulic Shock Absorbers in an Intercity Bus, *Multibody System Dynamics*, **19**(1-2), 73-90.

[35] Rektorys, K., et al. (1994), *Survey of applicable mathematics, Vol. II*, Kluwer Academic Publishers: Dordrecht.

2018 ORDER FORM

This subscription is   ◯ New   ◯ A renewal

Please choose one subscription	Price (US$)	Required	Shipping price (US$)	
USA	◯ $300.00	Ground Shipping-USA	◯	Free
Canada	◯ $300.00	Ground Shipping- Canada	◯	$40.00
Mexico	◯ $300.00	Ground Shipping- Mexico	◯	$40.00
All Other Countries	◯ $300.00	Airmail -not available for USA and Canada	◯	$80.00

\# For e-copy subscription, no shipping fee is required.

Title Selection

No	TITLE	ISSN	QTY	PRICE(US$)
1				
2				
3				
4				

Methods Of Payment

Please Make Check/Bank Draft Payable to: L&H Scientific Publishing

Methods of Payment   ◯Check/Bank Draft Enclosed _____ US$ ◯Master Card   ◯Visa

Card No   ☐☐☐☐ ☐☐☐☐ ☐☐☐☐ ☐☐☐☐ Exp. Date   ☐☐☐☐

Contact Information

Organization: _____

Name: _____

Street Address: _____

(sorry, we cannot deliver to P.O. Box)

City/State/Zip _____

Country: _____

Email: _____

Phone/ Fax: _____

Date **X**	Signature **X**

L&H Scientific Publishing   P.O. Box 99   Glen Carbon   IL 62034   USA

Please complete the order form with payment to
L&H Scientific Publishing
P.O. Box 99
Glen Carbon, IL 62034, USA
Tel: 1-618-402-2267
Fax:1-618-545-9338
Email: lhscientificpublishing@gmail.com

Aims and Scope

The interdisciplinary journal publishes original and new results on recent developments, discoveries and progresses on Discontinuity, Nonlinearity and Complexity in physical and social sciences. The aim of the journal is to stimulate more research interest for exploration of discontinuity, complexity, nonlinearity and chaos in complex systems. The manuscripts in dynamical systems with nonlinearity and chaos are solicited, which includes mathematical theories and methods, physical principles and laws, and computational techniques. The journal provides a place to researchers for the rapid exchange of ideas and techniques in discontinuity, complexity, nonlinearity and chaos in physical and social sciences. Topics of interest include but not limited to

- Complex and hybrid dynamical systems
- Discontinuous dynamical systems (i.e., impulsive, time-delay, flow barriers)
- Nonlinear discrete systems and symbolic dynamics
- Fractional dynamical systems and control
- Stochastic dynamical systems and randomness
- Complexity, self-similarity and synchronization
- Complex nonlinear phenomena in physical systems
- Stability, bifurcation and chaos in complex systems
- Turbulence and other complex phenomena in hydrodynamics
- Nonlinear waves and solitons
- Dynamical networks
- Combinatorial aspects of dynamical systems
- Biological dynamics and biophysics
- Pattern formation, social science and complexization

No length limitations for contributions are set, but only concisely written manuscripts are published. Brief papers are published on the basis of Technical Notes. Discussions of previous published papers are welcome.

Peer Review

Discontinuity, Nonlinearity, and Complexity adopts the traditional blind-review policy in which the reviewers' names are concealed for submission author(s) for free submission. Each submitted manuscript is reviewed at least two referees in appropriate fields. In addition, the editorial board members' recommendation or established experts' recommendation publication are welcome.

Manuscript Submission Guidelines

For manuscript submission, authors can directly contact Editors-in-Chief. Manuscript preparation can follow the sample papers and journal manuscript templates (word file and Latex files), which can be found from the website at
https://lhscientificpublishing.com/Journals/DNC-Default.aspx

Proofs and Electronic Offprints

Authors will receive a PDF proof of their articles and, on publication, electronic offprints of the article.

Open Access

After manuscripts were accepted, author(s) have a right to request the accepted manuscripts published by L&H Scientific publishing with open access, and the author(s) have a responsibility to paying the open access publication fee with US$60 per page. The copyright is still held by the Publisher. Without any request of the open access publication, the accepted manuscripts are assumed to be published traditionally.

Continued from inside front cover

Didier Bénisti
CEA, DAM, DIF 91297 Arpajon Cedex
France
Fax: +33 169 267 106
Email: didier.benisti@cea.fr

Alexandre N. Carvalho
Departamento de Matemática, Instituto de
Ciências Matemáticas e de Computação
Universidade de São Paulo - Campus de São
Carlos, Caixa Postal 668, 13560-970 São
Carlos SP, Brazil
Email: andcarva@icmc.usp.br

Maurice Courbage
CNRS-UMR 7057 "Matière et Systèmes
Complexes", 75205 Paris Cedex 13 France
Email: maurice.courbage@univ-paris-
diderot.fr

Michal Fečkan
Department of Mathematical Analysis and
Numerical Mathematics, Comenius University
in Bratislava, Mlynska dolina
842 48 Bratislava, Slovakia
Fax: +421 2 654 12 305
Email: michal.feckan@fmph.uniba.sk

Marie-Christine Firpo
Laboratoire de Physique des Plasmas
CNRS UMR 7648, Ecole Polytechnique
91128 Palaiseau cedex, France
Fax: (00 33) 1 69 33 59 06
Email: marie-
christine.firpo@lpp.polytechnique.fr

Stefano Galatolo
Dipartimento di Matematica Applicata
Via Buonattoti 1
56127 Pisa, Italy
Email: galatolo@dm.unipi.it

N.H. Ibragimov
Director of Research Center "ALGA",
Department of Mathematics and Natural
Sciences, Blekinge Institute of Technology
Karlskrona 371 79, Sweden,
Email: nail.ibragimov@bth.se

Tassilo Küpper
Mathematical Institute
University of Cologne, Weyertal 86-90
D-50931 Cologne, Germany
Fax: +49 221 470 5021
Email: kuepper@math.uni-koeln.de

Marc Leonetti
IRPHE, Aix-Marseille Université
 UMR CNRS 7342, Technopôle de
Château-Gombert 13384 Marseilles Cedex
13 France, Fax: + 33 4 13 55 20 01
Email: leonetti@irphe.univ-mrs.fr

Mikhail Malkin
Institute of Information Technologies,
Mathematics and Mechanics, Lobachevsky
State University of Nizhny Novgorod,
Russia
Fax: +7 831 465 76 01
Email: malkin@unn.ru

Vladimir I. Nekorkin
Institute of Applied Physics of RAS
46 Ul'yanov Street, 603950, Nizhny
Novgorod, Russia
Email: vnekorkin@neuron.appl.sci-nnov.ru

Dmitry E. Pelinovsky
Department of Mathematics & Statistics
McMaster University, 1280 Main Street
West, Hamilton, Ontario, Canada L8S 4K1
Fax: +1 905 522 0935
Email: dmpeli@math.mcmaster.ca

Dmitry V. Kovalevsky,
Climate Service Center Germany
(GERICS), Hamburg & Nansen
International Environmental and Remote
Sensing Centre (NIERSC) & Saint
Petersburg State University (SPbU), St.
Petersburg, Russia
Email: dmitry.v.kovalevsky@gmail.com

Raul Rechtman
Instituto de Energias Renovables
Universidad Nacional Autonoma de Mexico
Priv. Xochicalco S/N, Temixco Morelos
65280 Mexico
Fax: +52 555 622 9791
Email: rrs@ier.unam.mx

Andrey Shilnikov
Department of Mathematics & Statistics
Georgia State University
100 Piedmont Ave Atlanta GA 30303
Tel: 404.413.6423
E-mail: ashilnikov@gsu.edu

Yury Stepanyants
University of Southern Queensland
West St., Toowoomba, QLD, 4350
Australia
Emails: yuas50@gmail.com,
Yury.Stepanyants@usq.edu.au

Vasily E. Tarasov
Skobeltsyn Institute of Nuclear Physics,
Lomonosov Moscow State University
119991 Moscow, Russia
Fax: +7 495 939 03 97
Email: tarasov@theory.sinp.msu.ru

Vladimir V. Uchaikin
Ulyanovsk State University
L.Tolstoy Str. 42
Ulyanovsk 432700, Russia
Fax: +7 842 241 20 88
Email: vuchaikin@gmail.com

Alexei A. Vasiliev
Space Research Institute
Profsoyuznaya 84/32
Moscow 117997, Russia
Fax: +7 495 333 12 48
Email: valex@iki.rssi.ru

Ling Zhao
DCM-FFCLRP-USP
Av. Bandeirantes, 3900
Bairro Monte Alegre, Ribeirao Preto –
SP CEP 14040-901, Brazil
Fax: 55-16-33150407
Email: zhao@usp.br

Contents

Available online at https://lhscientificpublishing.com/Journals/DNC-Download.aspx